Title

Monolithically Integrated Time-Varying Transmission Lines (TVTL) for Tunable and Interference Resilient RF Front Ends

Author

Zou, Xiating

Publication Date

2021

Peer reviewed|Thesis/dissertation

UNIVERSITY OF CALIFORNIA

Los Angeles

Monolithically Integrated Time-Varying Transmission Lines (TVTL) for Tunable and Interference Resilient RF Front Ends

A dissertation submitted in partial satisfaction of the

requirements for the degree Doctor of Philosophy

in Electrical and Computer Engineering

by

Xiating Zou

2021

ABSTRACT OF THE DISSERTATION

Monolithically Integrated Time-Varying Transmission Lines (TVTL) for Tunable and Interference Resilient RF Front Ends

by

Xiating Zou

Doctor of Philosophy in Electrical and Computer Engineering

University of California, Los Angeles, 2021

Professor Yuanxun Ethan Wang, Chair

With the development of modern wireless communications, interference has become a primary challenge for spectrum utilization and coexistence. High frequency-selectivity, tunable, low-noise, and high-linearity RF front-end components can greatly help the reception robustness under heavy interference scenarios. In this work, we propose to utilize the parametric mixing and amplification behavior of the time-varying transmission lines (TVTL) to design and implement such devices.

TVTLs are reactance-based circuits consisting of passive transmission lines whose inductance or capacitance is modulated by an electromagnetic wave called the “pump”. The single-sideband operation of a TVTL is especially favorable in that it can provide low-noise parametric amplification and frequency conversion with a moderate amount of gain. Moreover, TVTLs are compatible with modern IC technologies and can be realized with small form factors.

In this work, an in-depth theoretical study on the time-varying transmission lines (TVTL) in the single-sideband operation is presented. The theory then serves as a guideline to design three configurations of TVTLs on commercially available monolithic microwave integrated circuit (MMIC) processes. These MMIC TVTLs are then applied to design the RF correlator with either the frequency translational approach or the tunable peak amplifier approach to overcome the interference issues faced by modern receivers. Measurements results showed that 0 dB conversion loss was realized in the directly-pumped TVTL frequency translational correlator prototype. > 25 dB correlation suppression was also achieved by the same prototype when comparing the reception of the correlated signal with the reception of the uncorrelated (orthogonal) signal. For the tunable peak amplifier approach, experiments indicated that the peak gain of the tunable peak amplifier was > 25 dB with a bandwidth < 5MHz, and the measured frequency tuning range was > 100 MHz. The noise figure of the tunable peak amplifier in both simulation and measurement was < 1.8 dB. Lastly, the tunable peak amplifier also exhibited good linearity in the measurement, which was -11.5 dBm in-band IIP3 and 30 dBm out-of-band IIP3.

The dissertation of Xiating Zou is approved.

Aydin Babakhani

Christopher S. Lynch

Sudhakar Pamarti

Yuanxun Ethan Wang, Committee Chair

University of California, Los Angeles

2021

This dissertation is dedicated to my family and friends

for their unconditional love, companion, and support.

TABLE OF CONTENTS

LIST OF FIGURES

LIST OF TABLES

ACKNOWLEDGEMENTS

First of all, I would like to express my sincere gratitude to my advisor, Professor Yuanxun Ethan Wang, for his continuous support and mentorship throughout my study and research at UCLA. I still remember when I first came to UCLA for my undergraduate research 6 years ago, he would grab a chair and sit right next to me to discuss my project. He continues to provide such valuable discussions throughout my Ph.D. study, which makes this dissertation possible.

I would also like to acknowledge my doctoral committee members Professor Aydin Babakhani, Professor Christopher Lynch, and Professor Sudhakar Pamarti for taking the time to serve on my committee and providing insightful suggestions to improve this work.

Moreover, I am deeply grateful to Professor Tatsuo Itoh for serving on my committee when I took the qualifying examination. I learned a lot from him not only from his classes but also through daily interactions. His passion and devotion to his work inspired me to continue to overcome difficulties.

I would like to express my sincere thanks to my collaborator Dr. Qianteng Wu for countless discussions and unreserved collaborations. In this dissertation, Chapter 2 and Chapter 3 include the theoretical analyses, MMIC designs, experimental results, and discussions in the co-authored works [X. Zou, Q. Wu, and Y. E. Wang, "Monolithically Integrated Parametric Mixers With Time-Varying Transmission Lines (TVTLs)," *IEEE Trans. Microw. Theory Techn.*, vol. 68, no. 10, pp. 4479–4490, Oct. 2020] and [Q. Wu, X. Zou, and Y. E. Wang, "RF Correlator Receiver Based on Monolithically Integrated Directly-Pumped Time-Varying Transmission Lines," *preparation for publication*]. Chapter 4 consists of the RF correlator results discussed in [Q. Wu, X. Zou, and Y.

E. Wang, “RF Correlator Receiver Based on Monolithically Integrated Directly-Pumped Time-Varying Transmission Lines,” *preparation for publication*] and the tunable peak amplifier design proposed in [X. Zou, Q. Wu, and Y. E. Wang, “Tunable Peak Amplifier with Monolithically Integrated Time-Varying Transmission Lines (TVTL),” *preparation for publication*]. In these co-authored works, Dr. Qianteng Wu and I have been working together to design different versions of monolithically integrated TVTLs and apply them to various microwave/RF applications. Professor Yuanxun Ethan Wang is the advisor and PI of these works.

In addition, the alumni and lab mates of the Digital and Microwave Lab also provided great help throughout my time at UCLA. I would like to thank Dr. Qiang Xu, Dr. Shihan Qin, and Dr. Rui Zhu for their mentorship and help when I initially started this work. I am also grateful to Dr. Lap K Yeung, Dr. Ting Lu, Dr. Joseph Devin Schneider, Dr. Mathew Biedka, Dr. Zhi Yao, Dr. Cui Han, Ms. Qian Gao, Dr. Jean Paul Santos, Mr. Maziar Hedayati, and Dr. Yaozhong Liu for the meaningful and insightful discussions on LTCC technology, RF acoustic technology, integrated circuits, magnetic materials, and antennas.

Furthermore, I greatly appreciate the suggestions and instructions from Mr. Minji Zhu, the lab manager of the Center for High Frequency Electronics (CHFE) at UCLA, on equipment operations, experimental setups, and PCB fabrication.

I would like to thank Michael Foster, Gary Ray, and Ming Chen from Boeing Research & Technology for the technical discussions. This research is funded by National Science Foundation under the award No. 1610594 and DARPA SPAR program with subcontract from Boeing Inc. I’d also like to thank the Department of Electrical and Computer Engineering and the Graduate

Division of University of California, Los Angeles for funding my Ph.D. study and dissertation writing.

Last but not least, I want to express my sincere gratitude to my family for their unconditional love and encouragement. Without their support and guidance, I would not be able to sail this journey. I'd also like to acknowledge Jingjing, Munan, and Yi for our friendship. Also, thank my cats for their companion and emotional support during my time at UCLA. Their "thoughts" and "contributions" to this dissertation were either deleted or translated to English by their human fellow.

VITA

Education

2018-2021 ***Ph.D. Candidate*** in **Electrical and Computer Engineering**
University of California, Los Angeles, USA

2016-2018 ***M.S.*** in **Electrical and Computer Engineering**
University of California, Los Angeles, USA

2012-2016 ***B.S.*** in **Electronic Information Engineering**
University of Science and Technology of China, Hefei, Anhui, P. R. China

Publications

[1] **X. Zou**, Q. Wu, and Y. E. Wang, "Monolithically Integrated Parametric Mixers With Time-Varying Transmission Lines (TVTLs)," *IEEE Transactions on Microwave Theory and Techniques*, vol. 68, no. 10, pp. 4479–4490, Oct. 2020, doi: 10.1109/TMTT.2020.3011116.

[2] **X. Zou** and Y. E. Wang, "Parametric Flat Lenses for Near-Field Imaging and Electronic Beam Scanning," in 2020 IEEE International Symposium on Antennas and Propagation and North American Radio Science Meeting, Jul. 2020, pp. 511–512. doi: 10.1109/IEEE CONF35879.2020.9329972.

[3] **X. Zou**, Q. Wu, and Y. E. Wang, "Monolithically Integrated Parametric Mixers with Time-varying Transmission Lines (TVTL)," in *2019 IEEE MTT-S International Microwave Symposium (IMS)*, Jun. 2019, pp. 971–974, doi: 10.1109/MWSYM.2019.8700793.

[4] **X. Zou**, Q. Wu, and Y. E. Wang, "Parametrically Enhanced Delay Line with Monolithically Integrated Time-varying Transmission Lines (TVTL)," in *2019 IEEE Radio and Wireless Symposium (RWS)*, Jan. 2019, pp. 1–3, doi: 10.1109/RWS.2019.8714546.

[5] M. Hedayati, L. K. Yeung, M. Panahi, **X. Zou**, and Y. E. Wang, "Parametric Downconverter for Mixer-First Receiver Front Ends," *IEEE Transactions on Microwave Theory and Techniques*, pp. 1–1, 2021, doi: 10.1109/TMTT.2021.3058214.

[6] L. K. Yeung, **X. Zou**, and Y. Wang, "Parametrically enhanced bandpass filters," *IET Microwaves, Antennas & Propagation*, vol. 15, no. 2, pp. 229–240, 2021, doi: https://doi.org/10.1049/mia2.12039.

[7] J. D. Schneider, T. Lu, S. Tiwari, **X. Zou**, A. Mal, R. N. Candler, Y. E. Wang, and G. P. Carmen., "Frequency conversion through nonlinear mixing in acoustic waves," *Journal of Applied Physics*, vol. 128, no. 6, p. 064105, 2020, doi: 10.1063/5.0018074.

[8] L. K. Yeung, **X. Zou**, and Y. E. Wang, "BPFs with parametrically compensated passband insertion loss and selectivity," in *2020 IEEE/MTT-S International Microwave Symposium (IMS)*, Aug. 2020, pp. 803–806, doi: 10.1109/IMS30576.2020.9223902.

[9] T. Lu, J. D. Schneider, **X. Zou**, S. Tiwari, Z. Yao, G. P. Carmen, R. N. Candler, Y. E. Wang ., "Lamb Wave Resonator Loaded Non-reciprocal RF Devices," in *2020 IEEE/MTT-S International Microwave Symposium (IMS)*, Aug. 2020, pp. 516–519, doi: 10.1109/IMS30576.2020.9224075.

[10] L. K. Yeung, **X. Zou**, and Y. E. Wang, "Parametric quality factor enhancement for highly-selective miniaturized BPFs," in *2020 IEEE Radio and Wireless Symposium (RWS)*, Jan. 2020, pp. 148–151, doi: 10.1109/RWS45077.2020.9050095.

[11] Q. Wu, **X. Zou**, and Y. E. Wang, "Jamming Resilient Spread Spectrum Receiver with Time-Varying Transmission Line (TVTL) RF Correlator," in *2020 IEEE Radio and Wireless Symposium (RWS)*, Jan. 2020, pp. 20–23, doi: 10.1109/RWS45077.2020.9050035.

[12] Q. Wu, **X. Zou**, R. Zhu, and Y. E. Wang, "Chip-Scale RF Correlator with Monolithically Integrated Time-Varying Transmission Line (TVTL)," in *2018 IEEE/MTT-S International Microwave Symposium (IMS)*, Jun. 2018, pp. 431–434, doi: 10.1109/MWSYM.2018.8439846.

[13] M. Biedka, Q. Wu, **X. Zou**, S. Qin, and Y. E. Wang, "Integrated time-varying electromagnetic devices for ultra-wideband nonreciprocity," in *2018 IEEE Radio and Wireless Symposium (RWS)*, Jan. 2018, pp. 80–83, doi: 10.1109/RWS.2018.8304951.

[14] Q. Wu, **X. Zou**, S. Qin, and Y. E. Wang, "Frequency translational RF receiver with time-varying transmission lines (TVTL)," in *2017 IEEE MTT-S International Microwave Symposium (IMS)*, Jun. 2017, pp. 1767–1769, doi: 10.1109/MWSYM.2017.8058988.

Chapter 1

Introduction

As modern wireless communications evolve towards more advanced standards and technologies, the density of spectrum usage has reached a historically high. Meanwhile, the communications among users, hubs, and base stations in a wireless network face challenges not only in the effective range but also in data rate, spectral efficiency, robustness in fading environments, etc. To tackle some of these challenges, advanced digital modulation formats such as CDMA and OFDM were developed for various applications. However, these modulation formats produce non-constant-envelope signals which can be spread to adjacent channels due to the imperfection of transmitters, and thus, causes interference. The interference from the co-site radios or other users in the proximity to the receiver can significantly degrade the reception performance. Not only the signal-to-interference-plus-noise ratio (SINR) of the receiver decreases under such interferences, the linearity of the low-noise amplifier (LNA) in the receiver front-end also suffers when strong interference presents, resulting in various issues such as the receiver desensitization and blocking.

High frequency-selectivity, tunable, low-noise, and high-linearity RF front-end components can greatly help the robustness of reception under heavy interference scenarios. The benefits of such a device are three folds. First of all, the high frequency-selectivity of the receiver rejects external interferences from the adjacent channels. Second, the tunability enables the adaptive filtering of interferences. Lastly, the gain offered by such a device, if made without much noise penalty, can boost up the overall SINR of the receiver. High frequency-selectivity can be achieved

with conventional acoustic filters, however, these filters usually have fixed resonance and are unable to provide gain. Transistors-based circuits, on the other hand, can realize tunability and gain, but they do not always perform very well in terms of noise and linearity. To achieve all these features in one device, an approach drastically different from the traditional practices must be taken. In this work, we propose to apply the parametric mixing and amplification behavior of the time-varying transmission lines (TVTL) [1]-[2] to design such multi-functional RF front-end devices. It must be noted that TVTL is a different concept from the classical nonlinear transmission lines (NLTL) [3]. Discussions on NLTL in the literature have focused on the utilization of their nonlinear property in pulse shaping, harmonic generation, etc. [4]-[6]. The input of NLTL is usually one signal either in the form of a pulse or a low-frequency CW, and the output is a sharpened pulse or a frequency multiplied CW signal. TVTL bears the structure resemblance to NLTL, but it operates in a linear time-varying mode in which the output is approximately linear to the input, with an additional pump or carrier to control the time-varying behavior of the line. In order to assure that the device operates in the linear time-varying mode, dispersion engineering must be performed to prevent the nonlinear mode of the pump signal such as shock waves [7] from being formed and propagating in the transmission line.

Time-varying transmission lines (TVTL) are transmission lines and reactance-based structures that utilize nonlinear reactance to create parametric mixing and amplification. The parametric mixing and amplification effects were first studied in the 1950s and 1960s to design parametric amplifiers which were particularly favorable at that time due to the lack of transistors [8]-[14]. With the invention and advancement of semiconductor technology, the interest in applying parametric effects in electronic applications gradually died out. Nevertheless, the concept of parametric mixing and amplification still found vast applications in other areas. Many nonlinear

optical components such as optical amplifiers [15]-[18], mixers [19]-[20], oscillators [21], etc. were built based on it. For quantum computing applications, Josephson junctions were applied as nonlinear inductors to build parametric amplifiers with near quantum-limit sensitivity [22]-[24].

Recently, there has been a re-emergence of interest in parametric circuits among microwave circuit designers due to the low-noise characteristic of reactive-based circuits. In [25]-[29], single-stage reactive elements were used to design narrowband parametric mixers and parametric amplifiers. In [30]-[32], the negative impedance created by the parametric amplification was applied to enhance the quality factor of the resonators and compensate for the loss of sharp bandpass filters. In [33]-[34], the parametric mixing and amplification effects were utilized on the acoustic platform for the first time for novel acoustic mixers and Q-enhanced resonators. In [35], the phase stability of the parametric mixing was utilized in flat lenses for near-field imaging and far-field beam scanning. Distributed parametric circuits such as the time-varying transmission lines (TVTL) were also studied for broadband applications including the nonmagnetic circulator [36]-[38], the frequency translational RF receiver [39], and the low-loss delay line [40]. The frequency translational RF receiver proposed in [39] operates in a way similar to other mixer-first receivers [41]-[43] but uses parametric mixers instead of switched capacitors to convert the RF signal to different bands for the benefit of filtering at a controllable/tunable frequency.

Comparing with prior works, the work presented here includes a fundamental study of TVTL's parametric amplification and mixing performance in the single-sideband operation mode. Detailed noise analyses and discussions are also presented in Chapter 2, which demonstrate a different understanding than that in the classical literature [9][44] where a 3 dB noise figure lower limit was quoted. The new understanding showed that the theoretical lower limit of a TVTL's

noise figure could be as low as the quantum noise limit. Moreover, with input reactive termination at ω_{p-s}, an additional benefit offered by the TVTL to the system noise performance was that the noise generated by the output load incident into the TVTL could be reflected with a properly designed phase and cancel what was originally generated by the load. It thus could bring the noise advantage even to the stage following the TVTL. In Chapter 3, we also demonstrate three TVTL mixer configurations, namely the traveling-wave TVTL, the reflective TVTL, and the directly-pumped TVTL on commercially available GaAs HBT MMIC processes. This chapter illustrates how modern MMIC technology can be used to bring the classical concept of parametric mixers/amplifiers into practical RF applications. In Chapter 4, the fabricated MMIC TVTLs are applied to build the novel RF correlator with either the frequency translational approach or the tunable peak amplifier approach for interference rejection and mitigation. The measured results of the prototypes indicate that the TVTL-based circuits exhibit characteristics of both passive and active circuits that can enable high frequency-selectivity, tunability, and low-noise operation.

Chapter 2

Fundamentals of Time-Varying Transmission Lines (TVTL)

The time-varying transmission line (TVTL) is a unique type of transmission line structure whose characteristic impedance is a function of time and space. The theory of the TVTL in infinitely long propagating circuits was first proposed under the name of the traveling wave parametric amplifier and analyzed in [8]-[9] with the time-varying coupling inductance. It was revisited and derived with the time-varying capacitance to reveal the operating principle of the TVTL in [37], by assuming the double-sideband operation condition. The double-sideband operation involves the frequencies of the signal ω_s, the pump ω_p, and the two sidebands in mixing terms $\omega_{p\pm s} = (\omega_p \pm \omega_s)$. In this work, the TVTLs are forced into the single-sideband operation by creating a stopband at ω_{p+s}. In general, solutions yield differently whether double-sideband or single-sideband propagation condition is assumed. Comparing to the double-sideband mixing, the single-sideband operation of the TVTL theoretically offers a better chance of achieving positive gain at the lower sideband ω_{p-s} and the signal frequency ω_s. In this section, the theory of the single-sideband operation is introduced with the time-varying capacitance. It is then compared with the double-sideband operation of the time-varying transmission lines to reveal its superior gain performance. Lastly, the thermal noise performance of the time-varying transmission lines (TVTL) in the single-sideband operation is discussed. We also argue in Section 2.3 and Section 2.4 that the theoretical lower limit of a TVTL's noise figure could be as low as the quantum noise limit. This chapter includes theoretical analyses and discussions reported in [45].

2.1 Single-sideband operation of the time-varying transmission lines (TVTL)

Figure 2-1 shows the lumped-element model of an infinitely long TVTL with the time-varying capacitance. The inductance per unit length is denoted by L which is time-invariant. The capacitance per unit length C is modulated by a voltage $v_c(z,t)$. Assume the capacitance per unit length C varies linearly with the voltage $v_c(z,t)$, its value can be expressed as:

$$C(v_c) = C_0 + C_1 \cdot v_c. \tag{2-1}$$

where C_0 is the mean capacitance per unit length, C_1 is the first order capacitance coefficient, and v_c is the voltage across the capacitance. For the case where $C(v_c)$ is a nonlinear function, equation (2-1) can still serve as the first-order approximation of $C(v_c)$. The mean capacitance C_0 and the first order capacitance coefficient C_1 in this case can then be derived by performing a Fourier expansion of the time-varying capacitance:

$$\begin{cases} C_0 = \dfrac{1}{2\pi}\displaystyle\int_{-\pi}^{\pi} C(v_c)\, d(\omega t) \\ C_1 = \dfrac{1}{\pi}\displaystyle\int_{-\pi}^{\pi} C(v_c)\cos(\omega t)\, d(\omega t) \end{cases}. \tag{2-2}$$

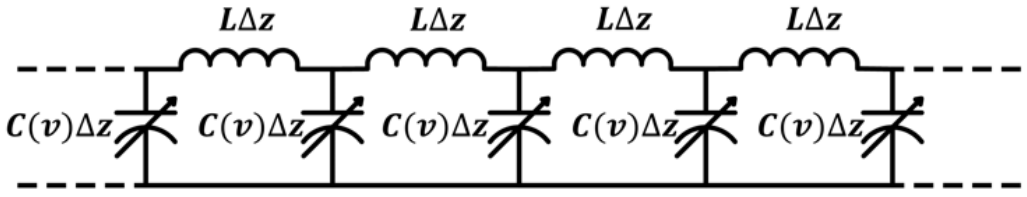

Figure 2-1. Lumped-element model of the time-varying transmission line with time-varying capacitance.

To derive the single-sideband mixing solution of the traveling-wave TVTL, one should modify the conventional wave equation to be [46]:

$$\frac{\partial^2 v(z,t)}{\partial z^2} = L\frac{\partial}{\partial t}\left[C(z,t)\frac{\partial v(z,t)}{\partial t}\right]. \tag{2-3}$$

Suppose the time-varying capacitance in the TVTL is modulated by a large-signal pump at ω_p. Its complex amplitude is denoted by V_p and is assumed to be constant along the TVTL. When a small-signal tone at ω_s of amplitude V_0 enters a TVTL, the pump signal will couple with the small-signal $v_s(z,t)$ so that intermodulation tones at $\omega_{p\pm s}$ will be generated. One may obtain the single-sideband solution where only frequency components at ω_s, ω_{p-s}, and ω_p exist by properly terminating ω_{p+s} with a stopband. Denote the voltage waveforms consisting of frequency components ω_s, ω_{p-s}, and ω_p along the TVTL as:

$$\begin{aligned} v_c(z,t) &= v_s(z,t) + v_{p-s}(z,t) + v_p(z,t) \\ &= \sum_i V_i(z)e^{j\omega_i t} + V_i^*(z)e^{-j\omega_i t}. \end{aligned} \tag{2-4}$$

where $i \in \{s, p-s, p\}$ indicates the frequency component ω_s ω_{p-s}, and ω_p. $(\cdot)^*$ denotes the operation of the complex conjugate. $V_i(z) = A_i(z)e^{-j\beta_i z}$ are the complex magnitudes of these frequency components. The initial phases ϕ_i of these waveforms are captured in $A_i(z)$'s. β_i's are the propagation constants of the voltage waveforms. Then, the capacitance per unit length of a TVTL in equation (2-1) can thus be expressed as:

$$C(v_c) = C_0 + C_1[v_s(z,t) + v_{p-s}(z,t) + v_p(z,t)]. \tag{2-5}$$

Substitute equations (2-4) and (2-5) into equation (2-3) and consider only the terms of $e^{\pm j\omega_s t}$ and $e^{\pm j\omega_{p-s} t}$. Then, equation (2-3) can be simplified into:

$$\frac{\partial^2 V_s(z)}{\partial z^2} = -\omega_s^2 L C_0 V_s(z) - \omega_s^2 L C_p V_{p-s}^*(z). \tag{2-6}$$

$$\frac{\partial^2 V_{p-s}(z)}{\partial z^2} = -\omega_{p-s}^2 L C_0 V_{p-s}(z) - \omega_{p-s}^2 L C_p V_s^*(z). \tag{2-7}$$

where

$$C_p = \frac{1}{2} C_1 |A_p| e^{-j(\beta_p z - \phi_p)} = \frac{1}{2} \xi_0 C_0 e^{-j(\beta_p z - \phi_p)}. \tag{2-8}$$

is a complex value of the time-varying capacitance, and $\xi_0 = C_1|A_p|/C_0$ is defined as the capacitance modulation index of a TVTL, representing the amount of capacitance variation with respect to its mean capacitance.

To further simplify equation (2-6) and (2-7), one may assume that $A_i(z)$'s are slow-varying functions of z as the capacitance modulation index ξ is usually small. As a result, $\partial^2 A_i(z)/\partial z^2$ is negligible in comparison to $\beta_i \, \partial A_i(z)/\partial z$ [9]. Moreover, assume that the TVTL is non-dispersive within the frequency range of interest, i.e.,

$$v_p = \frac{\omega_s}{\beta_s} = \frac{\omega_{p-s}}{\beta_{p-s}} = \frac{\omega_p}{\beta_p} = \frac{1}{\sqrt{LC_0}}. \tag{2-9}$$

where v_p denotes the phase velocity of the traveling wave. Then, equation (2-6) and (2-7) can be re-written into:

$$\frac{dA_s(z)}{dz} = -\frac{j}{4}\xi_0\beta_s e^{j\phi_p}A_{p-s}^*(z). \tag{2-10}$$

$$\frac{dA_{p-s}(z)}{dz} = -\frac{j}{4}\xi_0\beta_{p-s} e^{j\phi_p}A_s^*(z). \tag{2-11}$$

and thus:

$$\frac{d^2A_s(z)}{dz^2} = \frac{d}{dz}\left(\frac{dA_s(z)}{dz}\right) = \frac{1}{16}\xi_0^2\beta_s\beta_{p-s}A_s(z). \tag{2-12}$$

From the theory of the ordinary differential equation, the general solution of $A_s(z)$ to equation (2-12) is:

$$A_s(z) = c_1e^{\lambda z} + c_2e^{-\lambda z}. \tag{2-13}$$

where $\lambda = \xi_0\sqrt{\beta_s\beta_{p-s}}/4$ is the eigenvalue of equation (2-12), and c_1, c_2 are unknown coefficients to be determined by initial conditions. Substituting equation (2-13) into equation (2-10), the general solution of $A_{p-s}(z)$ can be found as

$$A_{p-s}(z) = -j\sqrt{\frac{\beta_{p-s}}{\beta_s}}e^{j\phi_p}\left[c_1^*e^{\lambda z} - c_2^*e^{-\lambda z}\right]. \tag{2-14}$$

The initial conditions of the single-sideband TVTL are:

$$A_s(z=0) = \frac{V_0}{2}e^{j\phi_s}. \tag{2-15}$$

$$A_{p-s}(z=0) = 0. \tag{2-16}$$

Apply them to equation (2-13) and (2-14), the unknown coefficients are thus derived as:

$$c_1 = c_2 = \frac{V_0}{4} e^{j\phi_s}. \tag{2-17}$$

The solution to equation (2-5) is then given by:

$$V_s(z) = \frac{V_0}{2} e^{j\phi_s} \cosh\left(\frac{1}{4}\xi_0 \sqrt{\beta_s \beta_{p-s}} z\right) e^{-j\beta_s z}. \tag{2-18}$$

$$V_{p-s}(z) = -j\frac{V_0}{2} e^{j(\phi_p - \phi_s)} \sqrt{\frac{\beta_{p-s}}{\beta_s}} \sinh\left(\frac{1}{4}\xi_0 \sqrt{\beta_s \beta_{p-s}} z\right) e^{-j\beta_{p-s} z}. \tag{2-19}$$

Since the TVTL parametric mixer is a special case of the reactive mixers, it must follow the Manley-Rowe relation [47], that is:

$$\frac{P_s - P_{in}}{\omega_s} - \frac{P_{p-s}}{\omega_{p-s}} = 0. \tag{2-20}$$

where $P_{in} = V_0^2/2Z_0$ is the input signal power at ω_s of the TVTL, and P_s, P_{p-s} are the average output power of the tone at ω_s and the tone at ω_{p-s} respectively. From equations (2-18) and (2-19), P_s and P_{p-s} are derived as:

$$P_s = \frac{V_0^2}{2Z_0} \cosh^2\left(\frac{1}{4}\xi_0 \sqrt{\beta_s \beta_{p-s}} z\right). \tag{2-21}$$

$$P_{p-s} = \frac{V_0^2}{2Z_0} \frac{\beta_{p-s}}{\beta_s} \sinh^2\left(\frac{1}{4}\xi_0 \sqrt{\beta_s \beta_{p-s}} z\right). \tag{2-22}$$

Plugging P_s, P_{in}, and P_{p-s} into the left-hand side of equation (2-20), one can prove that the Manley-Rowe relation is indeed satisfied.

Moreover, equations (2-18) and (2-19) indicates an RF-to-RF power conversion from the pump signal to either the signal tone at ω_s or the mixing product at ω_{p-s}. When the time-varying transmission line is sufficiently long, one may obtain a moderate amount of power gain at either ω_s or ω_{p-s}, which are:

$$G_{s,s} = \frac{P_s}{P_{in}} = \cosh^2\left(\frac{1}{4}\xi_0\sqrt{\beta_s\beta_{p-s}}z\right). \tag{2-23}$$

$$G_{p-s,s} = \frac{P_{p-s}}{P_{in}} = \frac{\beta_{p-s}}{\beta_s}\sinh^2\left(\frac{1}{4}\xi_0\sqrt{\beta_s\beta_{p-s}}z\right). \tag{2-24}$$

where z represents the length of the transmission line. Equation (2-24) shows that as β_{p-s}/β_s increases, i.e., the ratio between ω_{p-s} and ω_s increases, the conversion gain increases. Therefore, the frequency separation between ω_s and ω_p should be far enough to obtain a fair amount of conversion gain within a short length of a TVTL. Furthermore, the conversion gain improves as the capacitance modulation index ξ_0 grows, indicating that a larger pump voltage V_p will lead to a better conversion gain. Thirdly, in the ideal case where the transmission line is lossless, the conversion gain increases as the transmission line grows longer. In reality, Ohmic loss is inevitable, and it accumulates as the length of the transmission line increases. The conversion gain may even reduce if the TVTL is too long. Lastly, the dispersion of the transmission line may also cause a phase mismatch so that the condition in equation (2-9) may no longer hold. This phase error reduces the conversion gain as formulated in [9].

Similar frequency conversion exists from ω_{p-s} to ω_s if the input signal is at ω_{p-s}. The signal power gain and conversion power gain, in this case, can be easily obtained by replacing the initial conditions in equations (2-15)-(2-16) by:

$$A_s(z=0)=0. \tag{2-25}$$

$$A_{p-s}(z=0)=\frac{V_0}{2}e^{j\phi_{p-s}}. \tag{2-26}$$

and thus, the output voltages of the TVTL are:

$$V_s(z)=-j\frac{V_0}{2}e^{j(\phi_p-\phi_{p-s})}\sqrt{\frac{\beta_s}{\beta_{p-s}}}\sinh\left(\frac{1}{4}\xi_0\sqrt{\beta_s\beta_{p-s}}z\right)e^{-j\beta_s z}. \tag{2-27}$$

$$V_{p-s}(z)=\frac{V_0}{2}e^{j\phi_{p-s}}\cosh\left(\frac{1}{4}\xi_0\sqrt{\beta_s\beta_{p-s}}z\right)e^{-j\beta_{p-s}z}. \tag{2-28}$$

Therefore, the signal power gain $G_{p-s,p-s}$ and the conversion power gain $G_{s,p-s}$ can be derived as

$$G_{p-s,p-s}=\cosh^2\left(\frac{1}{4}\xi_0\sqrt{\beta_s\beta_{p-s}}z\right). \tag{2-29}$$

$$G_{s,p-s}=\frac{\beta_s}{\beta_{p-s}}\sinh^2\left(\frac{1}{4}\xi_0\sqrt{\beta_s\beta_{p-s}}z\right). \tag{2-30}$$

Combing both frequency coupling mechanisms, a time-varying transmission line (TVTL) can be generalized into a linear, four-port network that is defined by cross-coupled frequencies ω_s and ω_{p-s}. The symbolic representation of the four-port linear network is depicted in Figure 2-2.

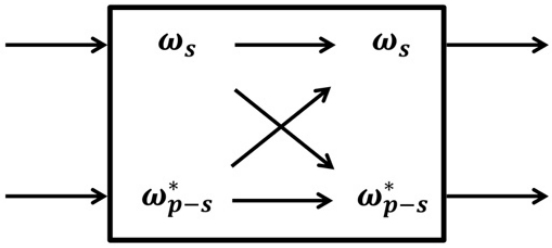

Figure 2-2 Symbolic representation of the TVTL by a four-port linear network.

Denote t_{ii} to be the voltage gain of the TVTL at ω_i when $V_k^+(0) = 0, k \neq i$, and t_{ij} to be the voltage conversion gain of the TVTL from ω_j to ω_i when $V_k^+(0) = 0, k \neq i$ where $i, j, k \in \{s, p-s\}$. From equations (2-18)-(2-19) and equations (2-27)-(2-28), considering the Ohmic loss of the lossy TVTL, t_{ii} and t_{ij} can be written as:

$$t_{s,s} = \cosh\left(\frac{1}{4}\xi_0\sqrt{\beta_s\beta_{p-s}}z\right)e^{-(\alpha_s+j\beta_s)z}. \tag{2-31}$$

$$t_{s,p-s} = -je^{j\phi_p}\sqrt{\frac{\beta_s}{\beta_{p-s}}}\sinh\left(\frac{1}{4}\xi_0\sqrt{\beta_s\beta_{p-s}}z\right)e^{-(\alpha_s+j\beta_s)z}. \tag{2-32}$$

$$t_{p-s,s} = je^{-j\phi_p}\sqrt{\frac{\beta_{p-s}}{\beta_s}}\sinh\left(\frac{1}{4}\xi_0\sqrt{\beta_s\beta_{p-s}}z\right)e^{-(\alpha_{p-s}-j\beta_{p-s})z}. \tag{2-33}$$

$$t_{p-s,p-s} = \cosh\left(\frac{1}{4}\xi_0\sqrt{\beta_s\beta_{p-s}}z\right)e^{-(\alpha_{p-s}-j\beta_{p-s})z}. \tag{2-34}$$

where α_s and α_{p-s} are the attenuator constants of the lossy TVTL at ω_s and ω_{p-s} respectively. Noted that $|t_{ii}|^2$'s and $|t_{ij}|^2$'s are the signal power gain and conversion power gain of a practical

lossy TVTL. They are the generalized versions of equations (2-23)-(2-24) and (2-29)-(2-30) that consider the actual loss of the TVTL.

2.2 Single-sideband operation vs. double-sideband operation

Double-sideband operation is another operation mode of TVTLs in which both sidebands at $\omega_{p\pm s} = (\omega_p \pm \omega_s)$ are allowed to propagate on the TVTL. The power gain $G_{s,s}$ at the signal frequency $\omega_{p\pm s}$ and the conversion gain $G_{p\pm s,s}$ at the upconverted frequencies $\omega_{p\pm s}$ can be derived by adding an extra term $v_{p+s}(z,t)$ to equation (2-4) and following the steps in equations (2-5)-(2-19). The detailed discussions can be found in [36], and the results are re-written here for comparison.

$$G_{s,s} = \frac{P_s}{P_{in}} = \cos^2\left(\frac{1}{2\sqrt{2}}\xi_0\beta_s z\right). \tag{2-35}$$

$$G_{p\pm s,s} = \frac{P_{p\pm s}}{P_0} = \frac{1}{2}\frac{\beta_{p\pm s}^2}{\beta_s^2}\sin^2\left(\frac{1}{2\sqrt{2}}\xi_0\beta_s z\right). \tag{2-36}$$

Comparing equation (2-35) with equation (2-23), one can easily tell that a positive signal gain is impossible with the double-sideband operation but achievable with the single-sideband operation. The conversion gain, however, can be positive in both conditions as indicated in equation (2-24) and equation (2-36). Equations (2-24) and (2-36) give the same asymptotic result when the modulation index ξ_0 inside the parentheses is small. As the modulation index ξ_0, increases, the single-sideband conversion gain in Equation (2-24) will eventually outgrow the double-sideband conversion gain. It should be noted that equations (2-35)-(2-36) are for lossless time-varying transmission lines. For practical transmission lines with attenuation, an additional loss factor of

$e^{-2\alpha_s z}$ or $e^{-2\alpha_{p\pm s} z}$ should be included, as in equations (2-31)-(2-34), where α_s and $\alpha_{p\pm s}$ are the attenuation constants at the original signal frequency at ω_s and the upconverted signal at $\omega_{p\pm s}$ respectively.

2.3 Thermal noise analysis of TVTL for the single-sideband operation

In the previous section, we derived the frequency coupling and gain performance of ideal continuous TVTLs operating in the single-sideband mode. In practice, for TVTLs to operate in the linear time-varying mode, dispersion engineering must be performed to prevent nonlinear modes such as the shock wave [7] from being formed and propagating in the transmission line. Therefore, practical TVTLs are usually achieved by periodically loading a transmission line with varactor diodes. Then, TVTLs can also be analyzed from the traveling-wave amplifier point of view. Denote $g_{s,s}$, $g_{p-s,s}$ as the small-signal transconductances of a TVTL unit cell and M to be the total number of unit cells. When a signal voltage v_s is applied at the input of the TVTL, the time-varying capacitor in each unit cell will either generate current at ω_s with $g_{s,s}$ or convert the input voltage to current at ω_{p-s} with $g_{p-s,s}$. These currents will combine in phase at the output of the TVTL, so transconductances $g_{s,s}$ and $g_{p-s,s}$ of a unit cell can be related to $t_{s,s}$ and $t_{p-s,s}$ by

$$\left(1 + M g_{s,s} Z_0\right) e^{-(\alpha_s + j\beta_s)z} = t_{s,s}. \tag{2-37}$$

$$M\left(g_{p-s,s} Z_0\right) e^{-(\alpha_{p-s} - j\beta_{p-s})z} = t_{p-s,s}. \tag{2-38}$$

Similarly, if a voltage at ω_{p-s} is applied at the input of the TVTL, the time-varying capacitor in each unit cell will either generate current at ω_{p-s} with a small signal transconductance $g_{p-s,p-s}$

or transform the input voltage to current at ω_s with a small signal conversion transconductance $g_{s,p-s}$. These transconductances can also be related to $t_{p-s,p-s}$ and $t_{s,p-s}$ by

$$\left(1 + M g_{p-s,p-s} Z_0\right) e^{-(\alpha_{p-s} - j\beta_{p-s})z} = t_{p-s,p-s}. \tag{2-39}$$

$$M\left(g_{s,p-s} Z_0\right) e^{-(\alpha_s + j\beta_s)z} = t_{s,p-s}. \tag{2-40}$$

Ideally, lossless TVTLs do not introduce additional thermal noise to the system because they are made of pure reactive elements. In practice, resistive loss does exist due to the finite conductivity of conductors and finite quality factor of varactor diodes. The resistive loss of the TVTL will add thermal noise at both the signal frequency ω_s and the converted frequency ω_{p-s}. From [48, eq (10.14)], the input-referred noise power added by a lossy TVTL are

$$P_{ni,s} = kT_0 B(e^{2\alpha_s z} - 1). \tag{2-41}$$

$$P_{ni,p-s} = kT_0 B(e^{2\alpha_{p-s} z} - 1). \tag{2-42}$$

where $e^{2\alpha_s z} = 1/e^{-2\alpha_s z}$ and $e^{2\alpha_{p-s} z} = 1/e^{-2\alpha_{p-s} z}$ is the loss factor of the TVTL, and $kT_0 B$ is the thermal noise power emitted by the thermal resistor at room temperature T_0. Since the TVTL is implemented with a periodic structure of M unit cells, its noise power is generated by uncorrelated distributed thermal resistors in each cell. As a result, the added noise power in equations (2-41) and (2-42) can also be considered as a summation of the thermal noise power generated by the thermal resistors in each unit cell.

$$P_{ni,s} = \frac{\sum_{m=1}^{M} \left[v_{ni,s}^{(m)}\right]^2}{2Z_0} = \frac{M v_{ni,s}^2}{2Z_0}. \tag{2-43}$$

$$P_{ni,p-s} = \frac{\sum_{m=1}^{M}\left[v_{ni,p-s}^{(m)}\right]^2}{2Z_0} = \frac{Mv_{ni,p-s}^2}{2Z_0}. \tag{2-44}$$

where $v_{ni,s}^{(m)}$ and $v_{ni,p-s}^{(m)}$ are the noise voltage amplitude generated at ω_s and ω_{p-s} by the thermal resistor in the m-th unit cell, $m = 1,2,\dots,M$. $v_{ni,s}^{(m)}$'s and $v_{ni,p-s}^{(m)}$'s are assumed to have the same amplitude value $v_{ni,s}$ and $v_{ni,p-s}$ respectively.

2.3.1 Insertion noise factor of TVTL

Assume the input at ω_{p-s} of a TVTL is terminated with a matched cold resistor. Then, the thermal noise at ω_s added by the TVTL and arrive at the output comes from two thermal noise sources. The first one is the thermal noise directly generated at ω_s by the TVTL and arrives at the output with amplification. The second type of thermal noise is the one originally emitted at ω_{p-s} and then converted to ω_s by the TVTL. For the noise voltage $v_{ni,s}^{(m)}$ emitted at ω_s by the m-th unit cell of the TVTL, it generates noise current through itself and the following $(M-m)$ unit cells. These $(M-m+1)$ currents will flow to the output of the TVTL and combine in phase on the load. From the traveling-wave amplifier point of view and replace $g_{s,s}Z_0$ with the relationship in equation (2-37), the complex amplitudes of the output noise at ω_s from $v_{ni,s}^{(m)}$ can be written as:

$$\begin{aligned}\omega_s \longrightarrow \omega_s\colon v_{no1,s}^{(m)} &= v_{ni,s}^{(m)}e^{-\alpha_s z} + (M-m+1)g_{s,s}Z_0 v_{ni,s}^{(m)}e^{-\alpha_s z} \\ &= \left\{1 + \left(\frac{M-m+1}{M}\right)[\cosh(\lambda z) - 1]\right\} v_{ni,s}^{(m)}e^{-\alpha_s z}.\end{aligned} \tag{2-45}$$

where $\lambda = \xi_0\sqrt{\beta_s\beta_{p-s}}/4$ is the eigenvalue of equation (2-12). Then, summing the output noise power from all unit cells and combing the relationship in equations (2-41) and (2-43), the total output noise power from $v_{ni,s}^{(m)}$'s is thus:

$$\omega_s \longrightarrow \omega_s\colon P_{no1,s} = \frac{\sum_{m=1}^{M}\left|v_{no1,s}^{(m)}\right|^2}{2Z_0}$$

$$= \frac{v_{ni,s}^2}{2Z_0}e^{-2\alpha_s z}\sum_{m=1}^{M}\left\{1+\left(\frac{M-m+1}{M}\right)[\cosh(\lambda z)-1]\right\}^2$$

$$\approx \frac{kT_0B(e^{2\alpha_s z}-1)}{M}e^{-2\alpha_s z}\{M+(M+1)[\cosh(\lambda z)-1]\}$$

$$\approx kT_0B(e^{2\alpha_s z}-1)\cosh(\lambda z)\,e^{-2\alpha_s z}. \tag{2-46}$$

Note that in equation (2-46), the term of $[\cosh(\lambda z)-1]^2$ is neglected because the signal gain of the TVTL is small and $[\cosh(\lambda z)-1]^2 \ll 1$.

For the noise voltage $v_{ni,p-s}^{(m)}$ emitted at ω_{p-s} by the m-th unit, it will also interact with $(M-m+1)$ parametrically pumped unit cells and generate noise currents that add in-phase when they arrive at the output. Following the same traveling-wave amplifier analysis used in equation (2-45) and substitute $g_{s,p-s}Z_0$ with the relationship in equation (2-38). Then, the complex magnitudes and output noise power at ω_s from $v_{n,p-s}^{(m)}$'s can be formulated by:

$$\omega_{p-s} \longrightarrow \omega_s\colon v_{no2,s}^{(m)} = (M-m+1)g_{s,p-s}Z_0v_{n,p-s}^{(m)}e^{-\alpha_s z}$$

$$= e^{j\phi_p}\sqrt{\frac{\beta_s}{\beta_{p-s}}}\sinh(\lambda z)\frac{(M-m+1)}{M}v_{ni,p-s}^{(m)}e^{-\alpha_s z}. \tag{2-47}$$

$$\omega_{p-s} \longrightarrow \omega_s: P_{no2,s} = \frac{\sum_{m=1}^{M}\left|v_{no2,s}^{(m)}\right|^2}{2Z_0}$$

$$= kT_0B(e^{2\alpha_{p-s}z}-1)\frac{\beta_s}{\beta_{p-s}}\sinh^2(\lambda z)\,e^{-2\alpha_s z}\sum_{m=1}^{M}\frac{1}{M}\left(\frac{M-m+1}{M}\right)^2$$

$$\approx \frac{1}{3}kT_0B(e^{2\alpha_s z}-1)\frac{\beta_s}{\beta_{p-s}}\sinh^2(\lambda z)\,e^{-2\alpha_s z}. \tag{2-48}$$

With equations (2-46) and (2-48), the insertion noise factor of TVTLs can be calculated by

$$F = \frac{S_i/N_i}{S_o/N_o} = \frac{S_i}{\left|t_{s,s}\right|^2 S_i}\cdot\frac{\left|t_{s,s}\right|^2 kT_0B + P_{no1,s} + P_{no2,s}}{kT_0B}$$

$$= 1 + \frac{(e^{2\alpha_s z}-1)}{\cosh(\lambda z)} + \frac{1}{3}\frac{\beta_s}{\beta_{p-s}}(e^{2\alpha_{p-s}z}-1)\tanh^2(\lambda z). \tag{2-49}$$

Equation (2-49) is the lower bound of the insertion noise factor of a TVTL. It indicates that as the modulation index ξ_0 increases, i.e., the eigenvalue of the TVTL $\lambda = \xi_0\sqrt{\beta_s\beta_{p-s}}/4$ incrases, the insertion noise factor will approach to

$$F \to 1 + \frac{1}{3}\frac{\beta_s}{\beta_{p-s}}(e^{2\alpha_{p-s}z}-1). \tag{2-50}$$

in which the second term of equation (2-51) is a small number especially when the frequency ratio between the converted tone and the signal tone $\omega_{p-s}/\omega_s = \beta_{p-s}/\beta_s$ is large.

2.3.2 Conversion noise factor of TVTL

Similar analysis can be carried out for the conversion thermal noise calculation. The total noise power at ω_{p-s} added by the lossy TVTL can also be attributed to two components. The first component comes from the thermal noise $v_{ni,s}^{(m)}$'s emitted at ω_s and then converted to ω_{p-s} by the

TVTL. From equation (2-40), the complex magnitude of the output noise voltage $v_{no1,p-s}^{(m)}$ due to $v_{ni,s}^{(m)}$ from the thermal resistor in the m-th unit cell can be written as:

$$\omega_s \longrightarrow \omega_{p-s}\colon v_{no1,p-s}^{(m)} = (M-m+1)g_{p-s,s}Z_0 v_{ni,s}^{(m)} e^{-\alpha_{p-s}z}$$

$$= je^{j\phi_p}\sqrt{\frac{\beta_{p-s}}{\beta_s}}\sinh(\lambda z)\left(\frac{M-m+1}{M}\right)v_{ni,s}^{(m)}e^{-\alpha_{p-s}z}. \quad (2\text{-}51)$$

and the total output noise power from M unit cells is

$$\omega_s \longrightarrow \omega_{p-s}\colon P_{no1,p-s} = \frac{\sum_{m=1}^{M}\left|v_{no1,p-s}^{(m)}\right|^2}{2Z_0}$$

$$= \frac{v_{ni,s}^2}{2Z_0}e^{-2\alpha_{p-s}z}\frac{\beta_{p-s}}{\beta_s}\sinh^2(\lambda z)\sum_{m=1}^{M}\left(\frac{M-m+1}{M}\right)^2$$

$$\approx \frac{1}{3}kT_0B(e^{2\alpha_s z}-1)\frac{\beta_{p-s}}{\beta_s}\sinh^2(\lambda z)e^{-2\alpha_{p-s}z}. \quad (2\text{-}52)$$

The second output noise component is from the thermal noise voltages $v_{ni,p-s}^{(m)}$'s generated at ω_{p-s}. These noise voltages are then amplified by the TVTL as they travel along the TVTL and arrive at the output ω_{p-s} port. Following the same analysis, the complex amplitudes and the total output noise power added by $v_{ni,p-s}^{(m)}$'s can be derived as:

$$\omega_{p-s} \longrightarrow \omega_{p-s}\colon v_{no2,p-s}^{(m)} = \{1+(M-m+1)g_{p-s,p-s}Z_0\}v_{n,p-s}^{(m)}e^{-\alpha_{p-s}z}$$

$$= \left\{1+\left(\frac{M-m+1}{M}\right)[\cosh(\lambda z)-1]\right\}v_{ni,p-s}^{(m)}e^{-\alpha_{p-s}z}. \quad (2\text{-}53)$$

$$\omega_{p-s} \longrightarrow \omega_{p-s}: P_{no2,p-s} = \frac{\sum_{m=1}^{M}\left|v_{no2,p-s}^{(m)}\right|^2}{2Z_0}$$

$$= \frac{kT_0B(e^{2\alpha_{p-s}z}-1)e^{-2\alpha_{p-s}z}}{M} \times \sum_{m=1}^{M}\left\{1+\left(\frac{M-m+1}{M}\right)[\cosh(\lambda z)-1]\right\}^2$$

$$= kT_0B(e^{2\alpha_{p-s}z}-1)e^{-2\alpha_{p-s}z}\cosh(\lambda z). \quad (2\text{-}54)$$

Combining equations (2-52) and (2-54), the conversion noise factor of the TVTL is thus

$$F = \frac{S_i/N_i}{S_o/N_o} = \frac{S_i}{\left|t_{p-s,s}\right|^2 S_i}\cdot\frac{\left|t_{p-s,s}\right|^2 kT_0B + P_{no1,p-s} + P_{no2,p-s}}{kT_0B}$$

$$\approx 1+\frac{1}{3}(e^{2\alpha_s z}-1)+\frac{\beta_s}{\beta_{p-s}}(e^{2\alpha_{p-s}z}-1)\frac{\cosh(\lambda z)}{\sinh^2(\lambda z)}. \quad (2\text{-}55)$$

Equation (2-55) is the lower limit of the conversion noise factor of a TVTL. It indicates that the thermal noise added by the TVTL will be only one-third of that added by the original lossy transmission line if the eigenvalue $\lambda = \xi_0\sqrt{\beta_s\beta_{p-s}}/4$ of the TVTL is sufficiently high such that the last term in equation (2-55) can be neglected.

2.4 Discussions on the conversion noise performance of TVTLs

In classical works of parametric mixers [9][44], noise analysis was carried out under the assumption that both ends of the ideal lossless TVTL were terminated with resistive loads at the converted frequency ω_{p-s}. The schematic of a 4-port circuit model is shown in Figure 2-3 (a), where the ideal loss diplexers at the input and output of the TVTL are to perform frequency combining and separation. In such case, both the thermal noise at ω_s and ω_{p-s} will enter the TVTL

from its input termination (left-hand side). Consequently, it was concluded that the lower bound of the noise figure was 3 dB at room temperature $T = 290$ K without considering the actual loss of the TVTL. In our design, we terminated the input of the TVTL with a purely reactive load at ω_{p-s} so that no thermal noise at ω_{p-s} from the source termination can flow into the TVTL, as shown in Figure 2-3 (b). As a result, an ultra-low noise figure may be achieved with a low loss TVTL at room temperature.

The noise performance of the proposed schematic in Figure 2-3 (b) has been validated with the noise figure option in the Advanced Design System (ADS) Harmonic Balanced (HB) nonlinear noise simulation. The quality factors of the simulated TVTLs were dominated by the loss of the inductors and were assumed to be 50, 100, and 200 respectively. The time-varying capacitance parameters used in the noise figure simulation, as shown in Figure 2-4. (a), were extracted from measurements of MMIC varactor diodes. In this simulation, the series resistor R_s in the varactor diode model was intentionally set to zero to better control the quality factor of the TVTL. The capacitance-versus-voltage relation of the variable capacitor $C(v)$ is shown in Figure 2-4. (b).

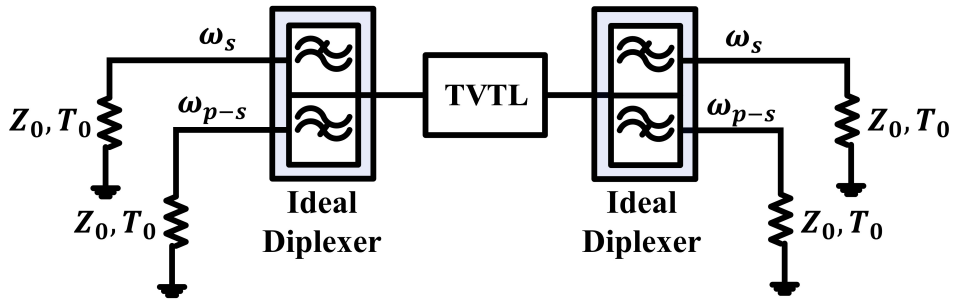

(a)

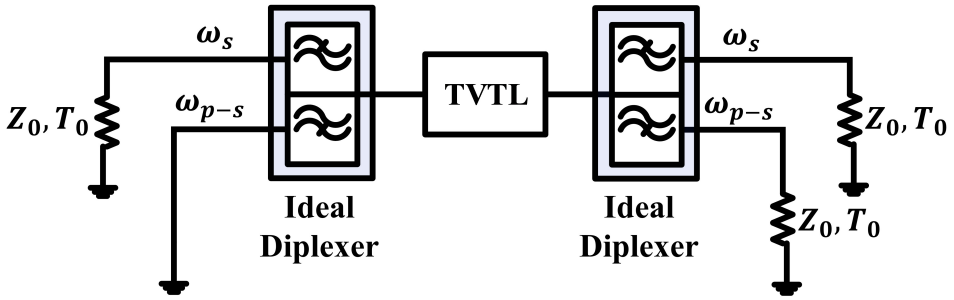

(b)

Figure 2-3 Diagram for the noise figure analysis of a traveling-wave TVTL. (a) The conventional approach where both ends of the TVTL are terminated with resistive passive terminations at the converted frequency. (b) The TVTL with its input at ω_{p-s} terminated by a pure reactive termination, e.g., a short circuit.

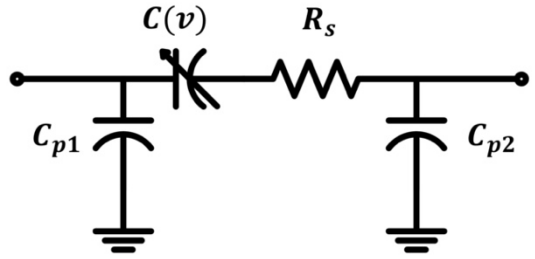

Quantity	$R_s(\Omega)$	C_{p1} (fF)	C_{p2} (fF)
Value	0	6.5	17.8

(a)

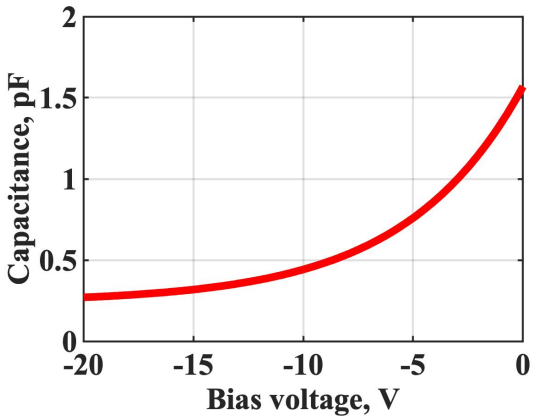

(b)

Figure 2-4 (a) Varactor diode model used in the simulation whose parameters were extracted from S-parameter measurements of MMIC varactor diodes. The series resistor R_s was set to zero to better control the quality factor of the TVTL. (b) The capacitance-versus-voltage behavior of the MMIC varactor diode.

In the simulation, the signal frequency was from 0.9 GHz to 1.1 GHz with a fixed carrier frequency at 3.4 GHz. The bandwidths of the diplexers are greater than 200 MHz. The conversion gain was around 0 dB at $f_s = 1$ GHz. As shown by the solid lines in Figure 2-6, the noise figure of the TVTL with reactive termination at ω_{p-s} dropped substantially as the increase of transmission line Q. The noise figure for $Q = 200$ was less than 0.9 dB for the simulated frequency band. Noted that with transmission line $Q = 50$, the noise figure of the TVTL was only 1.9 dB, which was already below the 3 dB limit set by the conventional approach in an ideal lossless TVTL. On the contrary, with the input of the TVTL terminated by a resistive load at ω_{p-s}, the noise figure changed very little (< 0.4 dB) with the increase of the transmission line Q, which was bounded by the 3 dB lower limit as described in [9] and [44]. Again, it must be noted that the noise figure calculation in [9, eq 50] does not consider the loss of the transmission line. To account for the signal-to-noise degradation of a lossy TVTL, equation (2-55) should be used. The case of the reactively terminated TVTL with transmission line $Q = 200$ is also included in Figure 2-5 as a reference.

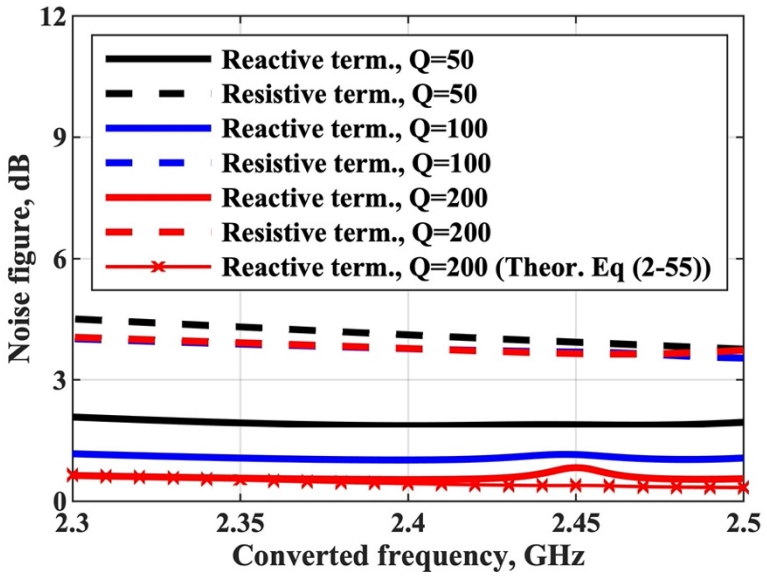

Figure 2-5 Noise figure comparisons of the TVTL with its input at ω_{p-s} terminated by a reactive termination and with its input at ω_{p-s} terminated by a resistive termination. The red line with the "cross" marks indicates the theoretical prediction of the noise figure of the reactively terminated TVTL with transmission line $Q = 200$.

The canonical definition of the noise figure assumes a lossless load at the output [48]. Consequently, the thermal noise at ω_{p-s} incident from the output load into the TVTL is not included in the common noise figure calculation. In fact, this noise may be reflected by the reactive termination at the TVTL input and be amplified as it travels back to the output, which ultimately affects the overall noise performance of the system. Interestingly, it may elevate or reduce the actual noise power appearing at the output load, depending on the phase difference between the noise generated by the load and the one reflected back to the load by the input reactive termination at ω_{p-s} of the TVTL. The phase difference, which is linearly proportional to the delay of the TVTL, can be 180° at a certain frequency so that the reflected noise voltage cancels with the original noise

voltage generated by the load at this frequency. This is much like the noise matching technique used in the low noise amplifier (LNA) design but with superiority as the noise cancellation offered by the TVTL to the next-stage load can be achieved without compromising its gain characteristics. To validate this concept, Figure 2-6. shows the schematics of two TVTL setups where the noise voltage $\bar{V}_{n,p-s}$ at ω_{p-s} is injected from the output termination into TVTL, is reflected by the reactive input termination of the TVTL, and arrives at the load. Figure 2-6. (a) depicts the desired situation where the noise voltage experiences a 180° phase shift during the process and cancels the original noise from the load. Figure 2-6. (b) illustrates the other extreme where the noise voltage experiences a 0° phase shift through the round trip due to the insertion of a quarter wavelength transmission line. The reflected noise voltage adds constructively to the original noise voltage, which degrades the noise performance of the system significantly.

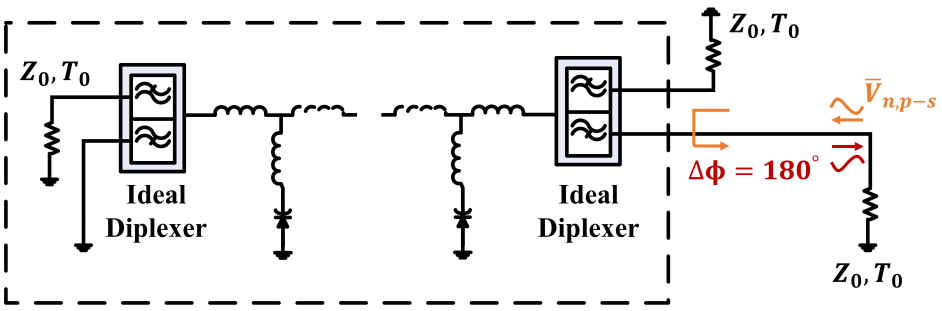

(a)

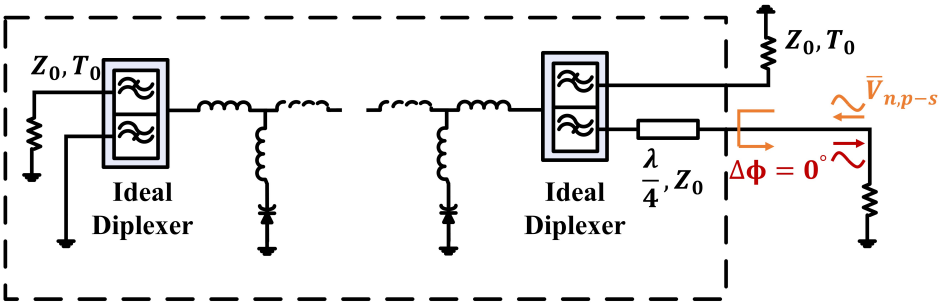

(b)

Figure 2-6 Noise contribution from the output resistive termination. (a) TVTL and its reactive input termination create a 180° phase shift so that the reflected noise voltage adds destructively to the original noise voltage $\bar{V}_{n,p-s}$ from the output resistive termination. (b) The reflected noise voltage experiences a 0° phase shift from the TVTL and its reactive input termination. It adds constructively to the original noise voltage $\bar{V}_{n,p-s}$ from the output resistive termination.

To simulate the noise performance of the overall system, both noise sources, including those upconverted from the input of the TVTL at ω_s and the noise generated from the output load of the TVTL at ω_{p-s} must be considered. Therefore, we used the RMS noise voltage option in the ADS HB nonlinear noise simulation to observe the final RMS noise voltage at the output. The TVTL was the same as the previous design with the transmission line Q of 200. The electrical length of the TVTL was 360° at around 2.4 GHz. In the simulation, both the input and output terminations were hot resistors at the room temperature of 290 K. The RMS noise voltages were calculated on the output node of the TVTL and then converted to the noise power. Figure 2-7 depicts the simulated output noise powers of the two cases in Figure 2-6. They were also compared with the resistive termination case and the thermal equilibrium case (red dashed line). No pump power was supplied in the thermal equilibrium case. It is shown that the noise power delivered to load was less than the thermal equilibrium case between 2.35 GHz to 2.45 GHz when the TVTL and its

reactive termination provides a 180° to the noise voltage. On the contrary, if the injected thermal noise experiences 0° phase shift when it arrives at the output of the TVTL, the noise power delivered to the load was much higher than the thermal equilibrium case and is even worse than the resistive input termination case. The conversion gain of all parametric mixing cases is also included in Figure 2-7 as a reference. The differences in the conversion gain within the simulated frequency were less than 0.8 dB between the resistive termination and reactive termination, while both 0° and 180° reactive terminations give the same conversion gain.

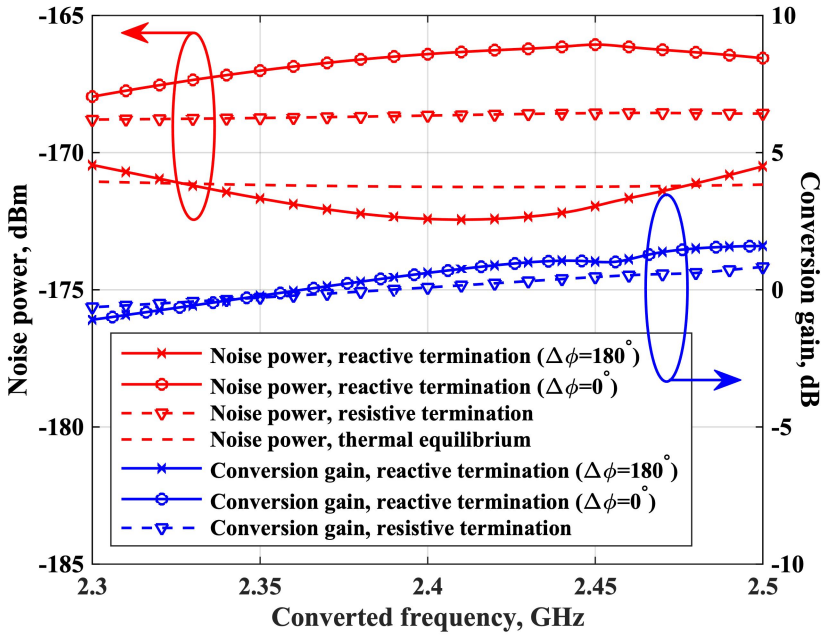

Figure 2-7 Noise figure comparisons of the TVTL with its input at ω_{p-s} terminated by a reactive termination and with its input at ω_{p-s} terminated by a resistive termination. The red line with the "cross" marks indicates the theoretical prediction of the noise figure of the reactively terminated TVTL with transmission line $Q = 200$.

Chapter 3

Monolithically Integrated Time-Varying Transmission Lines (TVTL)

It has been shown in [7] that the electromagnetic shock wave can be generated on a continuous nonlinear transmission line before any parametric mixing and amplification effect is observed. As a result, a practical TVTL needs to be achieved by periodically loading a transmission line with varactor diodes [36]-[40] as shown in Figure 3-1, where varactor diodes are to provide the time-varying capacitance in Figure 2-1. This discrete implementation is especially favorable in practice because it creates a bandgap that suppresses both the electromagnetic shock wave and the undesired intermodulation tones, particularly the one at ω_{p+s} for the single-sideband operation in the TVTL.

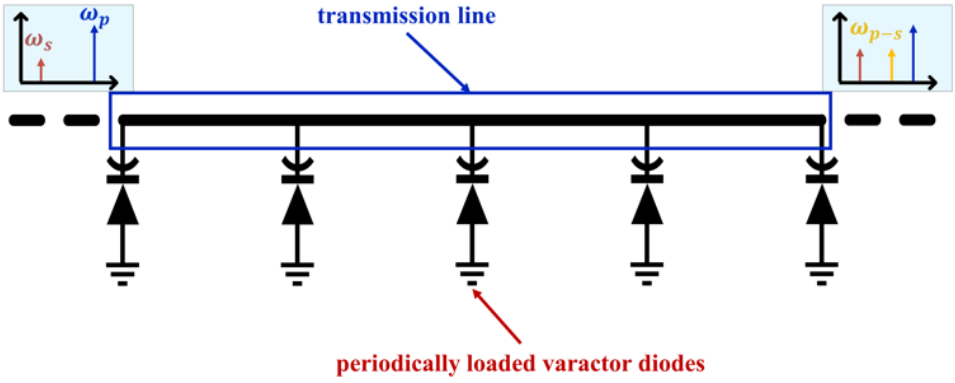

Figure 3-1 Discrete implementation of the time-varying transmission line (TVTL) where varactor diodes are periodically loaded on a transmission line. Noted that even though the single-sideband operation is illustrated in the diagram, the double-sideband operation is also feasible with this configuration.

Previous works of TVTLs [36]-[38] adopted the circuit implementation in Figure 3-1 and designed TVTLs that operated in the double-sideband mode for building non-magnetic circulators on PCB and on-chip. In this research, monolithic microwave integrated circuit (MMIC) designs of TVTL operating in the single-sideband mode are explored. Their design trade-offs and performance focusing on the parametric mixing property are analyzed in detail. This chapter includes selected TVTL designs and measured results reported in [45] and [49].

3.1 Traveling-wave time-varying transmission line (TVTL)

3.1.1 Inductor-pumped structure

The schematic in Figure 3-1 is simple to realize; however, the transmission line requires a large amount of chip area when implemented in a miniature format. Therefore, it was replaced by a series of inductors in the real MMIC designs, as shown in Figure 3-2. Moreover, the inductor pumping structure was also adopted in the MMIC designs where the varactor diode in each unit was replaced by a series LC resonator. This structure can improve the conversion gain in that it relates the voltage amplitude across the varactor diode V_c to the applied pump voltage V_p by:

$$V_c = \frac{1/j\omega_p C_0}{j\omega_p L + R + 1/j\omega_p C_0} V_p = \frac{1}{1 - \omega_p^2 L C_0 + j\omega_p R C_0} V_p. \tag{3-1}$$

where R is the series resistance of the inductor and $R << \omega_p L$ for high Q inductors. As $\omega_p^2 L C_0 \rightarrow 1$, the voltage swing across each varactor diode becomes significantly larger than V_p, resulting in an effective capacitance modulation index ξ_e:

$$\xi_e = \frac{C_1|V_c|}{C_0} = \frac{1}{\omega_p R C_0}\xi_0 = Q\xi_0. \tag{3-2}$$

which is Q times greater than that without the pumping inductor and $Q = 1/\omega_p R C_0$ is the quality factor of the series LC resonator. As indicated by equation (2-24), an increase in the capacitance modulation index, in general, leads to a higher conversion gain.

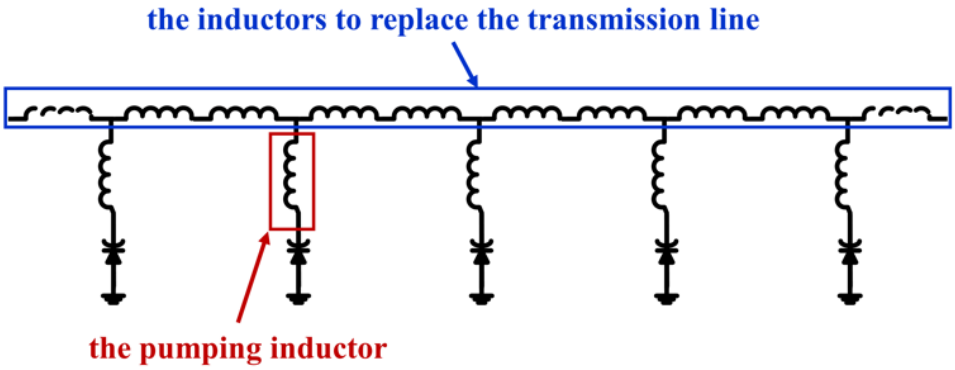

Figure 3-2 Schematic of the MMIC traveling-wave TVTL with the inductor pumping structure.

3.1.2 MMIC inductor-pumped traveling-wave TVTL

A traveling-wave TVTL was designed and fabricated with the Global Communication Semiconductors (GCS) InGaP HBT process, as shown in Figure 3-3. The overall chip size is 3.58 mm × 1.93 mm. The intended input frequency of the parametric mixer was around 1 GHz with a fixed pump/LO frequency at 3.4 GHz. The varactor diodes in this design had a value of 0.81 pF at −4.5 V. Each of the varactor diodes consists of 5 base fingers. The dimension of each base finger electrode is 10 μm × 50 μm. Their capacitance-versus-voltage behavior is shown in Figure 2-4. (b). Moreover, both the inductors replacing the transmission line and the pumping inductors were 1.0 nH. These values were chosen such that the Bloch impedance of the TVTL was

approximately 50 Ω at 1 GHz, the cutoff frequency of the TVTL was below 4.0 GHz, and the effective capacitance modulation was optimized.

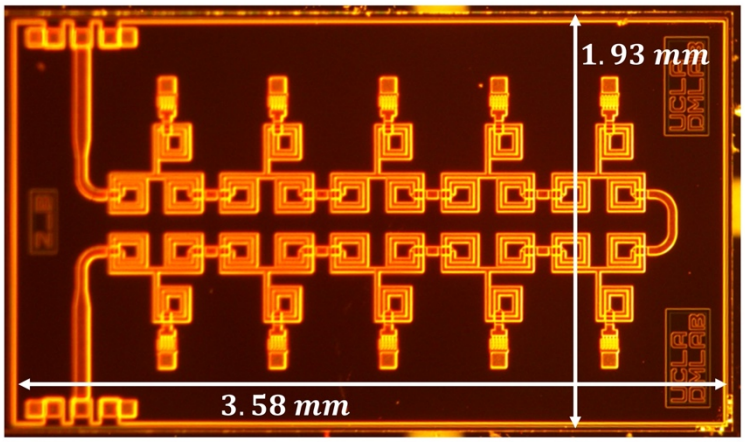

Figure 3-3 Photo of the traveling-wave TVTL.

The TVTL was first mounted onto a probe station to characterize its small-signal behavior. As shown in Figure 3-4, the measured S-parameter of MMIC TVTL was approximately cutoff at 3.8 GHz with the return loss below −10 dB when varactor diodes were biased at −4.5 V. Furthermore, the structure was well matched to 50 Ω up to 2.5 GHz.

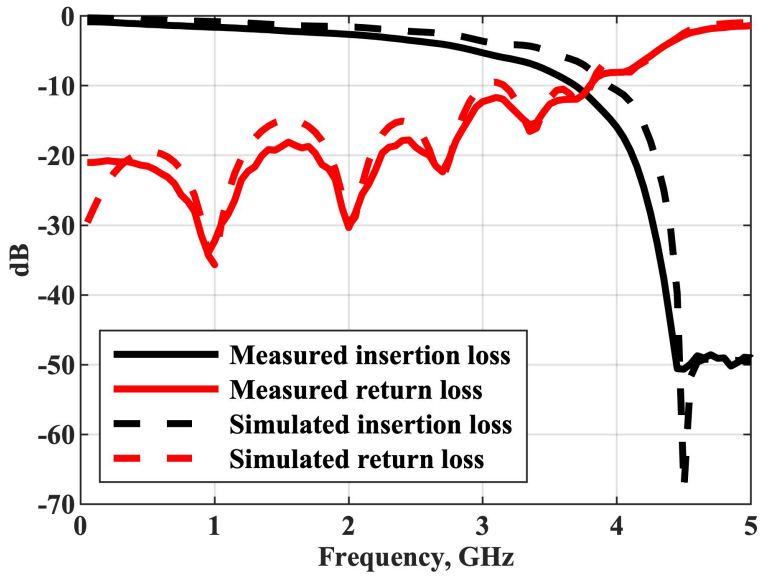

Figure 3-4 S-parameters of the MMIC traveling-wave TVTL parametric mixer with varactor diodes biased at −4.5 V.

In the conversion gain measurement, a 4-port dual-source Keysight N5241A PNA-X was used to generate the input signal of the traveling-wave TVTL parametric mixer from 0.5 GHz to 1.1 GHz. The 27.5 dBm pump signal at 3.4 GHz was also generated by the PNA-X. The two signals were then combined by an external diplexer and fed into the TVTL. At the output of the TVTL, an external triplexer was also applied to select the output frequency from 2.3 GHz to 2.9 GHz and terminated the other two tones. The loss of the lowpass filter at 1 GHz was 0.2 dB, and the loss of the bandpass filter at 2.4 GHz was 2.2 dB. The detailed measurement setup is shown in Figure 3-5. Figure 3-6 shows the power conversion performance of the traveling-wave TVTL parametric mixer. It can be observed that a small amount of conversion gain was obtained for input signal frequencies from 700 MHz to 800 MHz and from 900 MHz to 1040 MHz with varactor diodes biased at −4.5 V. The maximum conversion gain under such biasing condition was 2.1 dB at 735 MHz. Figure 3-6 also includes the theoretical prediction of the conversion gain

according to equation (2-24) and the simulation result with Advanced Design System (ADS) Harmonic Balance simulation. In the analytical prediction, a modulation index of 0.375 was used and the propagation constant was derived from the ADS simulation. The transmission line has a quality factor Q of 15 which was determined based on the simulated inductor Q value. This value was then used to compute the attenuation constant of the line. The measured conversion gain fluctuates around the theoretical prediction and simulation result, and its variation trend agrees well with them.

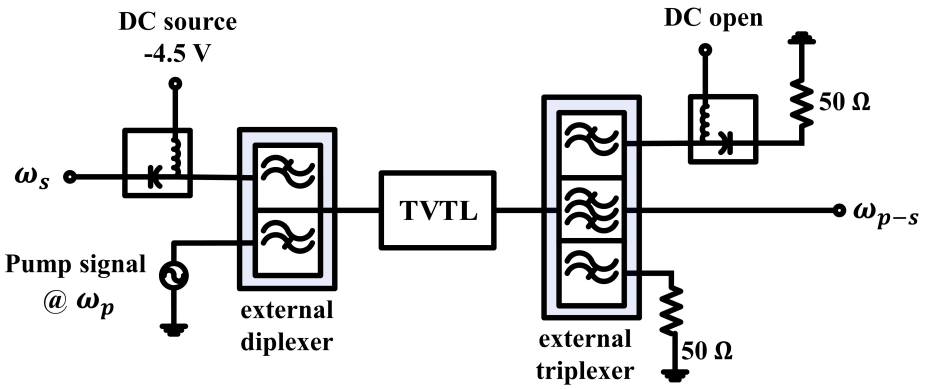

Figure 3-5 Conversion gain test setup for the MMIC traveling-wave TVTL parametric mixer.

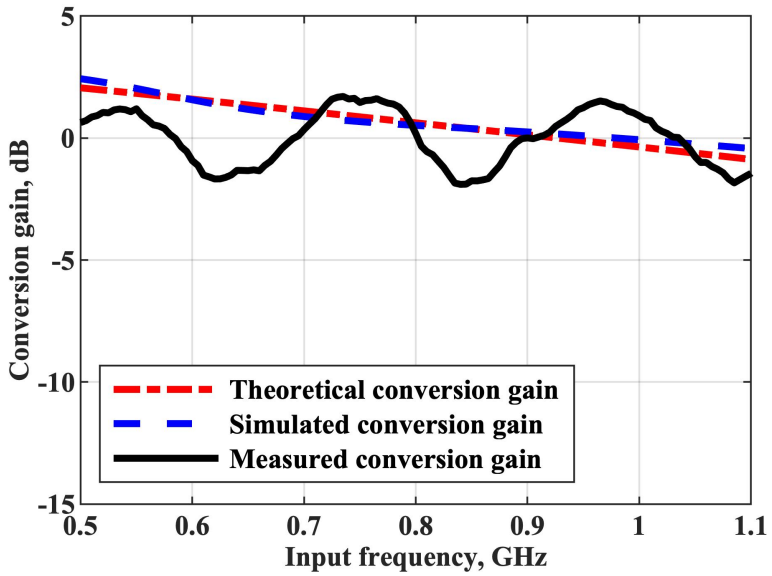

Figure 3-6 Conversion gain of the MMIC traveling-wave TVTL parametric mixer. The pump power was 27.5 dBm with the DC bias point at −4.5 V.

The noise figure of the parametric mixer was also measured with the Keysight N5241A PNA-X. The test setup was similar to the one illustrated in Figure 3-5 except an additional 25 MHz bandpass filter was inserted after the triplexer to protect the low-noise receiver in the PNA-X. In the measurement, the input signal was from 975 MHz to 1000 MHz with a power of −10.0 dBm. The pump/LO signal was at 3.4 GHz and had a power of 27.5 dBm. The varactor diodes were biased at −4.5 V. Each measurement was averaged over 8 independent sweeps by the PNA-X. It can be seen from Figure 3-7 that the mean noise figure was 2.7 dB for the entire measurement frequency. The analytical result based on equation (2-55) and the simulation result from the Advanced Design System (ADS) Harmonic Balance simulation are also attached in Figure 3-5 for comparison.

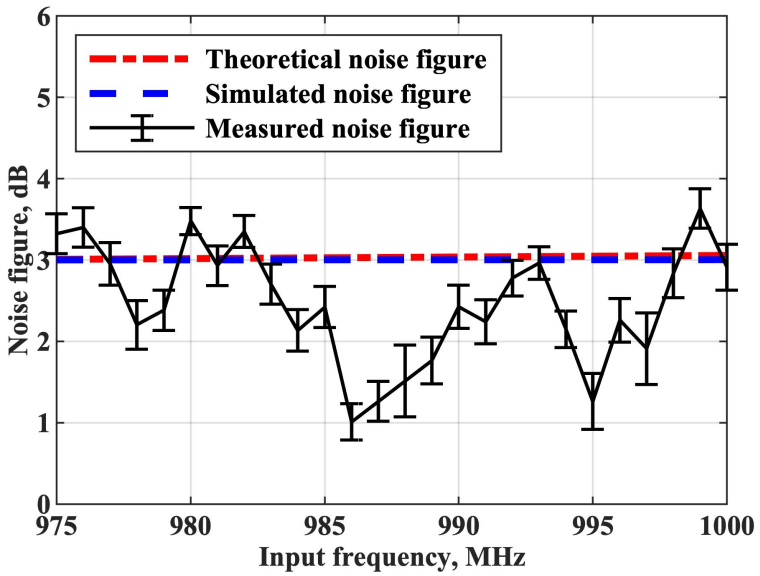

Figure 3-7 Noise figure of the MMIC traveling-wave TVTL parametric mixer, with biasing voltage at -4.5 V, pump frequency at 3.4 GHz, and pump power of 27.5 dBm.

Lastly, the output spectrum of the TVTL was captured by a Keysight N9020A signal analyzer. As shown in Figure 3-8, more than 10 dB suppression could be observed at the upper sideband at ω_{p+s} than the lower sideband at ω_{p-s}. The MMIC TVTL is approximately operating in the single-sideband mode. The P1dB and IP3 of the traveling-wave TVTL were measured with signal frequency at 1 GHz with a 27.5 dBm pump power at 3.4 GHz. The measured input-referred P1dB and input-referred IP3 were 16.0 dBm and 23.6 dBm.

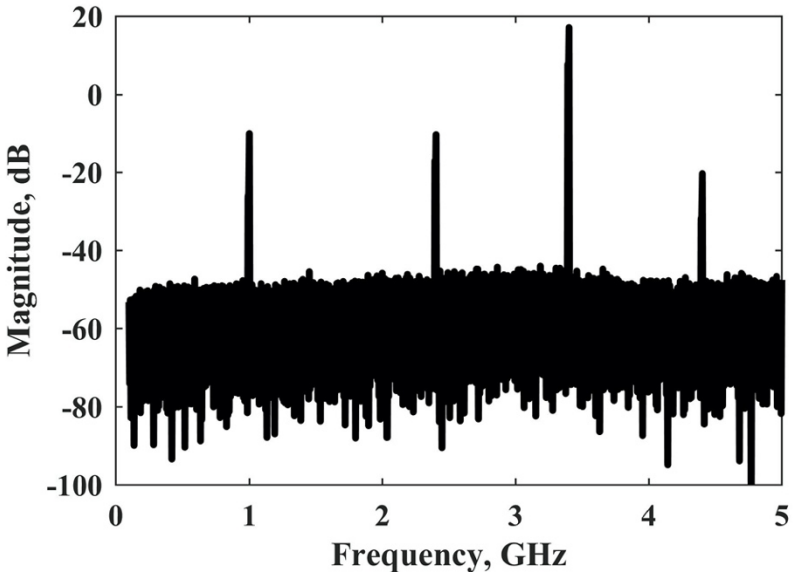

Figure 3-8 Spectrum of the MMIC traveling-wave TVTL parametric mixer output.

Similar traveling-wave TVTLs were also designed with the pump frequency at 4.5 GHz [39] [50][51]. Measurements revealed that this MMIC traveling-wave TVTL achieved a maximum of 1 dB conversion loss with 3-dB bandwidth > 400 MHz. The measured mean noise figure was 2.5dB within the frequency band of interest.

3.2 Reflective time-varying transmission line (TVTL)

The design in Figure 3-2 can offer effective frequency mixing and power conversion; however, the pump/LO power that is not converted to ω_s or ω_{p-s} is mostly wasted at the output 50 Ω termination of the TVTL. To solve this issue, a parametric mixer architecture with the reflective TVTL was proposed. The idea is illustrated in, where one end of the traveling-wave TVTL is terminated with an open circuit. A triplexer is needed to separate each frequency component. Matching networks at ω_s and ω_p are also added at the input ports to match the design to 50 Ω. In this architecture, both signals at ω_s and ω_p are reflected at the right-hand side of the

TVTL. The pump power that is not converted by the TVTL can thus be recycled by the source, which effectively reduces the amount of pump power consumed by a TVTL. Since multiple reflections involve in the reflective TVTL, its gain and noise figure performance need to be re-visited.

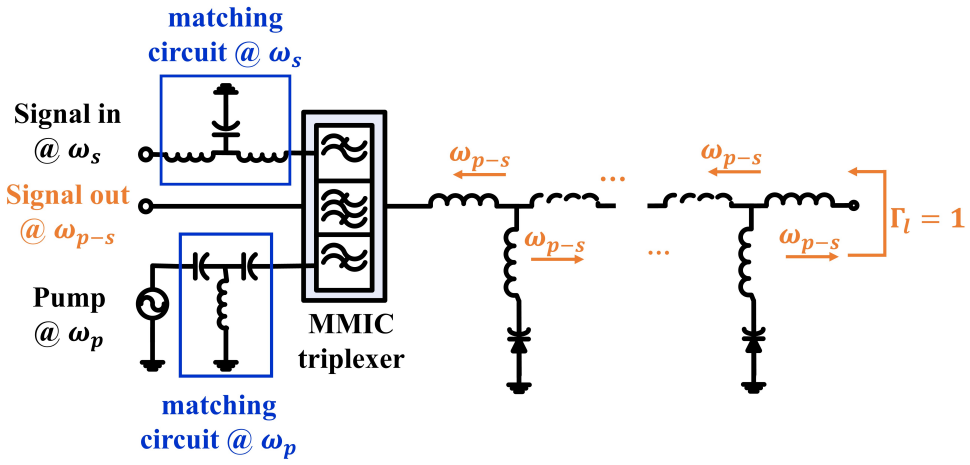

Figure 3-9 Concept of the reflective TVTL parametric mixers.

Figure 3-10 shows the equivalent circuit diagram for analyzing the conversion gain G and the noise figure F of the reflective TVTL parametric mixer. The highpass filter for the pump signal in the triplexer is neglected as it does not affect either the conversion gain or the noise power at ω_{p-s}. The remaining two filters in the triplexer and the matching network are assumed to be lossless. The traveling-wave TVTL portion of this device is designed to operate in the single-sideband condition and it has an insertion gain $G_{s,s}$ in (2-23) and a conversion gain $G_{p-s,s}$ in (2-24).

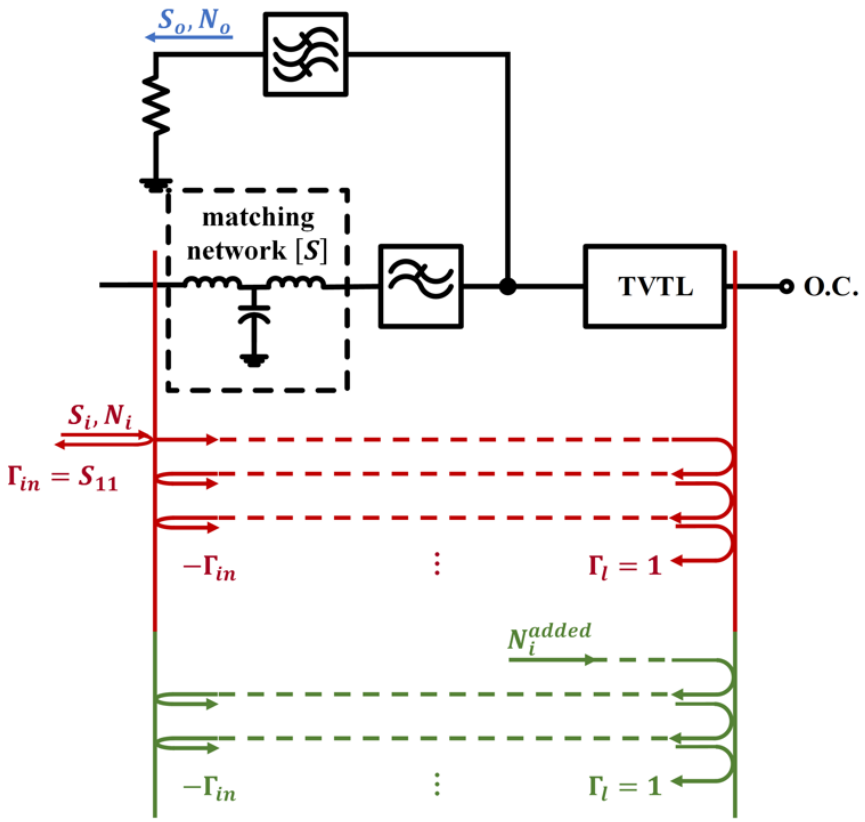

Figure 3-10 Equivalent circuit diagram of the reflective TVTL for conversion gain and noise figure analysis. The red line shows the multiple reflections of the input signal power and the input noise power, and the green line illustrates the multiple reflections of the noise power added by TVTL.

3.2.1 Conversion gain of the reflective TVTL

As illustrated in Figure 3-10 multiple reflections exist in the reflective TVTL if we analyze it in the time domain. Imagine an incident signal wave of power S_i first hits the matching network, it sees only an impedance of Z_0 since it has not yet traveled to the open circuit and cannot see its effect. As a result, the input reflection coefficient can be found by:

$$\Gamma_{in} = S_{11}. \tag{3-3}$$

where S_{11} is the reflection coefficient of the matching network alone at port 1 with its second port terminated with a matched load. The signal power transmitted through the matching network is thus:

$$S_{i,1} = (1 - |\Gamma_{in}|^2) \cdot S_i = (1 - |S_{11}|^2) S_i = \frac{|V_{si,1}|^2}{2Z_0}. \tag{3-4}$$

where $V_{si,1}$ is the magnitude of voltage transmitted through the matching network. After transmission through the matching network, the signal wave of power $S_{i,1}$ then travels along the TVTL, is reflected by the open circuit with $\Gamma_l = 1$, and travels along the TVTL again before it hits the matching network a second time. During the first round of reflections, a tone at ω_{p-s} , whose voltage can be found by equation (3-5), is generated by the TVTL. It then flows out of the network via the bandpass filter and is delivered to the load.

$$V_{so,1} = \sqrt{G_{p-s,s}} e^{j\phi_T} \cdot V_{si,1}. \tag{3-5}$$

where ϕ_T is the phase shift introduced by the TVTL, that is $\phi_T = -2\beta_s l$, and l represents the length of the open-ended TVTL. When the signal wave arrives at the matching network the second time, part of the signal wave is reflected back towards the TVTL, which creates a second round of reflections. The reflected signal voltage is:

$$V_{si,2} = |S_{11}| \sqrt{G_{s,s}} e^{j(\phi_T + \phi_M)} \cdot V_{si,1}. \tag{3-6}$$

where ϕ_M is the phase shift from the matching network. $V_{si,2}$ will result in another portion of the output signal, that is:

$$V_{so,2} = \sqrt{G_{p-s,s}} e^{j\phi_T} \cdot V_{si,2}. \tag{3-7}$$

In the kth round of reflections, one may safely conclude that:

$$V_{si,k} = \left(|S_{11}|\sqrt{G_{s,s}} e^{j(\phi_T+\phi_M)}\right)^{k-1} V_{si,1}. \tag{3-8}$$

$$V_{so,k} = \sqrt{G_{p-s,s}} e^{j\phi_T} \cdot V_{si,k}. \tag{3-9}$$

Summing $V_{o,k}$'s, the total output signal voltage is derived as:

$$\begin{aligned} V_{so} &= \sum_{k=1}^{\infty} V_{so,k} = \sum_{k=1}^{\infty} \sqrt{G_{p-s,s}} \left(|S_{11}|\sqrt{G_s} e^{j(\phi_T+\phi_M)}\right)^{k-1} V_{si,1} \\ &= \frac{\sqrt{G_{p-s,s}}}{1 - |S_{11}|\sqrt{G_{s,s}} e^{j(\phi_T+\phi_M)}} V_{si,1} \end{aligned} \tag{3-10}$$

where the product $\left|S_{11}\sqrt{G_{s,s}}\right|$ is assumed to be smaller than 1. As a result, the total output power is given by:

$$S_o = \frac{|V_{so}|^2}{2Z_0} = \frac{G_{p-s}(1 - |S_{11}|^2)}{\left|1 - |S_{11}|\sqrt{G_{s,s}} e^{j(\phi_T+\phi_M)}\right|^2} S_i. \tag{3-11}$$

Therefore, the overall conversion gain G of the parametric mixer can be found by:

$$G = \frac{S_o}{S_i} = \frac{(1 - |S_{11}|^2)}{\left|1 - |S_{11}|\sqrt{G_s}e^{j(\phi_T + \phi_M)}\right|^2} G_c. \tag{3-12}$$

At the resonance condition, the phase term in the denominator of (3-12) disappears which results in the maximum conversion gain,

$$G_{max} = \frac{(1 - |S_{11}|^2)}{\left(1 - |S_{11}|\sqrt{G_{s,s}}\right)^2} G_c. \tag{3-13}$$

When the TVTL operates in the single sideband condition, $G_{s,s}$ is greater than one. Then,

$$G_{max} > \frac{(1 - |S_{11}|^2)}{(1 - |S_{11}|)^2} G_{p-s,s} > \frac{(1 + |S_{11}|)}{(1 - |S_{11}|)} G_{p-s,s} > G_{p-s,s}. \tag{3-14}$$

Equation (3-14) indicates that G_{max} is greater than $G_{p-s,s}$ when the open-ended TVTL operates in the single-sideband condition. Moreover, due to the total reflection of the open-circuit termination, the signal wave travels equivalently twice the amount of the physical length of a traveling-wave TVTL in each round trip. This suggests that one can obtain a similar conversion gain to the traveling-wave TVTL with a much smaller area.

3.2.2 Thermal noise performance of the reflective TVTL

The input noise from the source impedance $N_i = kT_0B$ experiences the same multiple reflections and frequency conversion behavior as the input signal. The output noise power due to N_i can be obtained using the steps shown in equations (3-3)-(3-11) as:

$$N_o^{input} = \frac{G_{p-s,s}(1-|S_{11}|^2)}{\left|1-|S_{11}|\sqrt{G_{s,s}}\right|^2} kT_0B. \tag{3-15}$$

The added noise N_o^{added} comes from the thermal noise emitted by the resistive loss of the open-ended TVTL in the reflective structure. The equivalent input-referred thermal noise power for a traveling-wave TVTL is given by:

$$\begin{aligned} N_i^{added} &= (F_T - 1)kT_0B = N_{i,s}^{added} + N_{i,p-s}^{added} \\ &= \frac{1}{3}kT_0B(e^{2\alpha_s z} - 1) + kT_0B\frac{\beta_s}{\beta_{p-s}}(e^{2\alpha_{p-s}z} - 1)\frac{\cosh(\lambda z)}{\sinh^2(\lambda z)} \end{aligned} \tag{3-16}$$

where the word "input" refers to the input of the open-ended TVTL without the triplexer and the matching network. F_T is given by (2-55) which is the noise factor of a traveling-wave TVTL that is twice as long as the open-ended TVTL in the reflective structure. The first term in equation (3-16) represents the thermal noise originally generated at ω_s by the TVTL. Denote:

$$N_{i,s}^{added} = \frac{1}{3}\frac{\beta_s z}{Q_s}kT_0B = \frac{\left|v_{ni}^{added}\right|^2}{2Z_0}. \tag{3-17}$$

Since $N_{i,s}^{added}$ originates after the matching network, it first travels along the TVTL towards the open-circuit termination, is then reflected by the open circuit, and lastly arrives at the junction of the matching network, as demonstrated by the green line in Figure 3-10. Therefore, the output thermal noise voltage added by the TVTL in the k-th round of reflections can be written as:

$$v_{no,k}^{added} = \sqrt{G_{p-s,s}}\left(|S_{11}|\sqrt{G_{s,s}}\right)^{k-1} v_{ni}^{added}. \tag{3-18}$$

Summing $v_{no,k}^{added}$'s, the total output thermal noise voltage added by the TVTL is thus:

$$v_{no}^{add} = \sum_{k=1}^{\infty} v_{no,k}^{added} = \frac{\sqrt{G_{p-s,s}}}{1 - |S_{11}|\sqrt{G_{s,s}}} v_{ni}^{added}. \tag{3-19}$$

which leads to the output added thermal noise power, that is:

$$N_{o,s}^{added} = \frac{|v_{no}^{add}|^2}{2Z_0} = \frac{G_{p-s,s}}{\left|1 - |S_{11}|\sqrt{G_{s,s}}\right|^2} \frac{1}{3} kT_0B(e^{2\alpha_s z} - 1). \tag{3-20}$$

The second term in equation (3-16) represents the thermal noise directly emitted at ω_{p-s}. Since it is directly delivered to the load at the output, the output added thermal noise power from this portion of input thermal noise is:

$$N_{o,p-s}^{added} = G_c N_{i,p-s}^{added} = kT_0B(e^{2\alpha_{p-s} z} - 1)e^{-2\alpha_{p-s} z} \cosh(\lambda z). \tag{3-21}$$

Therefore, the overall thermal noise factor of the parametric mixer under the available gain condition can be found by:

$$\begin{aligned} F &= \frac{S_i/N_i}{S_o/N_o} = \frac{S_i}{S_o} \cdot \frac{N_o^{input} + N_{o,s}^{added} + N_{o,p-s}^{added}}{N_i} \\ &= 1 + \frac{1}{3} kT_0B(e^{2\alpha_s z} - 1) \cdot \frac{1}{1 - |S_{11}|^2} + \frac{(1 - e^{-2\alpha_{p-s} z}) \cosh(\lambda z)}{G}. \end{aligned} \tag{3-22}$$

where G is the overall conversion gain of the parametric mixer in equation (3-12). When G is sufficiently large, the third term in equation (3-22) is negligible. Then, equation (3-22) indicates that the noise figure of the reflective TVTL is worse than F_T even if the matching network and triplexer are lossless. The best case happens when $|S_{11}|^2 = 0$, i.e., no matching network exists. This suggests that there is a trade-off between conversion gain and noise figure in the reflective TVTL structure. The matching network guarantees the maximum power transfer between the input

at ω_s and the traveling-wave TVTL resulting in a maximum conversion gain, however, it also creates multiple reflections between the input port and the TVTL which degrades the overall signal-to-noise ratio.

3.2.3 MMIC reflective TVTL

A reflective TVTL was designed in the Advanced Design System (ADS) with the Global Communication Semiconductors (GCS) InGaP HBT varactor diodes. This reflective TVTL parametric mixer consists of a three-unit traveling-wave TVTL, and it is compared with a six-unit traveling-wave TVTL in the simulation. The input signal frequency was at 1 GHz with a fixed pump/LO frequency of 4.8 GHz. In both TVTLs, the varactor diodes had a mean capacitance of 0.52 pF at the bias voltage of -4 V. The two TVTLs were both simulated with the ADS Momentum simulation to include the actual loss. Figure 3-11 shows the simulation results of the two TVTL parametric mixers. For a fair comparison, the pump power was set to 19 dBm in both cases. The conversion gain of the reflective TVTL increased by more than 3 dB compared with the corresponding traveling-wave TVTL from 0.95 GHz to 1.05 GHz. A maximum of 7.8 dB gain improvement was obtained at the designed frequency of 1 GHz. The bandwidth of the reflective TVTL, however, was compromised because the matching circuits were intrinsically narrowband. The gain-bandwidth trade-offs in parametric amplifiers have been discussed in [52]-[55] from the perspective of coupling multiple resonances. The reflective TVTL implementation allows a similar trade-off to be formed from the perspective of the transmission line by creating multiple reflections on the transmission line. A high-Q TVTL would allow higher gain yet at the price of reduced bandwidth. Besides, reflective TVTL can be made with a smaller form factor that favors on-chip implementation.

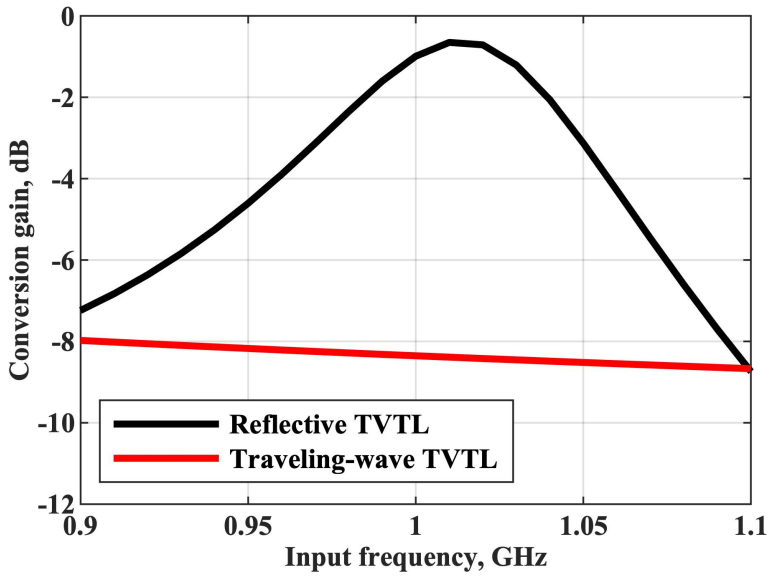

Figure 3-11 Comparison of the simulated conversion gain between the reflective TVTL parametric mixer and the corresponding traveling-wave TVTL parametric mixer. Both TVTLs were simulated with the Advanced Design System (ADS) Momentum simulation to include their actual loss. For a fair comparison, the pump power was set to 19 dBm for both cases.

An MMIC reflective TVTL was then fabricated with the GCS InGaP HBT process (shown in Figure 3-12). The overall chip size is $3.23\ \text{mm} \times 2.43\ \text{mm}$. In this design, the triplexer is embedded on-chip, which takes up most of the chip area. The traveling-wave TVTL only consumes one-fifth of the chip area. Due to the phase sensitivity of the narrowband matching networks, the biasing voltage of the varactor diodes was modified to -3 V in the measurement to get a reasonably good return loss at 1 GHz. The matched point of the pump shifted to 4.6 GHz under such a biasing condition. The measured return loss was more than 8 dB for the input frequency from 0.95 GHz to 1.05 GHz as shown in Figure 3-13. The return loss for the pump signal was 12.6 dB at 4.6 GHz.

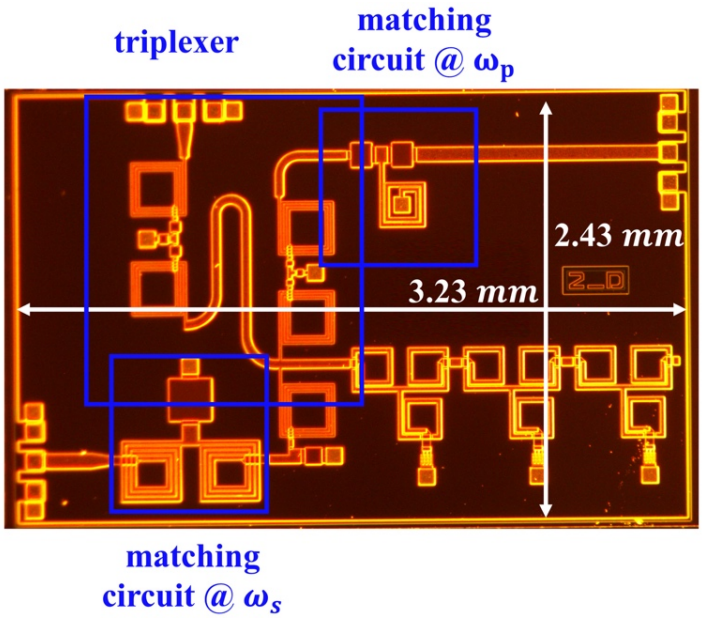

Figure 3-12 Photo of the parametric mixer with the reflective TVTL.

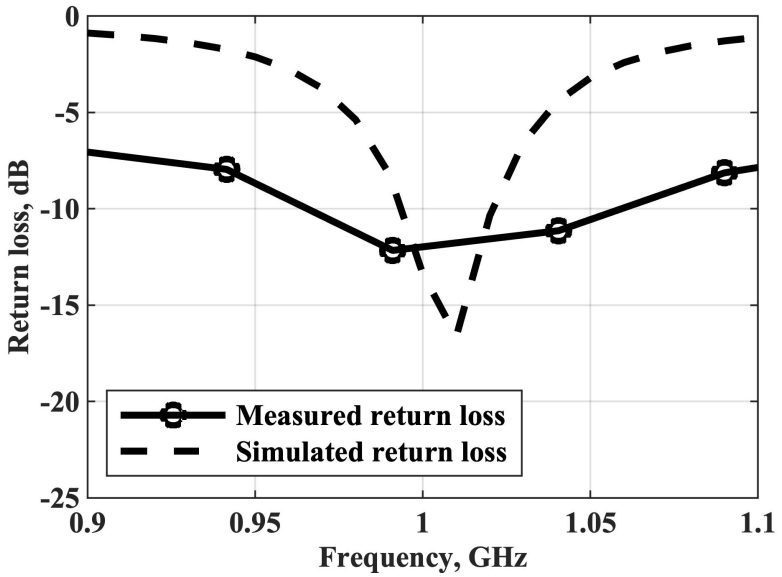

Figure 3-13 Return loss of the MMIC reflective TVTL parametric mixer.

Since the design had a triplexer on-chip, the setup of the conversion gain measurement was much simpler, as illustrated in Figure 3-14. During the conversion gain measurement, 19.9 dBm

pump power was applied. The measured conversion gain, in comparison with the theoretical prediction and simulation result, is shown in Figure 3-15. More than 0 dB conversion gain was measured from 1002 MHz to 1024 MHz, and the peak conversion gain was 0.48 dB at 1009 MHz. Noted that this conversion gain included a 2.5 dB loss of the triplexer. The 3-dB bandwidth of the parametric mixer was 70 MHz.

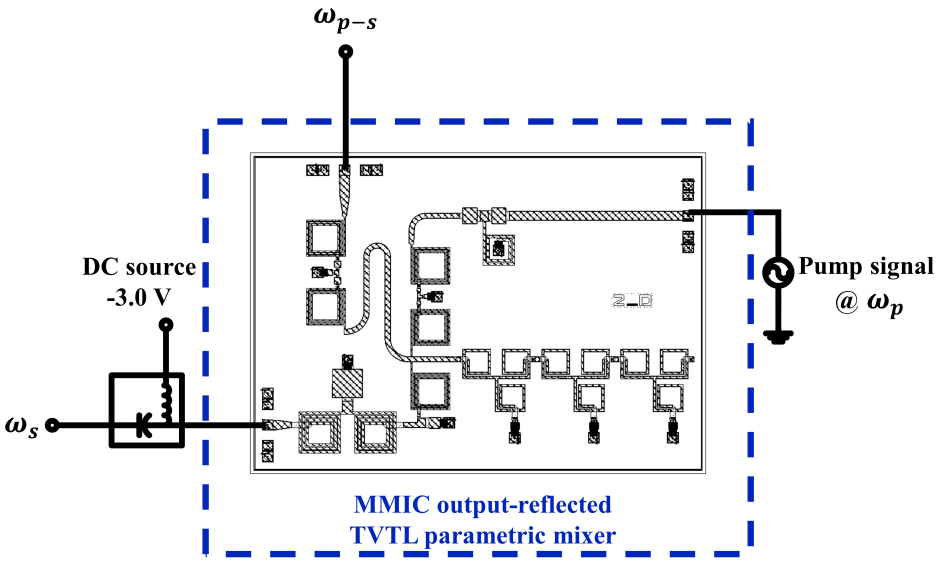

Figure 3-14 Conversion gain test setup for the reflective MMIC TVTL parametric mixer.

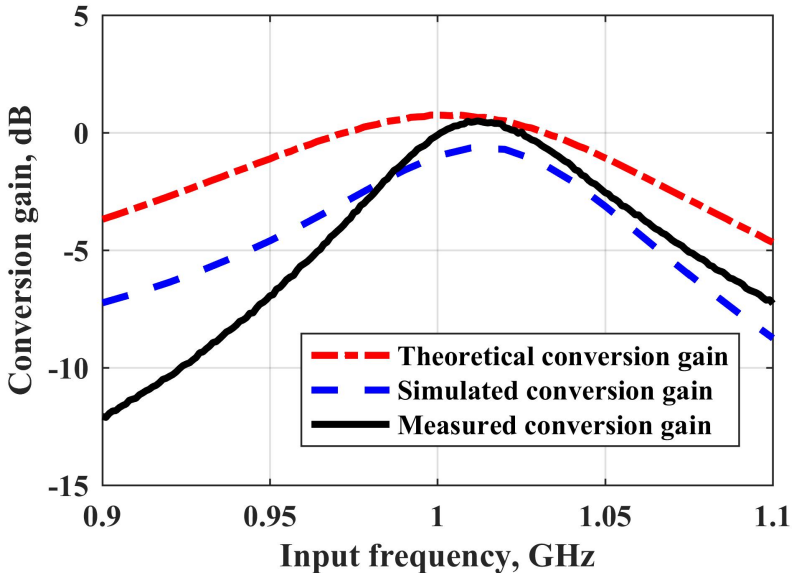

Figure 3-15 Conversion gain of the MMIC reflective TVTL parametric mixer.

The noise figure of the parametric mixer with the reflective TVTL was also measured with a bias voltage of −3 V and a pump signal of power 19.9 dBm at 4.6 GHz. The input signal was from 995 MHz to 1025 MHz with an input power of −10.0 dBm. It can be seen from Figure 3-16 that the overall noise figure including the matching network and the triplexer was below 7 dB within the whole measurement bandwidth, and a minimum of 5.9 dB noise figure was observed at 1020 MHz. The measured results also compared well with the analytical result and the simulation result. In Figure 3-17, the spectrum at the output of the reflective TVTL mixer is captured, which shows about 13 dBm residue pump power but indeed a single-sideband operation as the upper sideband is well suppressed. Lastly, the P1dB and IP3 of the reflective TVTL were measured with signal frequency at 1 GHz with a 19.9 dBm pump power at 4.6 GHz. The measured input-referred P1dB and input-referred IP3 were −4.0 dBm and 6.0 dBm.

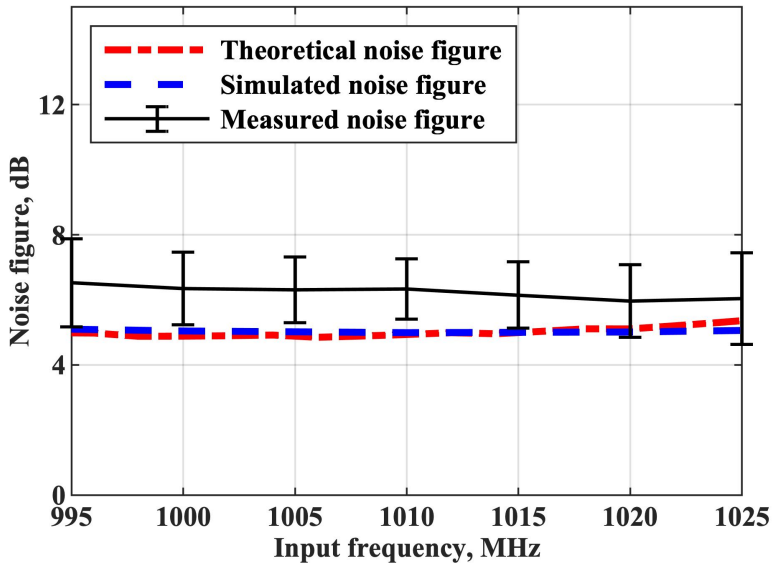

Figure 3-16 Noise figure of the MMIC reflective TVTL parametric mixer.

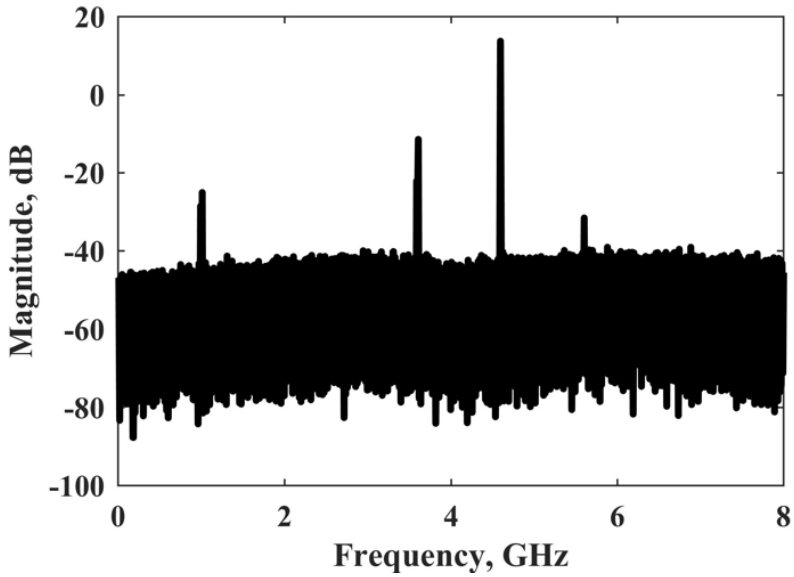

Figure 3-17 Spectrum of the MMIC reflective TVTL parametric mixer output.

The measured results imply that there is a trade-off between conversion gain, the bandwidth, and the noise figure in the reflective TVTL parametric mixer which designers must consider carefully

in order to obtain the optimal performance. Furthermore, the triplexer in this proof-of-the-concept design was implemented on-chip which has a relatively high resistive loss due to the poor quality factor of inductors in the MMIC process. If a triplexer with better technology such as the SAW/BAW was in use, the overall noise figure of the parametric mixer would be further improved.

3.3 Directly-pumped time-varying transmission line (TVTL)

The reflective TVTL shown in Figure 3-9 can significantly reduce the amount of power consumed by the 50Ω termination at the output of the traveling-wave TVTL, however, it also results in performance degradation in noise figure and bandwidth. Moreover, the non-zero transmission line loss in previous TVTL configurations leads to decaying pump power, i.e., decreasing modulation index, as the pump travels along the TVTLs. Consequently, the overall conversion gain of the TVTLs gets impaired. Worse still, triplexers are always required to combine/separate the signal ω_s, the converted band ω_{p-s}, and the pump ω_p in the previous two TVTL configurations, adding additional loss and noise to the system. To overcome all these challenges, the directly-pumped TVTL is proposed where single balanced diode bridges are adapted to replace the single-ended varactor diodes in Figure 3-2 and Figure 3-9. The schematic of the directly-pumped TVTL is shown in Figure 3-18, where the red section represents the directly pump TVTL unit cells while the black section denotes the circuitry for the pump. In this configuration, the pump power no longer travels along the TVTL. Instead, it is directly applied at the center of the diode bridges. Consequently, the amplitude of the pump is not influenced by the loss of the transmission line, and the modulation index can remain unchanged across all units of the directly-pumped TVTL. More importantly, the diode bridge provides intrinsic isolation between the pump port and the signal port, so theoretically, there is no pump power wasted on

either the transmission line loss or the 50Ω load at the output. Nevertheless, one must be noted that for the directly-pumped TVTL to function properly, the phase match condition in equation (2-9) must be satisfied. For a simpler implementation, we first set the phase difference of the pump $\Delta\phi_p$ to be 90° between two adjacent cells. Then, we design the values of the inductors and varactor diodes such that the phase difference ($\Delta\phi_s$) at ω_s between adjacent cells follows

$$\Delta\phi_s = 90^\circ \times \frac{\omega_s}{\omega_p}. \tag{3-23}$$

Lastly, the desired progressive phases of the pump that emulate a traveling wave propagation can be achieved by first splitting the pump power with a 90° hybrid and then differentiating each branch with a balun.

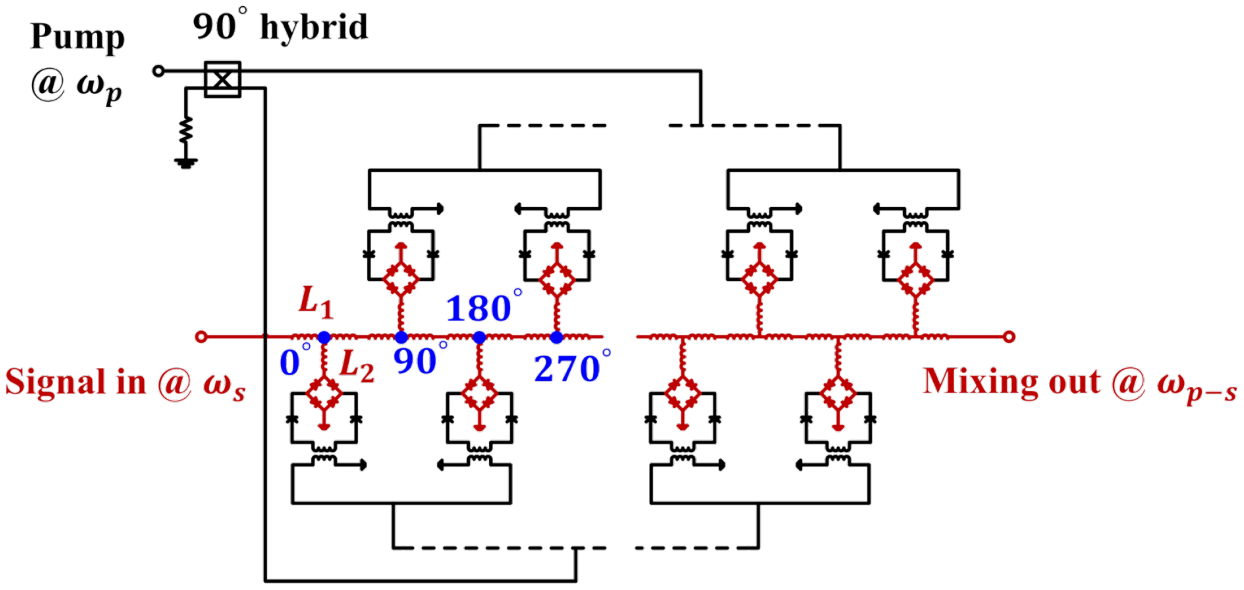

Figure 3-18 Circuit diagram of the directly-pumped TVTL. The red parts are the baluns and dividers for the pump path and the black part denotes the sections of TVTL.

Noted that the directly-pumped TVTL also possesses the traveling wave behavior so the gain and noise analyses in Chapter 2 apply.

3.3.1 MMIC 3D solenoid inductor

In addition to the power consumption issue, Ohmic loss was another challenge faced by the MMIC TVTL designs as the quality factor Q of on-chip inductors is usually very poor. Therefore, we employed a novel on-chip solenoid inductor structure [56] in the MMIC directly-pumped TVTL design to enhance the overall performance of the directly-pumped TVTL. Unlike the conventional spiral inductors whose resistive loss increases nonlinearly with the increase of the number of turns N, the Ohmic loss of the solenoid inductors scales linearly with N. As a result, Q of the solenoid inductor does not degrade as fast as that of the spiral inductor. Figure 3-19 shows the 3D structure of the vertical solenoid inductor, where vias are used to connect the top and bottom signal traces at the two sides of a $150\mu m$ GaAs substrate. The bottom ground plane metal around the solenoid inductor is removed to accommodate the signal traces on the bottom layer.

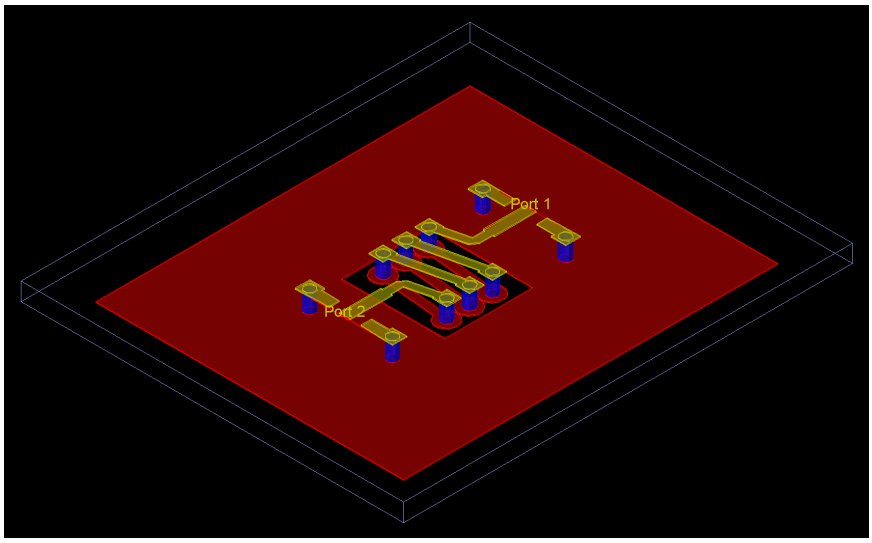

(a)

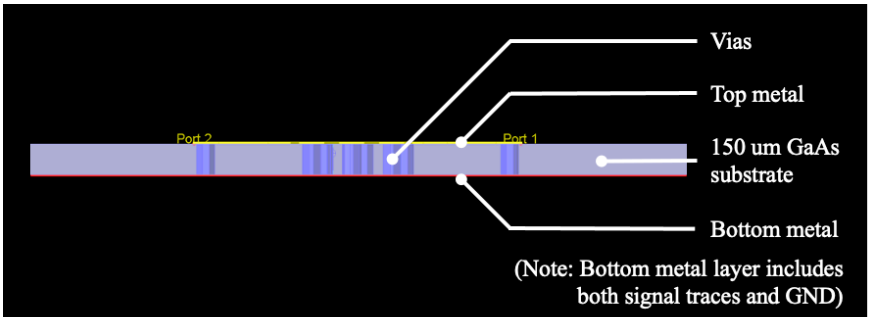

(b)

Figure 3-19 (a) 3D view of the solenoid inductor. The bottom ground metal (the red sheet in the diagram) around the solenoid inductor is removed for to accommodate the bottom signal traces. (b) Side view of the solenoid inductor.

For proof of concept, a 2.2 nH solenoid inductor along with its spiral counterpart was fabricated with the Advanced Wireless Semiconductor Company (AWSC) GaAs process. Their parameters were then extracted from measured S-parameters. During the measurement, both inductors were mounted onto the probe station and tested by a 4-port Keysight N5241A PNA-X to obtain their S-parameters. Then a series RL circuit model, as shown in Figure 3-20. (a), is used to extract their inductance and quality factor. Figure 3-20. (b)-(c) shows the measured inductance and quality factor of both inductors. As shown in Figure 3-20. (c), the quality factor of the solenoid inductor is $Q = 22$ at $1GHz$, whereas the quality factor of the spiral inductor is only $Q = 13$ at $1GHz$. This corresponds to a 69% increase in the quality factor.

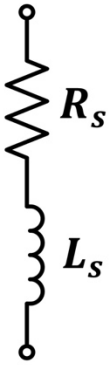

(a)

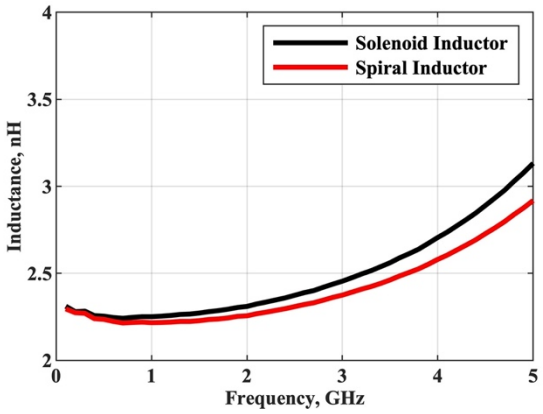

(b)

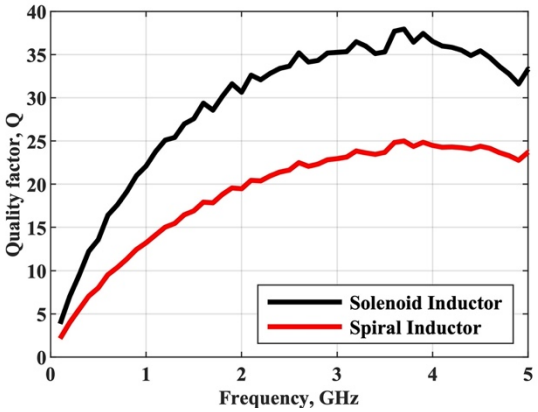

(c)

Figure 3-20 (a) Circuit model for inductance characterization; (b) Inductance of the 2.2 nH solenoid inductor and its spiral inductor counterpart; (c) Quality factor of the 2.2 nH solenoid inductor and its spiral inductor counterpart.

3.3.2 MMIC directly-pumped TVTL

The directly-pumped TVTL parametric mixer was designed and fabricated with the Advanced Wireless Semiconductor Company (AWSC) GaAs process. The photo of the chip is shown in Figure 3-21. The overall chip size is 11.56 mm × 6.8 mm.

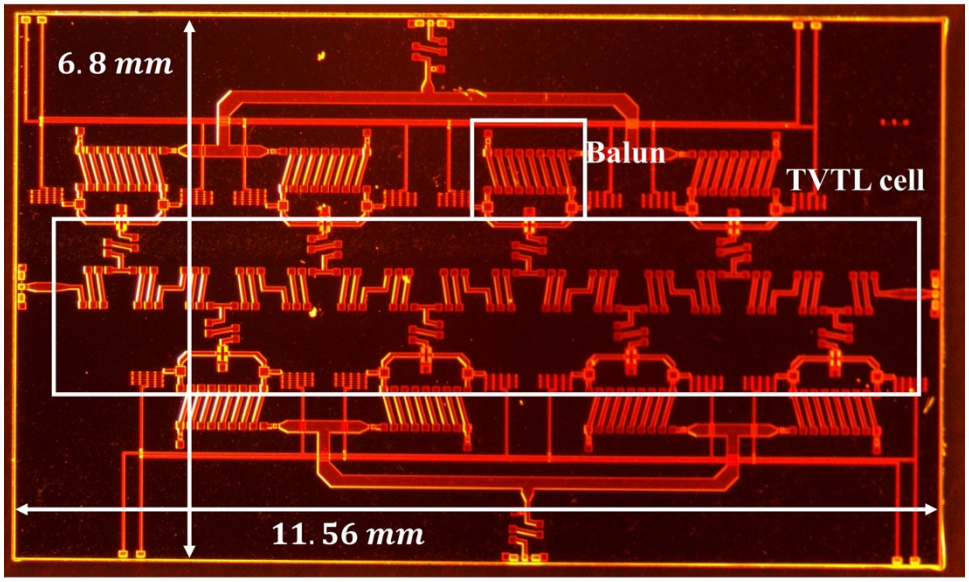

(a)

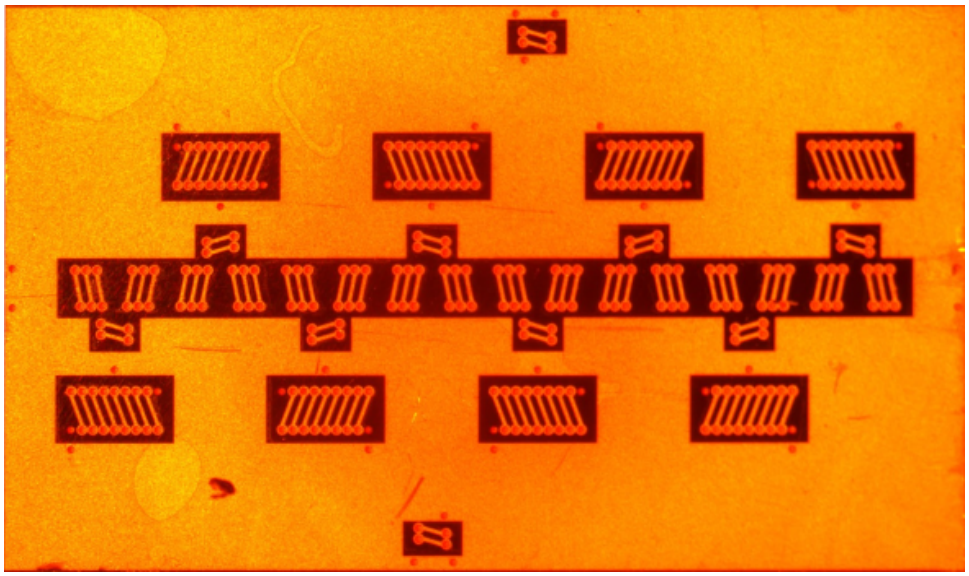

(b)

Figure 3-21 Photo of the MMIC directly-pumped TVTL with 3D solenoid inductors. (a) Top view of the MMIC directly-pumped TVTL; (b) Bottom view of the MMIC TVTL.

In this design, T-junction power dividers and baluns were implemented on-chip to supply the differential pump of the varactor diode bridge. Each varactor diode consists of 5 base fingers, and the dimension of each base finger electrode is $4\ \mu m \times 60\ \mu m$. The bias voltage across a single diode was selected to be -5.0 V to obtain an optimal capacitance variation ratio. Its circuit model and the capacitance-versus-voltage behavior are plotted in Figure 3-22. Noted that varactor diode bridges were implemented in the directly-pumped TVTL, so the bias voltages of the complete diode bridges should be ± 5.0 V. The signs of the bias voltages are determined such that each diode in the diode bridge is reversed biased. Moreover, the values of inductors in Figure 3-18 are $L_1 = 2.1$ nH and $L_2 = 1.1$ nH. These values are chosen such that the Bloch impedance of the TVTL was approximately $50\ \Omega$ at 1 GHz, the converted band ω_{p-s} into fall into the passband, and equation (3-23) is satisfied.

Similarly, the directly-pumped TVTL was first mounted onto a probe station to characterize its small-signal behavior. The S-parameters of the directly-pumped TVTL are shown in Figure 3-23. The cutoff frequency of the design was approximately at 3 GHz with $S21 = -10$dB. Since the pump does not propagate along the TVTL, we can let the cutoff frequency be smaller than the pump frequency ω_p without affecting the conversion gain performance. Moreover, the condition of the single-sideband operation is easier to obtain in the directly-pump TVTL as the upper sideband of the converted tone ω_{p+s} gets more suppression compared to the traveling-wave configuration.

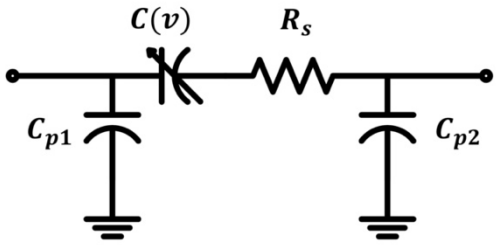

Quantity	$R_s(\Omega)$	C_{p1} $(f\mathrm{F})$	C_{p2} $(f\mathrm{F})$
Value	2.57	5.6	5.85

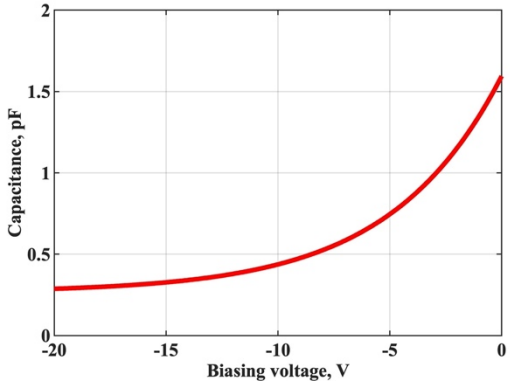

(a) (b)

Figure 3-22 (a) Varactor diode model used in the directly-pumped TVTL design. (b) The capacitance-versus-voltage behavior of the 5×4 μm $\times$ 60 μm MMIC varactor diode.

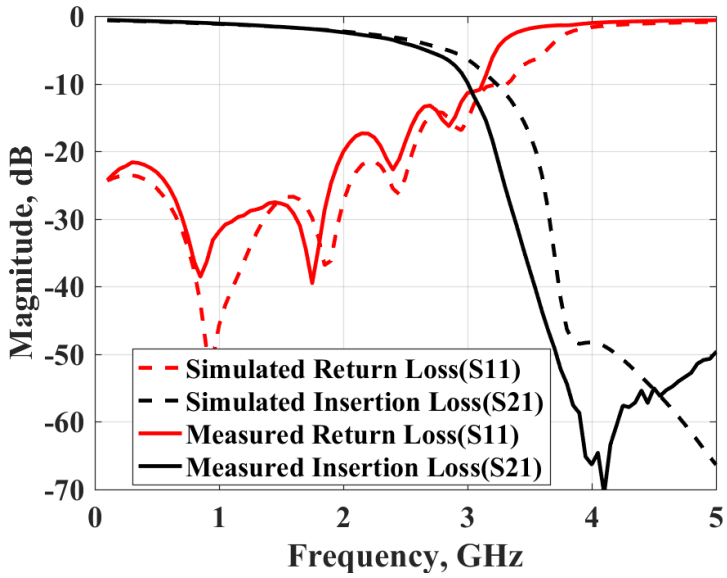

Figure 3-23 S-parameter of the directly-pumped TVTL with varactor diodes biased at -5.0 V.

In the insertion gain and conversion gain measurement, a 4-port dual-source Keysight N5241A PNA-X was used to generate the input signal of the directly-pumped TVTL parametric

mixer from 600 MHz to 1100 MHz with a power of −10 dBm. The pump was at 3.2 GHz with a power of 31.1 dBm. It was generated by a signal generator and amplified to the desired power level with a power amplifier. A 90° hybrid was used after the power amplifier to provide the desired phase difference across adjacent diode bridges. The complete measurement setup is shown in Figure 3-24.

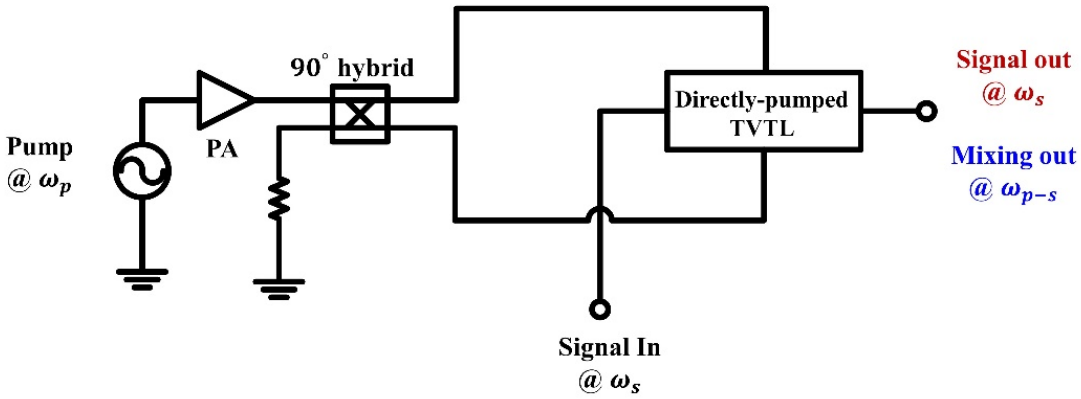

Figure 3-24 Conversion gain test setup for the MMIC directly-pumped TVTL parametric mixer.

Figure 3-25 shows the parametric amplification and conversion behavior of the directly-pumped TVTL. They are plotted with respect to the input frequency ω_s. More than 1.4 dB insertion gain and 1.8 dB conversion gain were observed for the entire measured signal frequency band. A peak conversion gain of 4.2 dB was achieved at 600 MHz. Figure 3-25 also includes the theoretical and simulation predictions of the insertion gain and conversion gain. The theoretical results were computed using equation (2-23) and equation (2-24) together with a $e^{-\alpha z}$ term to take into account of the actual loss of the TVTL. Simulations were carried out with the Advanced Design System (ADS) Harmonic Balance simulation.

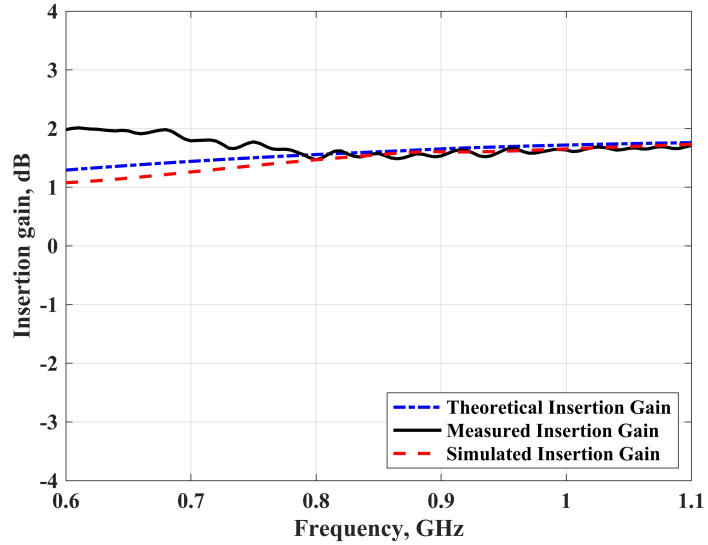

(a)

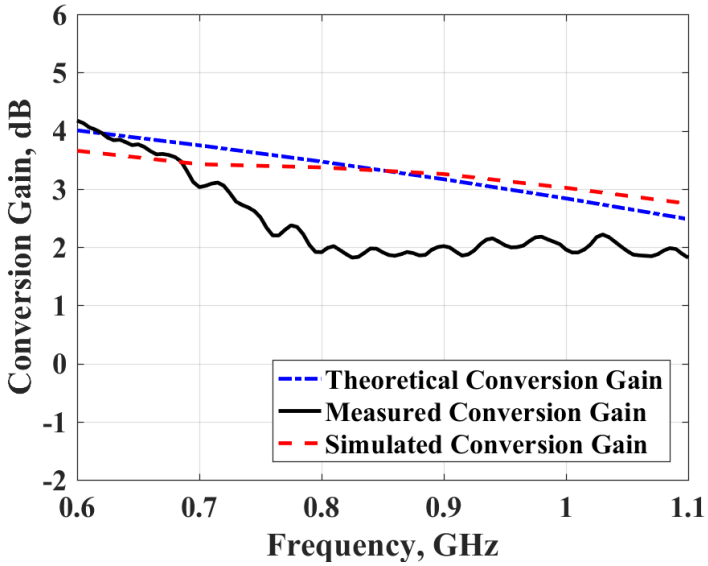

(b)

Figure 3-25 (a) Insertion gain of the directly-pumped TVTL; (b) Conversion gain of the directly-pumped TVTL with varactor diode bridges biased at ± 5.0 V. The pump is at 3.2GHz with a power of 31.1dBm.

The noise figure of the directly-pumped TVTL parametric mixer was measured with the built-in amplifier and converter noise figure function of the Keysight N5241A PNA-X. The test setup was similar to the one illustrated in Figure 3-24 except an additional high Q bandpass filter at 2355 MHz was added at the output of the directly-pumped TVTL in the conversion noise figure measurement to protect the low-noise receiver in the PNA-X. In the insertion noise figure measurement, the input signal was from 1.0 GHz to 1.2 GHz, while in the conversion noise figure measurement, the input signal was from 842.5 MHz to 847.5 MHz. Both noise figures were measured with an input signal power of -10.0 dBm. The pump/LO signal was at 3.2 GHz and had a power of 31.1 dBm. The varactor diode bridges were biased at ± 5.0 V. It can be seen from Figure 3-26 that the mean insertion noise figure and conversion noise figure were 1.8 dB and 3.0 dB respectively. The analytical results based on equation (2-49) and equation (2-55) and the simulation results from the ADS Harmonic Balance nonlinear noise simulation are also attached in Figure 3-26 for comparison.

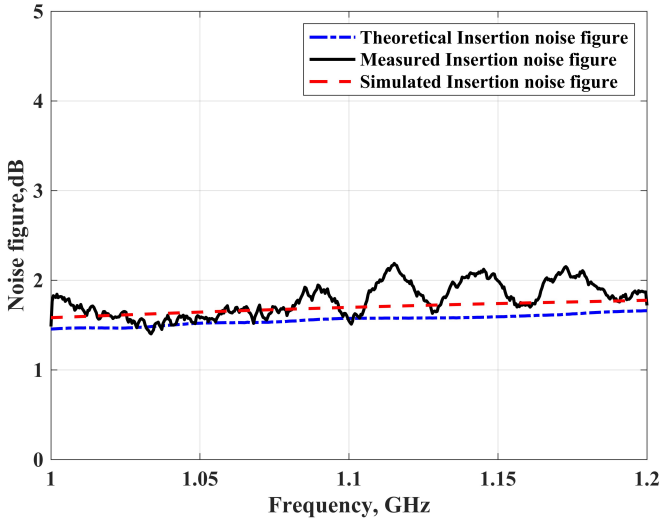

(a)

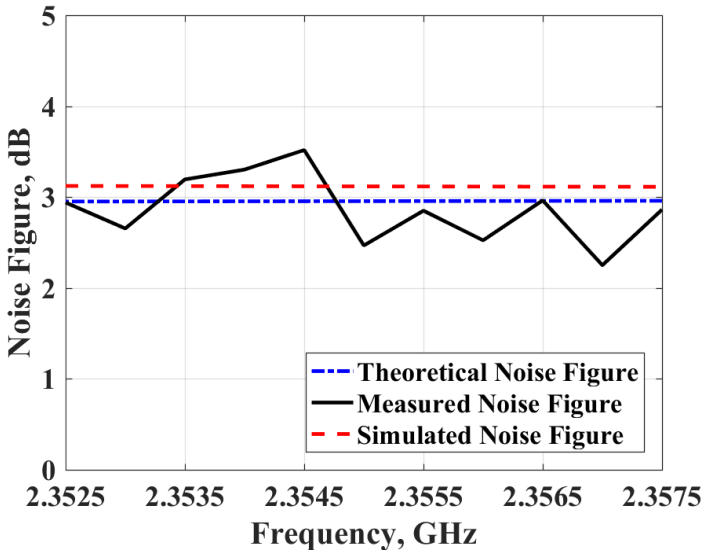

(b)

Figure 3-26 (a) Insertion noise figure of the directly-pumped TVTL; (b) noise figure of the directly-pumped TVTL with varactor diode bridges biased at ± 5.0 V and a 31.1 dBm pump at 3.2 GHz.

Figure 3-27 depicts the output spectrum of the directly-pumped TVTL measured with a Keysight N9020A signal analyzer. It was carried out with a -10 dBm signal at 845 MHz and a 31.1 dBm pump at 3.2 GHz. As shown in Figure 3-27, the upper sideband ω_{p+s} is 14 dB lower than that of the lower sideband at ω_{p-s}, and the MMIC directly-pumped TVTL is approximately operating in the single-sideband mode. In addition, more than 35 dB of pump power suppression was realized in the directly-pumped TVTL parametric mixer. The P1dB and IP3 of the directly-pumped TVTL were measured with signal frequency at 845 MHz with a 31.1 dBm pump power at 3.2 GHz. The measured input-referred P1dB and input-referred IP3 were 12.0 dBm and 22.5 dBm.

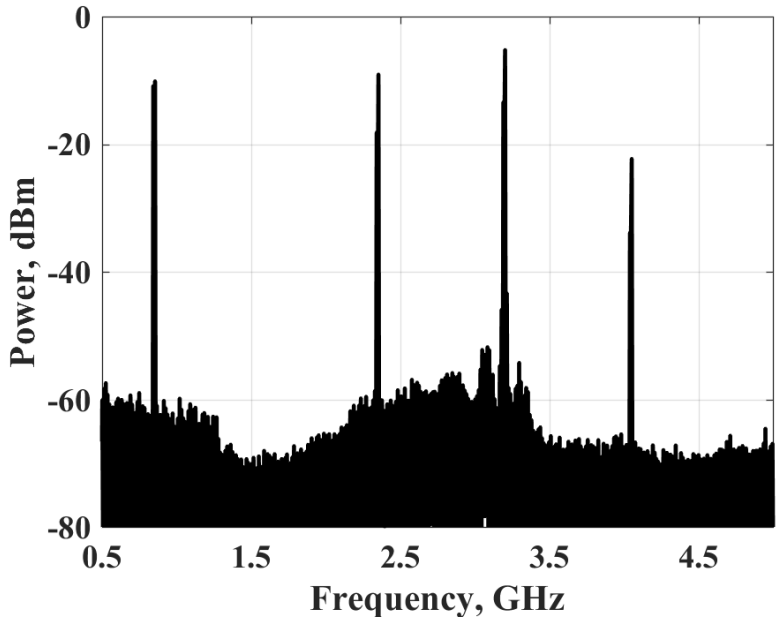

Figure 3-27 Measured spectrum at the output of the directly-pumped TVTL with varactor diode bridges biased at ± 5.0 V, signal power of -10 dBm at 845 MHz, and pump power of 31.1 dBm at 3.2 GHz.

3.4 Comparison with state-of-the-art mixers

The parametric mixing performance of the designed MMIC TVTL was also compared with commercial-off-the-shelf mixers and state-of-the-art mixers in literature, as summarized in Table 3-1. It can be seen from Table 3-1 that the traveling-wave TVTL and the directly-pumped TVTL design achieve better noise figure and IIP3 compared with other mixer designs. The LO power consumption of current designs is in the higher end because the TVTL design has not been optimized for a high power-efficiency yet, and the MMIC processes used were low-cost GaAs HBT process that is not ideal for low-power applications. Ideally, parametric circuits enabled by nonlinear reactance can achieve 100% efficiency [47] if all harmonics and intermodulation tones are terminated properly. This implies that there is great potential in improving the power efficiency

and reducing the power consumption of a TVTL. As the proposed TVTL specifically emphasizes other features such as low noise and high linearity, it is difficult to apply a comprehensive figure of merit for comparison to other designs that are mainly targeted at low-power applications. It should also be noted that linearity specs reported in Table 3-1 from many existing works were obtained with linearization techniques, while no linearization or IM3 cancellation technique has been applied for the MMIC TVTL.

Table 3-1 Comparison table – TVTL vs state-of-the-art mixers

	MA3-242LH+*	LT-5520**	[27]	[57]	[58]	[59]	This work[a]	This work[b]	This work[c]
Technology	E-PHEMT	NR	PCB	0.18um CMOS	0.13um CMOS	0.13um CMOS	GaAs HBT	GaAs HBT	GaAs HBT
RF Center Frequency (MHz)	985	1800	1900	1925	2280	3250	800	1015	850
RF Bandwidth (MHz)	270	1000	NR	750	2830	4500	600	70	500
IF Bandwidth (MHz)	30	140	20*	NR	NR	NR	600	70	500
CG (dB)	-5.5	-1.0	10.0	22.5 to 25.0	13.5 to 14.0	17.5	-2.0 to 2.0	0.4	2.0 to 4.0
NF (dB)	NR	15.0	3.3	7.7 to 9.5	2.7 to 6.5	3.9	2.7	7.0	3.0
IIP3 (dBm)	18.0	15.9	16.0	7.0 to 10.5	-13.5 to -10.0	0.84	23.6	6.0	22.5
DC Power (mW)	110	270.0 to 315.0	0.0	10.0	16.8	34.5	0.0	0.0	0.0
LO Power (dBm)	0	-10 to 0	27	NR	NR	NR	27.5	19.9	31.1

* Mini-Circuits, MA3-242LH+ ** Analog Device, LT5520 [a] MMIC traveling-wave TVTL

[b] MMIC reflective TVTL [c] MMIC directly-pumped TVTL NR - not reported

Chapter 4

RF correlator with Time-Varying Transmission Lines (TVTL)

In Chapter 3, we proposed three different configurations of MMIC TVTLs and characterized their parametric mixing and amplification performance. Here in the chapter, the RF correlator concept enabled by the MMIC time-varying transmission lines (TVTL) is presented in Section 4.1. In general, an RF correlator can be realized by either the frequency translational approach or the feedback approach. In Section 4.2, two prototypes of RF correlators with the frequency translational approach were designed and fabricated to demonstrate and prove the concept. In Section 4.3, the feedback approach called the tunable peak amplifier, which utilizes the frequency cross-coupling property of a TVTL, is discussed. Measurement results of the prototype showed that the tunable peak amplifier could achieve sharp gain, low noise, and good linearity while offering a 10% frequency tuning range at around 1 GHz. In this chapter, the circuit designs and results reported in [49] and [60] are included.

4.1 Concept of RF correlator

Traditionally, commercial wireless communication systems rely on wireless standards to perform spectrum planning and avoid in-band interference. The correlation operation is normally done in the digital domain for simple implementations and to obtain processing gain in conventional spread spectrum systems. However, with the increased spectrum usage and growing needs of various wireless technologies, the in-band interference and coexistence of multiple radios in portal devices have become critical problems. Moreover, for military radio systems which function in unplanned and uncontrolled EM environments, in-band jamming is a severe issue that

can desensitize the RF front-ends, reduce the signal-to-interference ratio (SIR), and in the worst case, cause receiver failures.

A potential approach to mitigate the in-band interference issue is to employ signal processing blocks such as the correlator in the RF domain to interrogate the receiving signal at the first stage. The RF correlators are devices that perform the correlation operation and can serve as a spread spectrum encoder/decoder. Mathematically, a correlation operation consists of a multiplication operation followed by an integration operation, as shown in Figure 4-1. This can be realized in circuits by placing a mixer in front of a sharp bandpass filter or a feedback loop. The mixer performs the multiplication operation while the bandpass filter or the feedback loop servers as the integrator.

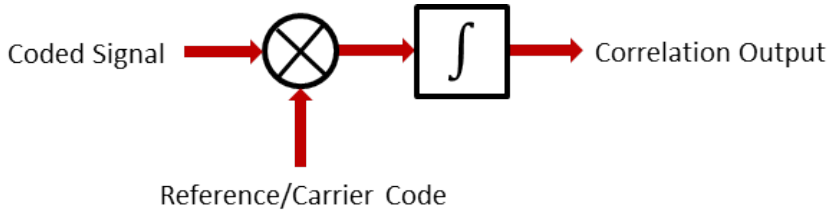

Figure 4-1. Diagram of the correlation operation.

From the signal and system point of view, when a received signal consisting of the desired wideband coded waveform, the narrowband jammer, and the noise arrives at the RF correlator, the received waveform is first mixed with the local oscillator that has the same pseudorandom code as the desired signal in the mixer. Since the desired signal is correlated with the reference code in the LO, the desired coded waveform is convolved into a narrow band signal with correlation/processing gain. The narrowband jammer, however, becomes a noise-like waveform because it is uncorrelated and is spread out by the reference code. Then the sharp bandpass filter or the feedback loop is employed to select the desired narrowband spectrum and maximize the

signal-to-noise ratio (SNR) of the received signal. The process of RF correlation is illustrated in Figure 4-2.

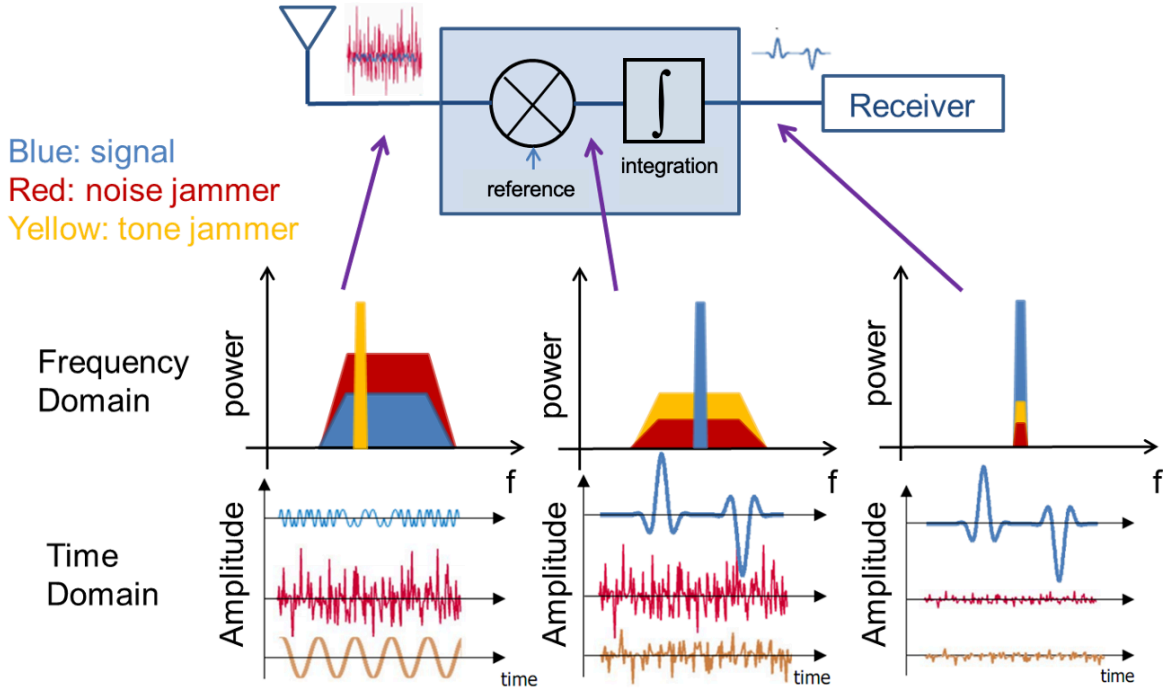

Figure 4-2 Principle of operation of the RF correlator.

Noted that for the benefit of the full system, the RF correlator must be placed at the very first stage of an RF front-end to prevent the jammers from hitting the low noise amplifier (LNA) in the receiver. Therefore, low-noise, low-loss, and high linearity are essential for the operation of the RF correlator. In this work, we proposed to utilize the TVTL as a capacitive mixer to perform the multiplication function because TVTLs can provide a moderate amount of conversion gain while being low-noise and linear. Both the sharp bandpass filter and the feedback loop were employed to perform the integration process, which lead to the frequency translational approach and the tunable peak amplifier approach of achieving RF correlation.

4.2 Frequency translational approach

In the frequency translational approach, a sharp bandpass filter was applied to perform the integration operation in the RF correlator.

4.2.1 Prototype with the traveling-wave TVTL

Different prototypes of the RF correlator with the frequency translational approach were designed and fabricated. Here in the section, the selected results of two prototypes are presented. The first prototype was based on the traveling-wave MMIC TVTL discussed in Section 3.1.2. The intended input frequency for the RF correlator was from 750 MHz to 1.1 GHz with the pump frequency ranging from 3.1 GHz to 3.45 GHz. Figure 4-3 and Figure 4-4 show the schematic and the photo of the designed RF correlator, where both triplexers at the input and output were implemented on-chip. The photo of the MMIC triplexer and its performance can be found in Figure 4-5. The RX band of the TriQuint TQQ1030 BAW duplexer was selected as the correlation filter as it has a narrow bandwidth and low insertion loss. The center frequency of the filter is 2.355 GHz with a 3 dB bandwidth of 10 MHz.

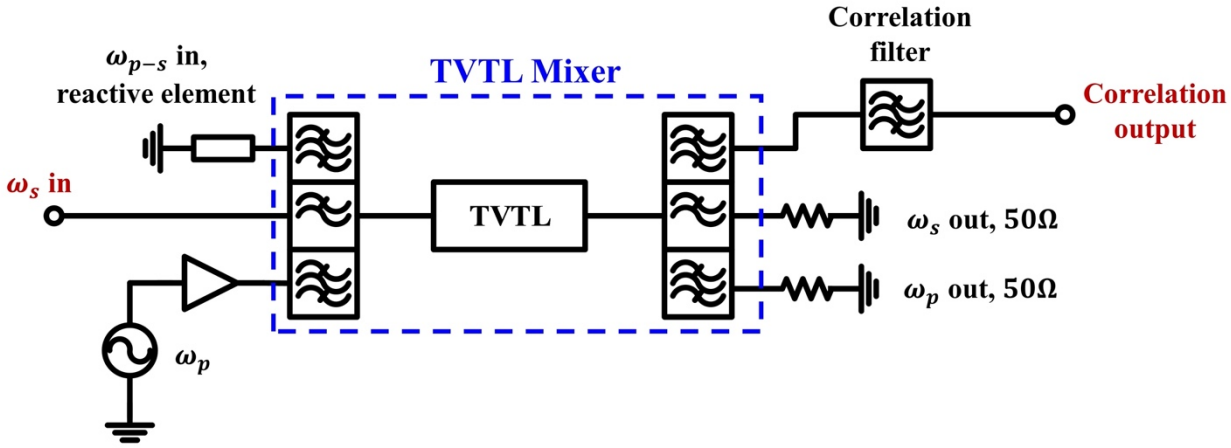

Figure 4-3 Circuit diagram of the RF correlator with the MMIC traveling-wave TVTL.

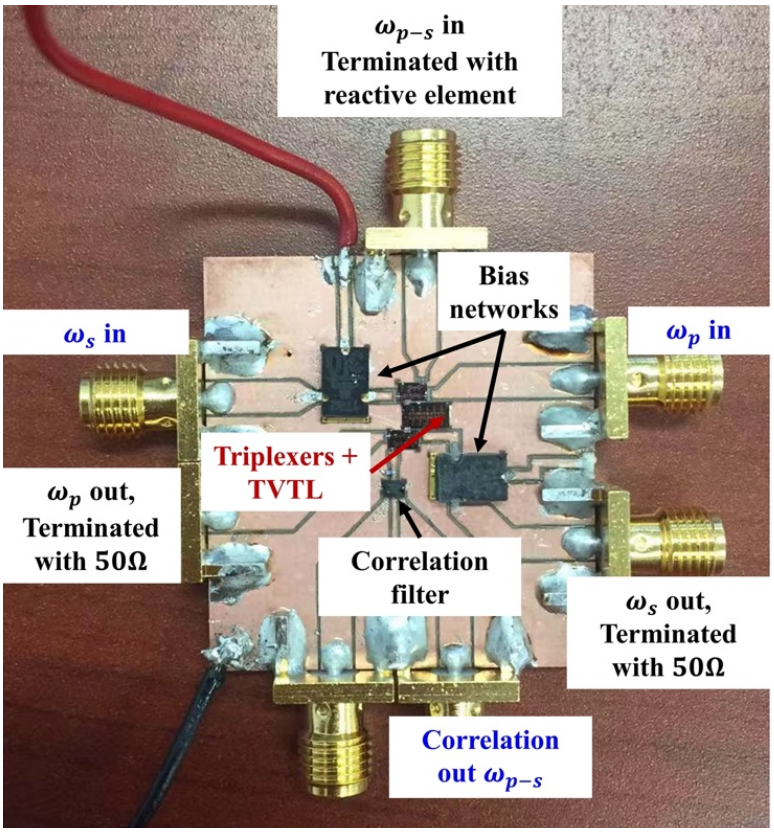

Figure 4-4. Photo of the fabricated prototype.

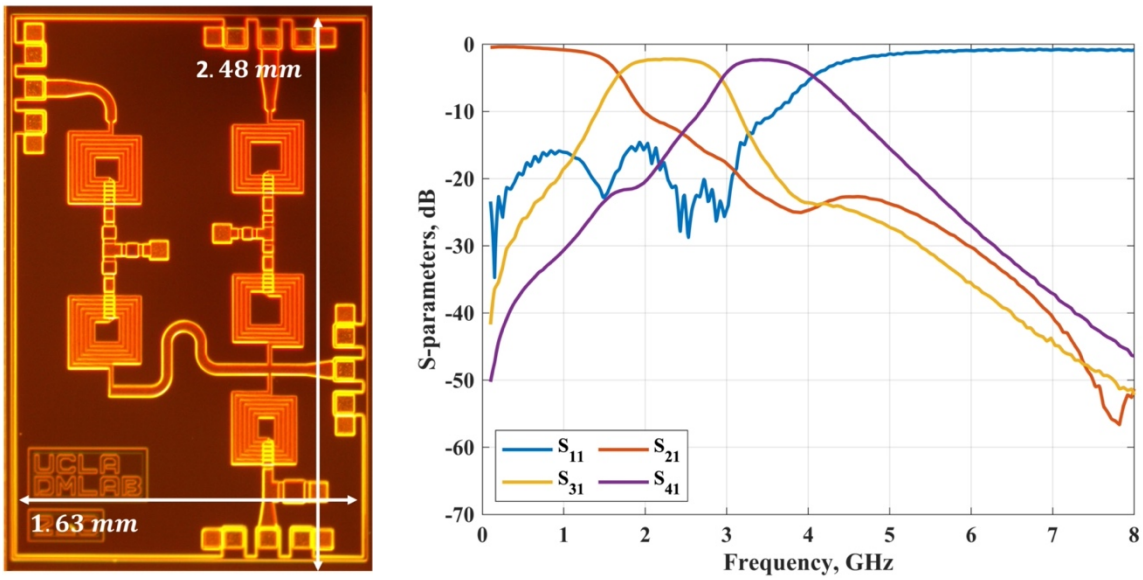

Figure 4-5. (a) Photo of the triplexer die; (b) Measured S-parameters of the triplexer.

The conversion gain of the RF correlator was firstly characterized with the Keysight N5241A PNA-X built-in mixer function. The frequency translational behavior of the RF correlator is shown in Figure 4-6. When the TVTL is placed in front of the fixed bandpass filter while altering the LO frequency, it corresponds to select the signal band at $\omega_{LO} - \omega_{BPF}$. In the measurement, the varactor diodes were biased at -4.5 V with a pump power of 27.5 dBm. The LO frequency changed from 3.10 GHz to 3.40 GHz with a 50 MHz step, which corresponds to selecting the correlation signal band from 750 MHz to 1.1 GHz. The minimum insertion loss of the RF correlator including the triplexers and the correlation filter is 4.6 dB at 800 MHz. Furthermore, the RF correlator prototype realized a frequency tuning range that was $>$ 300 MHz.

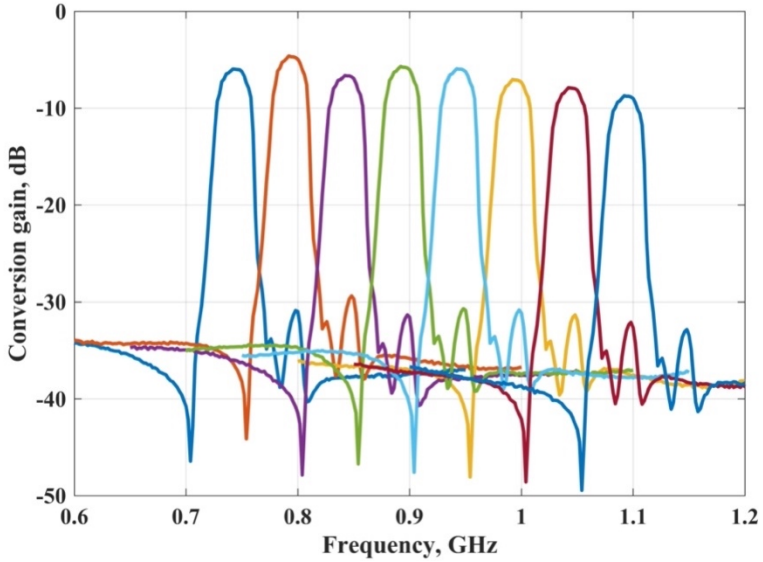

Figure 4-6 Measured conversion gain of the RF correlator sweeping pump frequency from 3.10 GHz to 3.40 GHz with a 50 MHz step. Lines from the left to the right correspond to the pump frequency shifting from 3.10 GHz to 3.40 GHz with a step of 50 MHz.

The noise figure of the RF correlator was measured with the built-in converter noise figure function of the Keysight N5241A PNA-X, as shown by the blue line in Figure 4-7. In the measurement, the varactor diodes were biased at -4.5 V with a pump power of 27.5 dBm at 3.40 GHz. The conversion loss of the RF correlator is also plotted in the same chart as a reference. It can be observed that the difference between the noise figure and the conversion loss of the RF correlator was < 1 dB, indicating that the MMIC TVTL chip did not introduce a significant amount of noise and most of the noise degradation comes from the resistive loss in the device.

The input P1dB of the designed correlator was measured at 1.0 GHz with varactor diodes biased at -4.5 V and a pump power of 27.5 dBm. From Figure 4-8, the input P1dB of the designed RF correlator was 16 dBm.

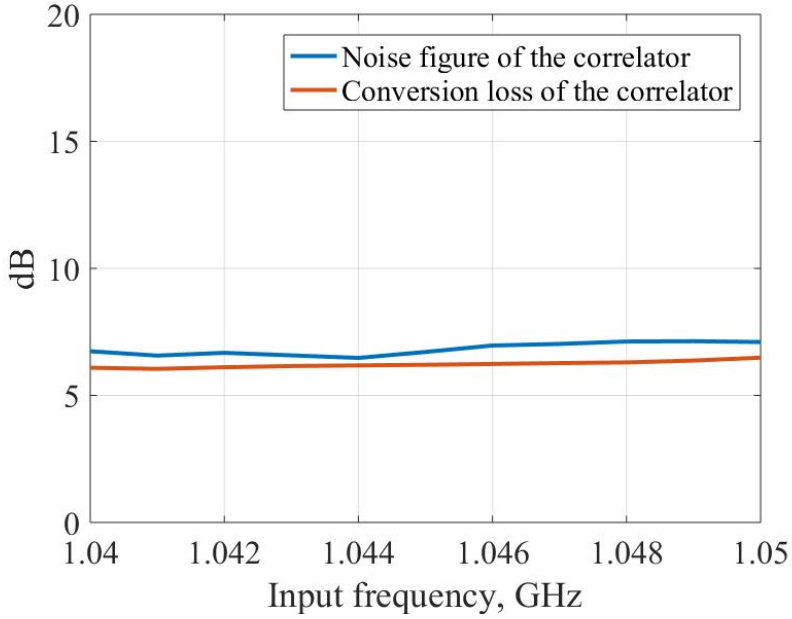

Figure 4-7 Measured noise figure of the RF correlator prototype.

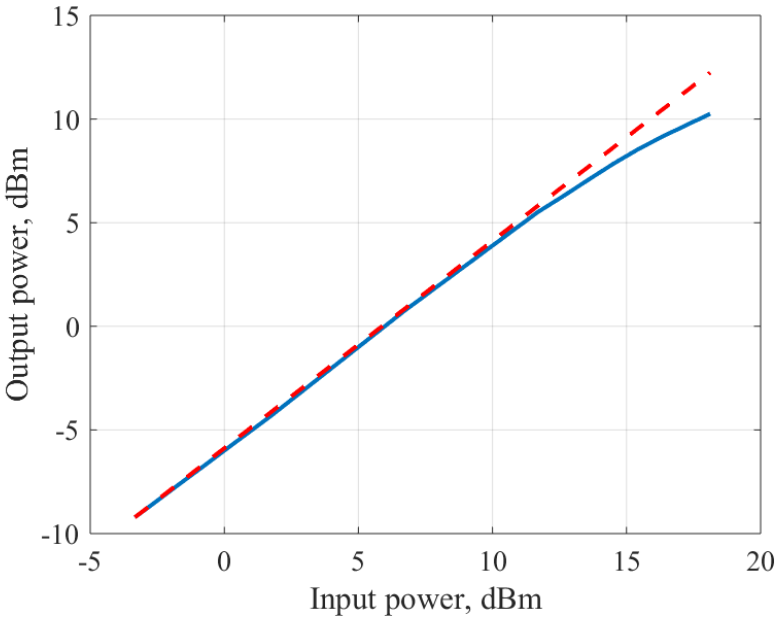

Figure 4-8 Measured P1dB of the RF correlator.

4.2.2 Prototype with the directly-pumped TVTL

To improve the noise performance of the RF correlator, the MMIC directly-pumped TVTL discussed in Section 3.3.2 was utilized to design the second prototype of the RF correlator. In this design, a customized triplexer fabricated with the Low Temperature Co-fired Ceramics (LTCC) substrate is also applied to minimize insertion loss. The RX band of the TriQuint TQQ1030 BAW duplexer was also used as the correlation filter in this prototype. Figure 4-9 and Figure 4-10 illustrate the schematic and the photo of the designed RF correlator.

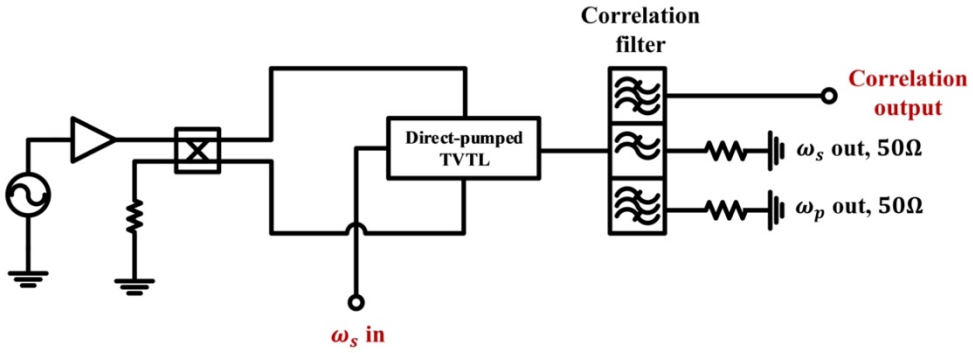

Figure 4-9 Schematic of the RF domain correlator based on the MMIC directly-pumped TVTL.

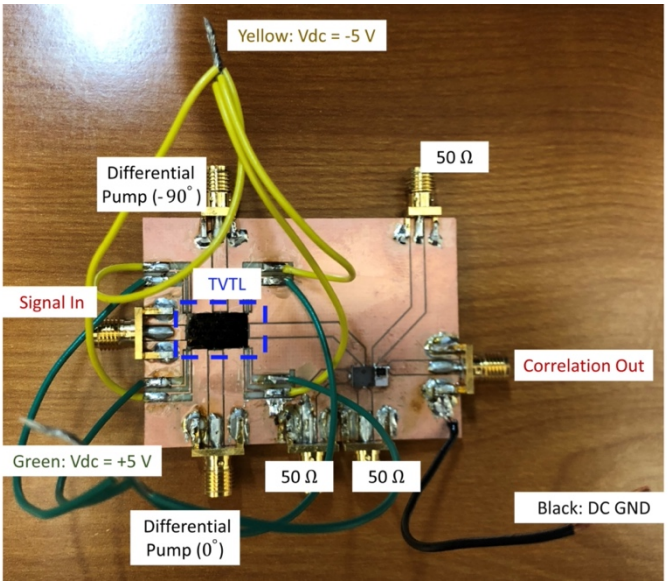

Figure 4-10 Photo of the fabricated RF correlator with the directly-pumped TVTL.

For this prototype, we also characterized the conversion gain and the noise figure with the Keysight N5241A PNA-X. In the conversion gain measurement of the designed correlator, the coded input signal is from 0.7 GHz to 1.0 GHz with an input power of -10 dBm. The reference LO is at 3.2 GHz with a power of 31.1 dBm. As shown in Figure 4-11, the minimum conversion loss of the RF correlator prototype including the triplexer is 0 dB. The insertion loss of the triplexer and the BAW correlation filter is also plotted in Figure 4-11 using the red dashed line as a reference. The in-band noise figure of the prototype was measured with the same LO power and frequency. The coded signal frequency in this experiment was from 842.5 MHz to 847.5 MHz. As shown in Figure 4-12, an average of 3.8 dB is achieved. Compared with the RF correlator prototype with the MMIC traveling-wave TVTL, the noise figure of this prototype was improved by around 2 dB.

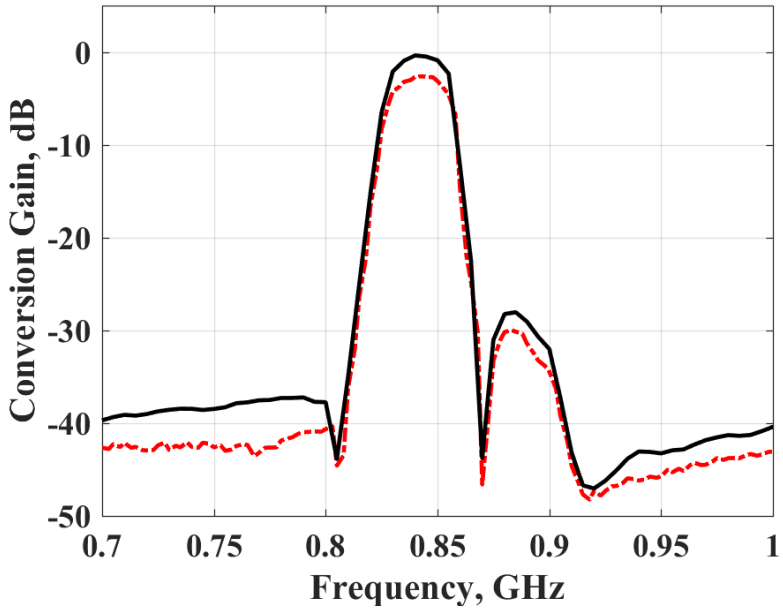

Figure 4-11 Measured conversion gain of RF correlator prototype with varactor diode bridges biased at ± 5.0 V.

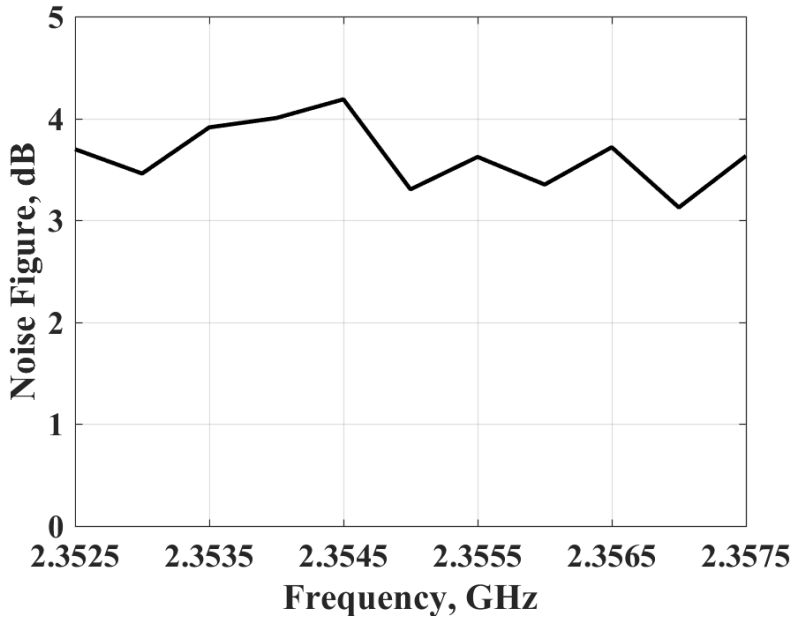

Figure 4-12 Measured noise figure of the RF correlator prototype with varactor diode bridges biased at ± 5.0 V.

The correlation test was carried out with the directly-pumped TVTL correlator prototype. The diagram of the test setup is shown in Figure 4-13. The two channels of the Arbitrary waveform generator (AWG) first generated two modulated signals with assigned codes. One of the modulated signals was then used as the received signal, while the other one was mixed with the LO and amplified to the right power level as the reference input. Both signal and reference waveforms were fed into the RF correlator, and the output waveform from the RF correlator was observed with the spectrum analyzer. In the correlation test, Binary Phase Shift Keying (BPSK) modulation was used for both the signal and the reference LO. Repeated binary codes were mapped into BPSK waveforms as shown in Figure 4-14, in which the phase of the reference LO was flipped by 180° at the end of each bit. The correlated signal code was identical to the reference LO code, whereas the orthogonal signal code was a continuous waveform without any phase change. The signal

waveform was centered at 845 MHz, and the reference LO waveform was centered at 3.2 GHz respectively. Both the signal and the reference LO code had a bit rate of 120 Mb/s without pulse shaping.

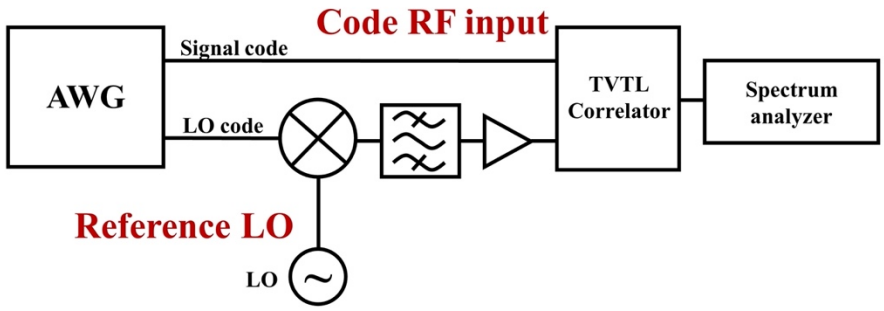

Figure 4-13 Correlation test and decoder test setup.

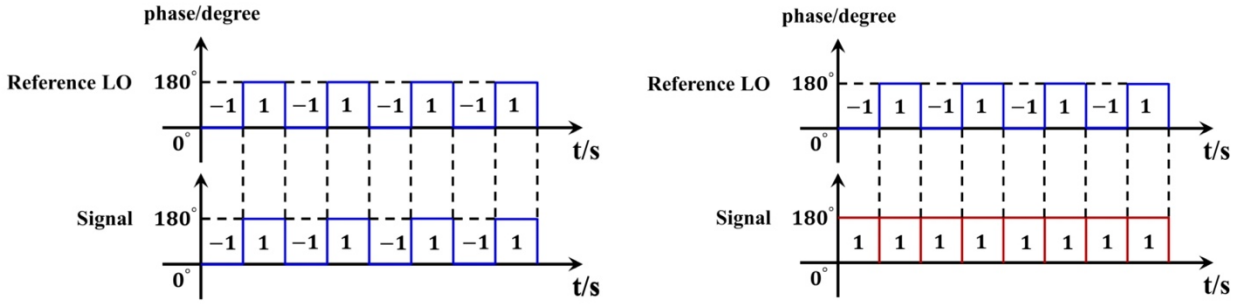

(a) (b)

Figure 4-14 (a) Correlated reference LO and signal codes for the correlation test. (b) Orthogonal reference LO and signal codes for the correlation test.

Figure 4-15 depicts the correlated and the orthogonal output spectra of the RF correlator. When the codes of the signal and reference LO were coherent, a peak at 2355 MHz could be observed, as shown in Figure 4-15. (a). On the contrary, when signal and reference codes were orthogonal to each other, a spectrum notch was observed. Comparing the spectra of the two cases,

$>$ 25 dB correlation suppression is obtained. Note that a minor spectrum regrowth was also observed in the output spectra of the RF correlator which was mainly caused by the misalignment in bits.

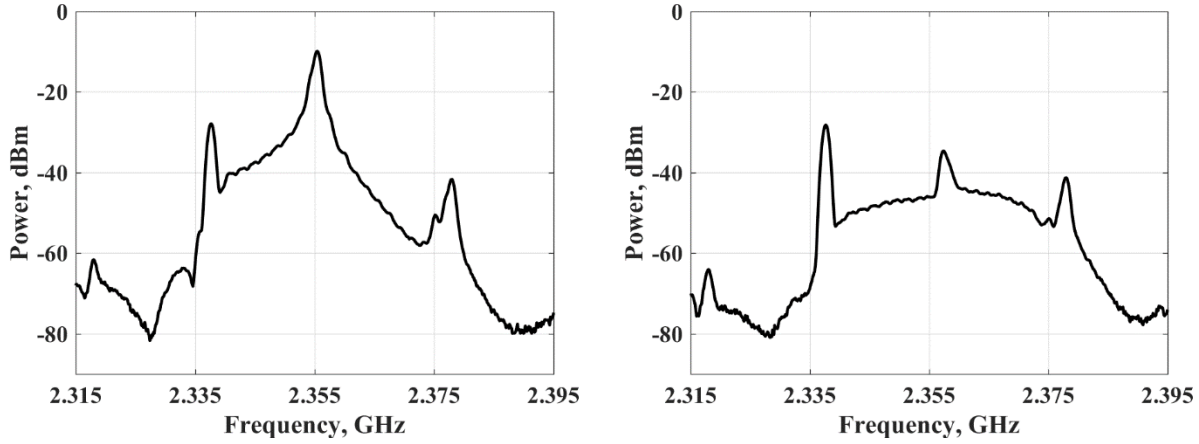

(a) (b)

Figure 4-15 (a) Output spectrum of the RF correlator when the signal code is identical to the reference code. (b) Output spectrum of the RF correlator when the signal code is orthogonal to the reference code.

4.3 Tunable peak amplifier approach

The second approach of achieving integration is via a feedback loop. In Section 2.1, we showed that a TVTL can be modeled as a four-port linear network defined by crossed-coupled frequency ω_s and ω_{p-s}. The unique frequency cross-coupling behavior of the TVTLs enables the possibility of adding feedback and resonance at one frequency and coupling that resonance to the other frequency to achieve frequency-selectivity. The concept was initially proposed in an earlier work [61] in which the authors analyzed the gain performance of the tunable peak amplifier and

demonstrated preliminary results of sharp gain behavior with a PCB TVTL. In this section, the operating principle of the tunable peak amplifier is first re-captured. Then, a detailed noise analysis of the tunable peak amplifier will be presented. Lastly, a prototype with the MMIC directly-pumped TVTL and its measurement results are discussed.

4.3.1 Operating principle of the tunable peak amplifier and its gain performance

The parametric gain behavior of the tunable peak amplifier can be mathematically explained as follows. Model the TVTL with a linear four-port network as depicted in Figure 2-1. Then the TVTL can be described by a matrix equation as follows:

$$\begin{bmatrix} V_s^-(z) \\ V_{p-s}^{*-}(z) \end{bmatrix} = \begin{bmatrix} t_{s,s} & t_{s,p-s} \\ t_{p-s,s} & t_{p-s,p-s} \end{bmatrix} \begin{bmatrix} V_s^+(0) \\ V_{p-s}^{*+}(0) \end{bmatrix} \tag{4-1}$$

where the "+" sign represents the incident voltages and the "−" sign represents the outgoing voltages. $(\cdot)^*$ denotes the operation of the complex conjugate. t_{ii}'s are the voltage gain of the TVTL at ω_i when $V_k^+(0) = 0, k \neq i$, and t_{ij}'s are the voltage conversion gain of the TVTL from ω_j to ω_i when $V_k^+(0) = 0, k \neq i$ where $i, j, k \in \{s, p-s\}$. Their formula can be found in equations (2-31)-(2-34).

If the output at ω_{p-s} is coupled back to the input port and assume the feedback has a delay of ϕ, as illustrated in Figure 4-16, where $V_{p-s}^{*+}(0) = V_{p-s}^{*-}(z)e^{j\phi}$, then equation (4-1) can be re-written into

$$V_s^-(z) = (t_{s,s} + \frac{t_{s,p-s}t_{p-s,s}e^{j\phi}}{1 - t_{p-s,p-s}e^{j\phi}})V_s^+(0) = A_{s,s}V_s^+(0). \tag{4-2}$$

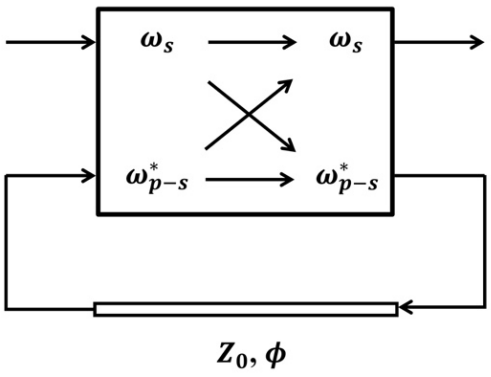

Figure 4-16 Diagram of the closed-loop TVTL with feedback at ω_{p-s}.

Substituting equations (2-31)-(2-34) into (4-2), then the voltage gain $A_{s,s}$ at the signal frequency ω_s can be written as

$$A_{s,s} = e^{-(\alpha_s z + j\beta_s z)}\left[\cosh(\lambda z) + \frac{\sinh^2(\lambda z)\, e^{-(\alpha_{p-s} z - j\beta_{m-s} z - j\phi)}}{1 - \cosh(\lambda z)\, e^{-(\alpha_{p-s} z - j\beta_{m-s} z - j\phi)}}\right]. \tag{4-3}$$

where $\lambda = \xi_0\sqrt{\beta_s \beta_{p-s}}/4$ is the eigenvalue of equation (2-12), and $\left|t_{p-s,p-s}\right| = \cosh(\lambda z)\, e^{-\alpha_{p-s} z}$ is assumed to be less than 1 to satisfy the stability requirement. By designing the delay of the feedback such that

$$\beta_{p-s} z + \phi = 2n\pi, \tag{4-4}$$

where z is the length of the TVTL and $n = 0, 1, 2, \cdots$, is an arbitrary non-negative number, a resonance at the converted frequency ω_{p-s} can be formed, which allows the energy at the converted band ω_{p-s} to build up. This is energy can then couple back to the signal frequency at ω_s and create an enhanced amplification at ω_s as the converted tone $V_{p-s}(z)$ circles through the TVTL multiple times. Moreover, equation (4-3) indicates that with the increase of the pump power,

i.e., modulation index ξ_0, $\left|t_{p-s,p-s}\right|$ will gradually approach 1. This will lead to a significantly enhanced Q of the resonance, and high gain and frequency-selectivity can be achieved at ω_s. Moreover, this also implies that the gain level and the sharpness of the amplification can also be altered through the control of the pump power. Thirdly, the frequency of the peak amplification is also tunable by varying the pump frequency. When changing the pump frequency from ω_{p1} to ω_{p2}, the signal frequency coupled with the fixed physical resonance at ω_{p-s} changes from $\left(\omega_{p1}-\omega_{p-s}\right)$ to $\left(\omega_{p2}-\omega_{p-s}\right)$. Note that this frequency tuning operation does not involve changing the physical resonance at ω_{p-s}, so a wide frequency tuning range may be achieved. Last but not least, the tunable peak amplifier can operate in both phase asynchronous mode and phase synchronous mode to the waveform to be filtered. The first operation mode is similar to a conventional tunable peak amplifier that provides high frequency-selectivity, while the phase synchronous mode is equivalent to performing RF correlation.

4.3.2 Thermal noise analysis of the tunable peak amplifier

In the following context, we refer to the TVTL without the feedback loop as the open-loop TVTL. Theoretically, an open-loop TVTL exhibits the low-noise characteristic which is favorable especially for receiver applications. The tunable peak amplifier enabled by the closed-loop TVTL possesses superior frequency-selectivity and tunability by coupling the resonance at the converted band ω_{p-s} to the signal frequency ω_s. Since resonance and feedback involve, which may add a significant amount of noise to the output of the tunable peak amplifier, the noise behavior of the peak amplifier must be carefully analyzed. Figure 4-17 illustrates the diagrams for the thermal noise analysis, in which two resonators are to conceptually separate the two frequencies of interest, and they are assumed to be lossless in the following analysis. The resistive loss of the TVTL adds

thermal noise at both the signal frequency ω_s and the converted frequency ω_{p-s}. The input referred noise power are given by equations (2-41) and (2-42).

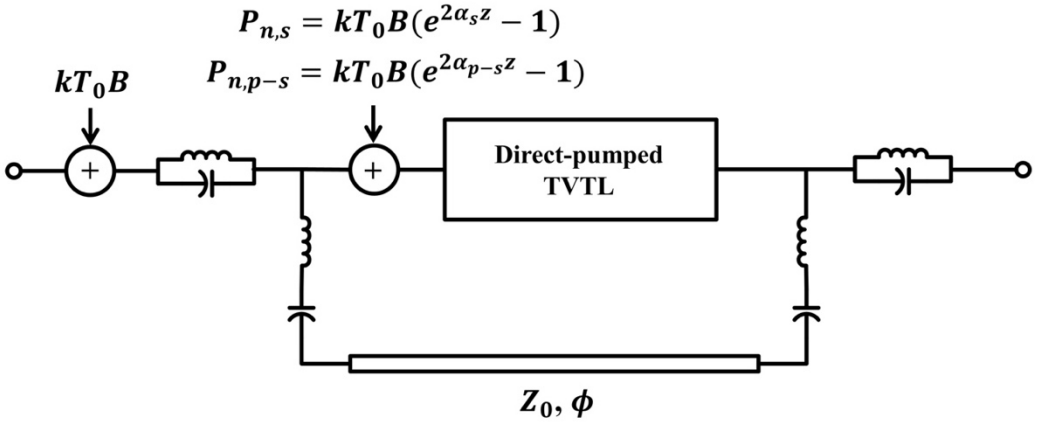

Figure 4-17 Equivalent noise diagram of the tunable peak amplifier.

Let us first consider the thermal noise originated at the signal frequency ω_s. Denote the noise voltage generated at ω_s by the m-th unit cell as $v_{ni,s}^{(m)}$. From the noise analysis of the open-loop TVTL in equations (2-45) and (2-51), the noise voltage emitted by the m-th unit cell leads to two open-loop noise components, that are

$$\omega_s \longrightarrow \omega_s: v_{no1,s,0}^{(m)} = \left\{1 + \left(\frac{M-m+1}{M}\right)[\cosh(\lambda z) - 1]\right\} v_{ni,s}^{(m)} e^{-\alpha_s z}. \tag{4-5}$$

$$\omega_s \longrightarrow \omega_{p-s}: v_{no1,p-s,0}^{(m)} = j e^{j\phi_p} \sqrt{\frac{\beta_{p-s}}{\beta_s}} \sinh(\lambda z) \left(\frac{M-m+1}{M}\right) v_{ni,s}^{(m)} e^{-\alpha_{p-s} z}. \tag{4-6}$$

where the last subscript in $v_{no1,s,0}^{(m)}$ and $v_{no1,p-s,0}^{(m)}$ represents the noise voltage without traveling in the loop. Since the feedback is introduced at the output ω_{p-s} port of the TVTL in the tunable peak amplifier, the noise voltage $v_{no1,p-s,0}^{(m)}$ will travel back to the input ω_{p-s} port of TVTL. The energy

of $v_{no1,p-s,0}^{(m)}$ can then be coupled back to the signal frequency ω_s as it travels along the TVTL multiple times. In the first round of traveling in the loop, the noise voltage $v_{no1,p-s,0}^{(m)}$ is either converted back to the signal frequency ω_s with a voltage gain $t_{s,p-s}$ or "amplified" by the TVTL with a voltage gain $t_{p-s,p-s}$. The resulted noise voltages are as follows.

$$v_{no1,s,1}^{(j)} = t_{s,p-s}\left(v_{no1,p-s}^{(m)} e^{-j\phi}\right)^*. \tag{4-7}$$

$$v_{no1,p-s,1}^{(j)} = t_{p-s,p-s}\left(v_{no1,p-s}^{(m)} e^{-j\phi}\right). \tag{4-8}$$

where the last subscript in $v_{no1,s,1}^{(j)}$ and $v_{no1,p-s,1}^{(j)}$ refers to the first round of traveling in the loop, and ϕ is the delay of the feedback. $v_{no1,p-s,1}^{(j)}$ will again circle back to the input ω_{p-s} port of TVTL and repeat the looping process. During the k-th round in the loop, the noise voltages are

$$v_{no1,s,k}^{(j)} = t_{s,p-s}\left(v_{no1,p-s,k-1}^{(j)} e^{j\phi}\right)^* = t_{s,p-s} e^{j\phi}\left(t_{p-s,p-s} e^{j\phi}\right)^{k-1} v_{no1,p-s,0}^{(j)}. \tag{4-9}$$

$$v_{no1,p-s,k}^{(j)} = t_{p-s,p-s}\left(v_{no1,p-s,k-1}^{(j)} e^{-j\phi}\right) = \left(t_{p-s,p-s} e^{-j\phi}\right)^k v_{no1,p-s,0}^{(j)}. \tag{4-10}$$

Since the noise voltages $v_{no1,s,k}^{(m)}$'s are correlated, the noise power from the m-th unit cell should be computed by first summing $v_{no1,s,k}^{(j)}$'s, $k = 0,1,$ ..., to obtain the total output noise voltage $v_{no1,s}^{(m)}$ from the m-unit cell.

$$v_{no1,s}^{(m)} = \sum_{k=0}^{\infty} v_{no1,s,k}^{(m)}$$

$$= v_{no1,s,0}^{(m)} + \sum_{k=1}^{\infty} t_{s,p-s} e^{j\phi} \left(t_{p-s,p-s} e^{j\phi}\right)^{k-1} v_{no1,p-s,0}^{(m)}$$

$$= v_{no1,s,0}^{(m)} + \left(\frac{t_{s,p-s} e^{j\phi}}{1 - t_{p-s,p-s} e^{j\phi}}\right) v_{no1,p-s,0}^{(m)}. \quad (4\text{-}11)$$

Noted that to make the infinite summation in equation (4-11) converge, $\left|t_{p-s,p-s} e^{j\phi}\right|$ must be less than 1, i.e., $\left|t_{p-s,p-s}\right|$ is a voltage attenuation rather than a voltage amplification. This is the same condition for the stability requirement imposed by the voltage gain in equation (4-3). The total output noise power at ω_s from $v_{ni,s}^{(m)}$'s can then be derived summing the M noise power from each unit cell.

$$P_{no1,s} = \frac{\sum_{m=1}^{M} \left|v_{no1,s}^{(m)}\right|^2}{2Z_0}. \quad (4\text{-}12)$$

The output thermal noise resulted from the noise voltages $v_{ni,p-s}^{(m)}$ initially generated at the converted frequency ω_{p-s} can also be analyzed using the same procedure as that in equations (4-5)-(4-12). It must be noted that for the closed-loop case, the reverse currents at ω_{p-s} do not couple to the output of the TVTL. They only circle in the loop and finally get dissipated. Consequently, the open-loop noise voltages contributed by $v_{ni,p-s}^{(m)}$ in the tunable peak amplifier becomes

$$\omega_{p-s} \longrightarrow \omega_s: v_{no2,s,0}^{(m)} = (M-m+1) g_{s,p-s} Z_0 v_{ni,p-s}^{(m)} e^{-\alpha_s z}$$

$$= -j e^{j\phi_p} \sqrt{\frac{\beta_s}{\beta_{p-s}}} \sinh(\lambda z) \frac{(M-m+1)}{M} v_{ni,p-s}^{(m)} e^{-\alpha_s z}. \quad (4\text{-}13)$$

$$\omega_{p-s} \longrightarrow \omega_{p-s}: v_{no2,p-s,0}^{(m)} = \{1 + (M-m+1) g_{p-s,p-s} Z_0\} v_{n,p-s}^{(m)} e^{-\alpha_{p-s} z}$$

$$= \left\{1 + \left(\frac{M-m+1}{M}\right)[\cosh(\lambda z) - 1]\right\} v_{ni,p-s}^{(m)} e^{-\alpha_{p-s} z}. \quad (4\text{-}14)$$

The noise voltage $v_{no2,p-s,0}^{(m)}$ also experiences the same resonance behavior as that of $v_{no1,p-s,0}^{(m)}$. It circles through TVTL multiple times and contributes to the total output noise. Following the steps in equations (4-7)-(4-12), the total output noise voltage from the m-th unit cell and the total noise power at ω_s from all $v_{ni,p-s}^{(m)}$'s can be found by

$$v_{no2,s}^{(m)} = \sum_{k=0}^{\infty} v_{no2,s,k}^{(m)} = v_{no2,s,0}^{(m)} + \left(\frac{t_{s,p-s} e^{j\phi}}{1 - t_{p-s,p-s} e^{j\phi}}\right) v_{no2,p-s,0}^{(m)}. \quad (4\text{-}15)$$

$$P_{no2,s} = \frac{\sum_{m=1}^{M} \left| v_{no2,s}^{(m)} \right|^2}{2Z_0}. \quad (4\text{-}16)$$

Summing the output noise power in equations (4-12) and (4-16), the noise factor of the tunable peak amplifier with the closed-loop TVTL can be found by

$$F = \frac{S_i/N_i}{S_o/N_o} = \frac{S_i}{\left|A_{s,s}\right|^2 S_i} \cdot \frac{\left|A_{s,s}\right|^2 kT_0 B + P_{no1,s} + P_{no2,s}}{kT_0 B}. \quad (4\text{-}17)$$

where $A_{s,s}$ is the voltage gain at the signal frequency ω_s formulated by equation (4-3). Equation (4-17) is difficult to obtain an analytical solution, however, it can be much simplified near the physical resonance, i.e., near the peak gain frequency, where the phase condition in equation (4-4)

is satisfied and $\left|1 - t_{p-s,p-s}e^{j\phi}\right| = 1 - \left|t_{p-s,p-s}\right|$ approaches 0. Under these conditions, $\left|A_{s,s}\right|^2$ can be approximated by

$$\left|A_{s,s}\right|^2 = \left|t_{s,s} + \frac{t_{s,p-s}t_{p-s,s}e^{j\phi}}{1 - t_{p-s,p-s}e^{j\phi}}\right|^2 \approx \left|\frac{t_{s,p-s}t_{p-s,s}}{1 - \left|t_{p-s,p-s}\right|}\right|^2 \longrightarrow \infty. \tag{4-18}$$

$P_{no1,s}$ in equation (4-12) can be approximated by

$$\begin{aligned} P_{no1,s} &= \frac{\sum_{m=1}^{M}\left|v_{no1,s}^{(m)}\right|^2}{2Z_0} \\ &\approx \left|\frac{t_{s,p-s}}{1 - \left|t_{p-s,p-s}\right|}\right|^2 \frac{\sum_{m=1}^{M}\left|v_{no1,p-s,0}^{(m)}\right|^2}{2Z_0} \\ &= \frac{v_{ni,s}^2}{2Z_0}\left|\frac{t_{p-s,s}t_{s,p-s}}{1 - \left|t_{p-s,p-s}\right|}\right|^2 \sum_{m=1}^{M}\left(\frac{M-m+1}{M}\right)^2 \\ &= \frac{kT_0B(e^{2\alpha_s z} - 1)}{M}\left|\frac{t_{p-s,s}t_{s,p-s}}{1 - \left|t_{p-s,p-s}\right|}\right|^2 \frac{M(M+1)(2M+1)}{6M^2} \\ &\approx \frac{1}{3}kT_0B(e^{2\alpha_s z} - 1)\left|\frac{t_{p-s,s}t_{s,p-s}}{1 - \left|t_{p-s,p-s}\right|}\right|^2. \end{aligned} \tag{4-19}$$

and the summation in equation (4-16) can be approximated by

$$P_{no2,s} = \frac{\sum_{m=1}^{M}\left|v_{no2,s}^{(m)}\right|^2}{2Z_0}$$

$$\approx \left|\frac{t_{s,p-s}}{1-\left|t_{p-s,p-s}\right|}\right|^2 \frac{\sum_{m=1}^{M}\left|v_{no2,p-s,0}^{(m)}\right|^2}{2Z_0}$$

$$= \frac{v_{ni,p-s}^2}{2Z_0} e^{-2\alpha_{p-s}z}\left|\frac{t_{s,p-s}}{1-\left|t_{p-s,p-s}\right|}\right|^2 \sum_{m=1}^{M}\left\{1+\left(\frac{M-m+1}{M}\right)[\cosh(\lambda z)-1]\right\}^2$$

$$\approx \frac{kT_0B(e^{2\alpha_{p-s}z}-1)e^{-\alpha_{p-s}z}}{M}\left|\frac{t_{s,p-s}}{1-\left|t_{p-s,p-s}\right|}\right|^2 \sum_{m=1}^{M}\{M+(M+1)[\cosh(\lambda z)-1]\}$$

$$\approx kT_0B(e^{2\alpha_{p-s}z}-1)e^{-2\alpha_{p-s}z}\cosh(\lambda z)\left|\frac{t_{s,p-s}}{1-\left|t_{p-s,p-s}\right|}\right|^2. \quad (4\text{-}20)$$

With equations (4-18)-(4-20), the noise factor in equation (3-18) can be simplified into

$$F \approx 1+\frac{1}{3}(e^{2\alpha_s z}-1)+\frac{(e^{2\alpha_{p-s}z}-1)}{\cosh(\lambda z)}\left|\frac{t_{p-s,p-s}}{t_{p-s,s}}\right|^2 \quad (4\text{-}21)$$

Equation (4-21) indicates the tunable peak amplifier can exhibit an even lower noise factor near the physical resonance than the open-loop noise factor as denoted by equation (2-55).

4.3.3 Prototype of the tunable peak amplifier with the directly-pumped TVTL

A prototype of the tunable peak amplifier was designed and fabricated with the MMIC directly-pumped TVTL discussed in Section 3.3.2. The intended frequency for the tunable peak amplifier was around 1.1 GHz with a pump frequency near 3.2 GHz. The circuit diagram of the tunable peak amplifier is shown in Figure 4-18, where diplexers are implemented at the input and output of the directly-pumped TVTL to separate the two frequencies of interest. These diplexers consist of both the lumped element filters as well as the stepped-impedance filters. In this design,

Rogers Corporation RO4003C material was selected as the PCB substrate, and the lumped components used were from muRata Manufacturing. The differential pump signals to drive the TVTL were fed from the backside of the PCB with panel mount SMA connectors. Figure 4-19 shows the photo of the tunable peak amplifier prototype.

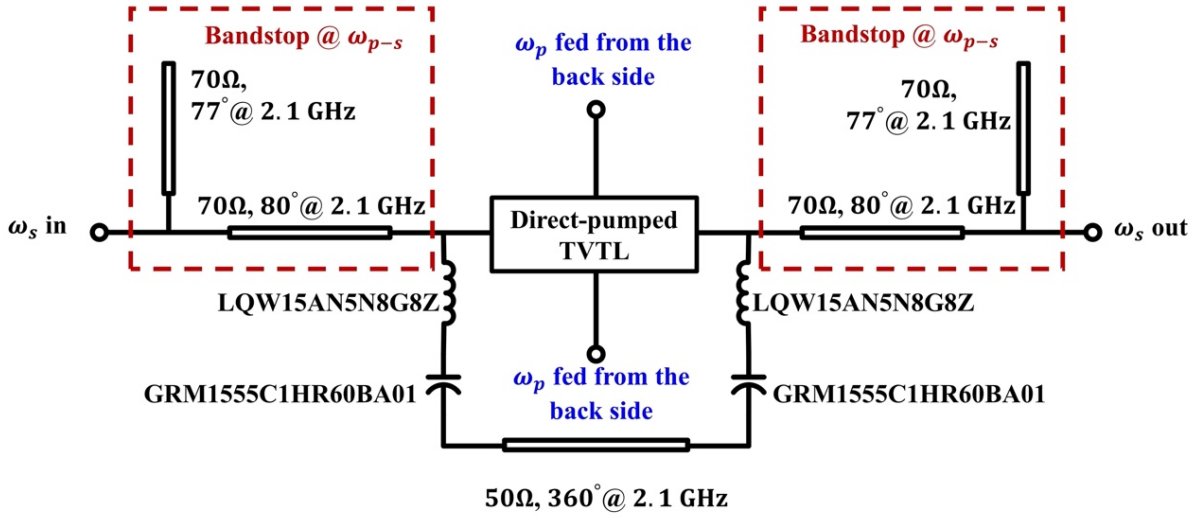

Figure 4-18 Circuit diagram of the tunable peak amplifier.

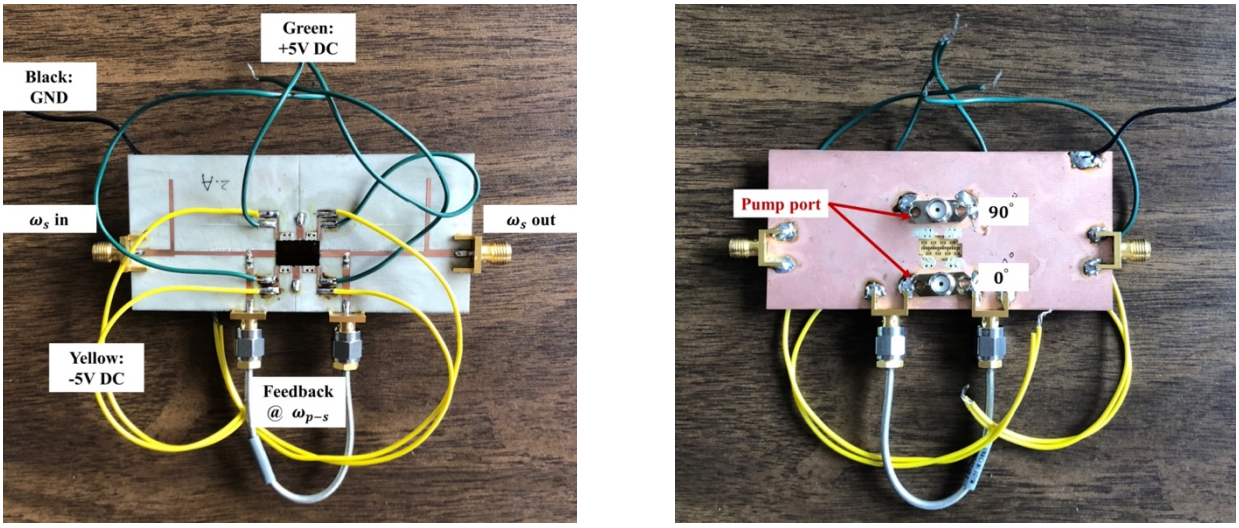

(a) (b)

Figure 4-19 Photos of the tunable peak amplifier prototype. (a) Front view of the tunable peak amplifier prototype. (b) Back view of the prototype where the removal of the PCB substrate around the directly-pumped TVTL chip is to prevent 3D inductor traces from touching the ground.

The tunable peak gain behavior of the designed amplifier was first characterized. Figure 4-21 demonstrates the theoretical, simulated, and measured insertion gains of the designed peak gain amplifier. The theoretical results were calculated based on equation (4-3). The simulations were carried out in the Advanced Design System (ADS) with Momentum EM models and the Harmonic Balanced (HB) simulation. The measurements were performed with the Keysight N5241A PNA-X. In both simulations and measurements, the directly-pumped TVTL was biased at ± 5 V to utilize the maximize the capacitance variation ratio of the varactor diodes. The input signal was from 1.0 GHz to 1.2 GHz with a power of -30 dBm. The pump was at 3.22 GHz with a power of 31 dBm. As shown in Figure 4-20, > 25 dB peak insertion gain was observed with a bandwidth

$<$ 5MHz. Furthermore, the measured insertion gain agrees with the theoretical analysis and simulation of the insertion gain fairly well.

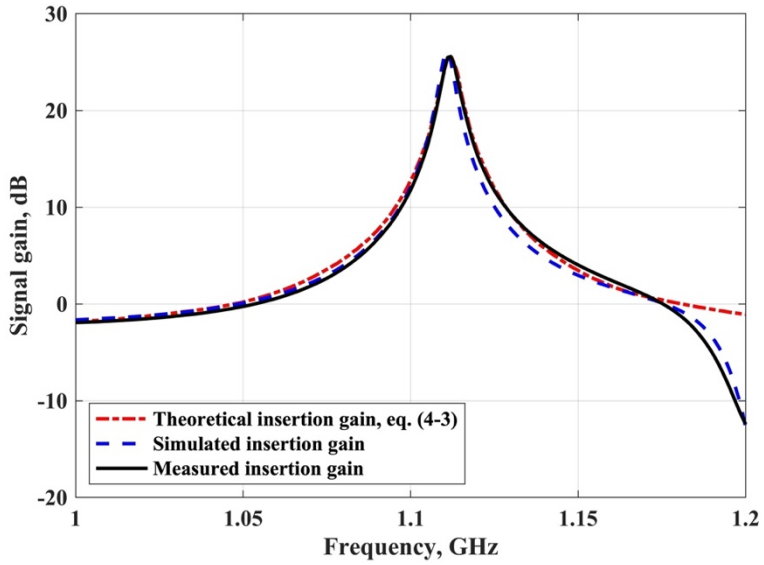

Figure 4-20 Insertion gain of the tunable peak amplifier with a 31 dBm pump at 3.22 GHz.

Then, we investigated the frequency tunability of the proposed tunable peak amplifier with both simulations and measurements. In these setups, the pump frequency was shifted from 3.12 GHz to 3.22 GHz with a step of 20 MHz. For each step of the pump frequency, the insertion gain of the tunable peak amplifier from 1.0 GHz to 1.2 GHz was captured. In the measurement, the pump was generated by an external signal generator with variable frequencies. It was then amplified to 31 dBm by a power amplifier and divided into two branches with a 90° phase difference. The simulated and measured insertion gains are depicted in Figure 4-21. It can be seen from Figure 4-21 that the center frequency of the amplifier varied according to the shift of the pump frequency. $>$ 100 MHz 3 dB frequency tuning range was achieved in the prototype.

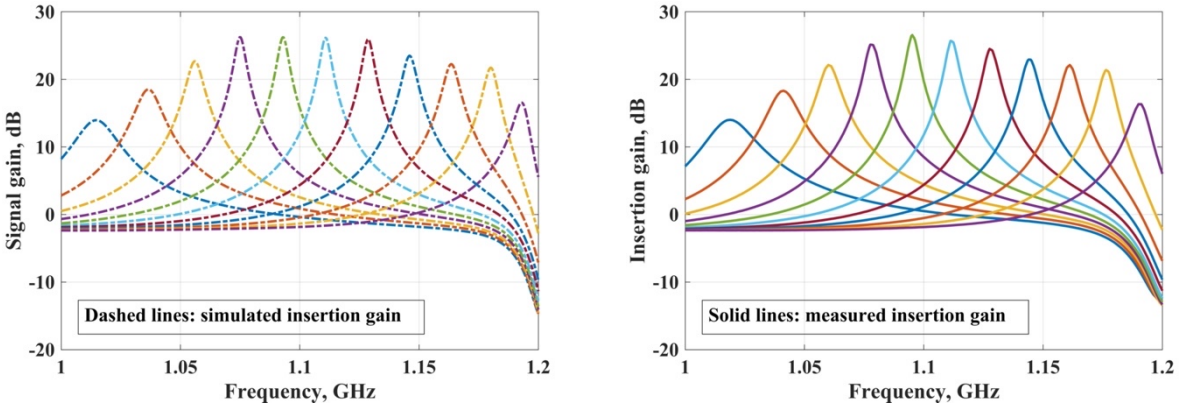

(a) Simulated (b) Measured

Figure 4-21 Insertion gains of the tunable peak gain amplifier sweeping the pump frequency from 3.12 GHz to 3.22 GHz. Lines from the left to the right correspond to the pump frequency shifting from 3.12 GHz to 3.22 GHz with a step of 20 MHz.

In addition to the frequency tunability, equation (4-3) also indicates that the gain of the peak amplifier is tunable with respect to the pump power. This effect was also validated in simulations and measurements with identical input and varactor diode biasing. The pump frequency was fixed at 3.22 GHz, and its power was altered from 26 dBm to 31 dBm. As shown in Figure 4-22, the peak gain increases with the increase of the pump power. This indicates that the gain levels of the peak amplifier can also be controlled through the pump. Note that there was a 10 MHz shift in the peak gain frequency when the pump power varied from 26 dBm to 31 dBm. This was due to the fact that the fast-varying pump waveform could affect the impedance and delay of the TVTL. At different pump levels, the TVTL exhibited slightly different phase delays, causing the frequency shift of the insertion gain.

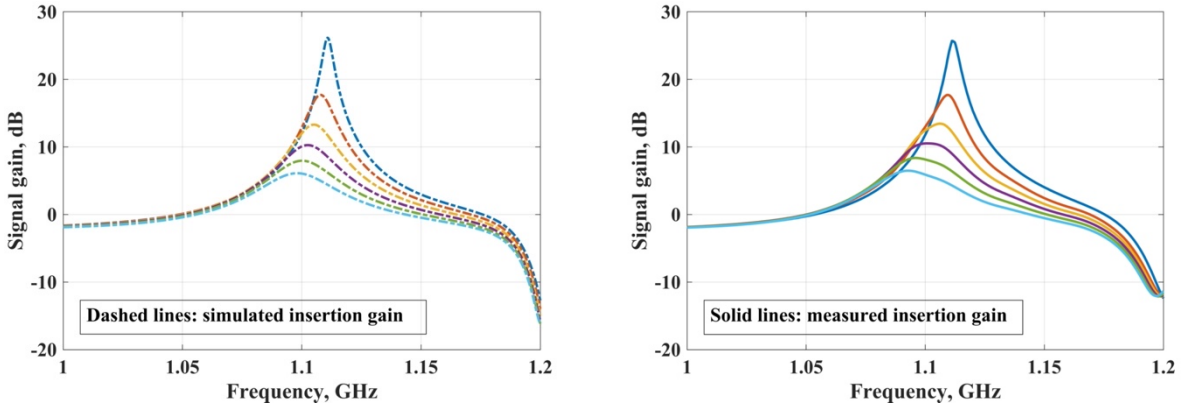

(a) Simulated (b) Measured

Figure 4-22 Insertion gains of the tunable peak gain amplifier sweeping the pump power from 26 dBm to 31 dBm. Lines from the top to the bottom correspond to the pump power varying from 26 dBm to 31 dBm with a 1 dBm step.

Thirdly, we characterized the noise performance of the tunable peak gain amplifier. Similarly, simulations and measurements were performed to confirm the low noise characteristic predicted by equation (4-21). For the simulations, we utilized the Harmonic Balanced (HB) nonlinear noise option to calculate the output noise voltages and then converted them into the total noise figure using [62, eq. 2-116]. For measurements, the built-in amplifier noise figure function of the Keysight N5241A PNA-X was used. In both the simulations and measurements, the varactor diodes were biased at ± 5 V, and the pump was at 3.22 GHz with a power of 31 dBm. Figure 4-23 depicts the simulated and measured noise figure of the tunable peak gain amplifier. They are also compared with the theoretical noise figure near the resonance, i.e., peak gain frequency, by equation (4-21). The measured insertion gain results are included as a reference. In Figure 4-23, <1.8 dB noise figure was observed in both the simulation and measurement of the tunable peak amplifier. This matches well with the theoretical approximation by equation (4-21). There were

two “bumps” observed in the measurements near the peak gain frequency. These could be due to the phase noise leakage from the pump. At the peak gain region where the insertion gain was high, the thermal noise dominated, and the effect of the phase noise did not play an important role in the overall noise figure. However, as the insertion gain decreased rapidly for out-of-band frequencies, the phase noise leaked from the pump port could no longer be neglected, causing the two noise figure peaks near the physical resonance. Furthermore, we also noticed in the measurement that when the insertion gain was high, the in-band noise figure decreased with the insertion gain (i.e., the pump power), as depicted in Figure 4-24.

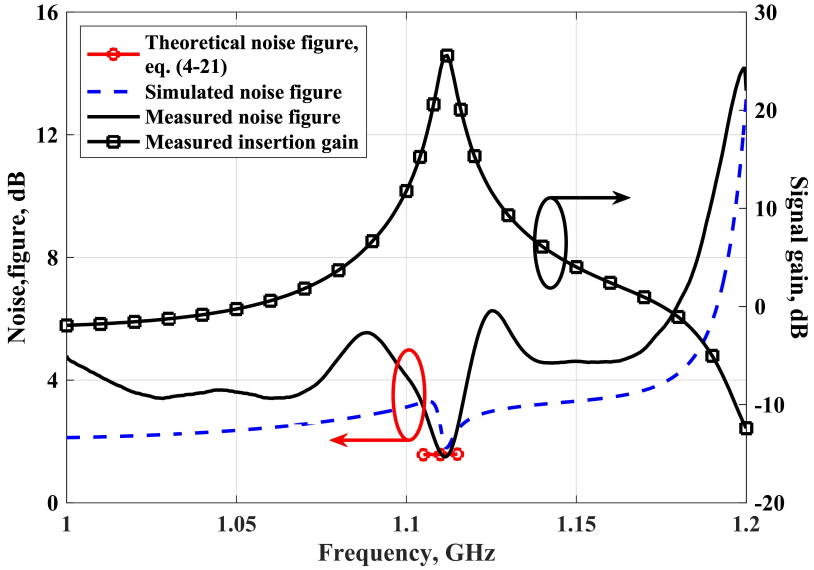

Figure 4-23 Noise figure of the tunable peak amplifier and its associated insertion gain.

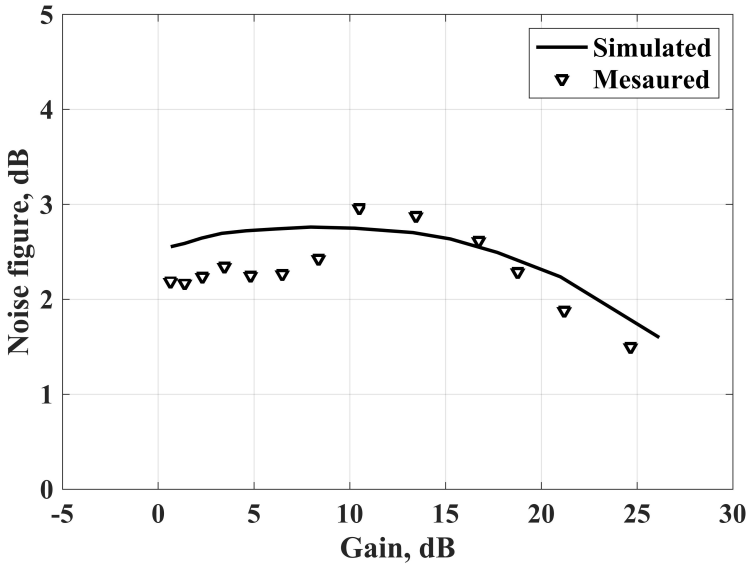

Figure 4-24 In-band noise figure variations with respect to the peak gain level.

Lastly, measurement results show that the tunable peak amplifier also has excellent linearity performance. In both the P1dB and IP3 measurements, the varactor diodes were biased at ± 5 V, and the pump was at 3.22 GHz with a 31 dBm power. Figure 4-25 shows that the measured in-band OP1dB of the tunable peak was 4.9 dBm.

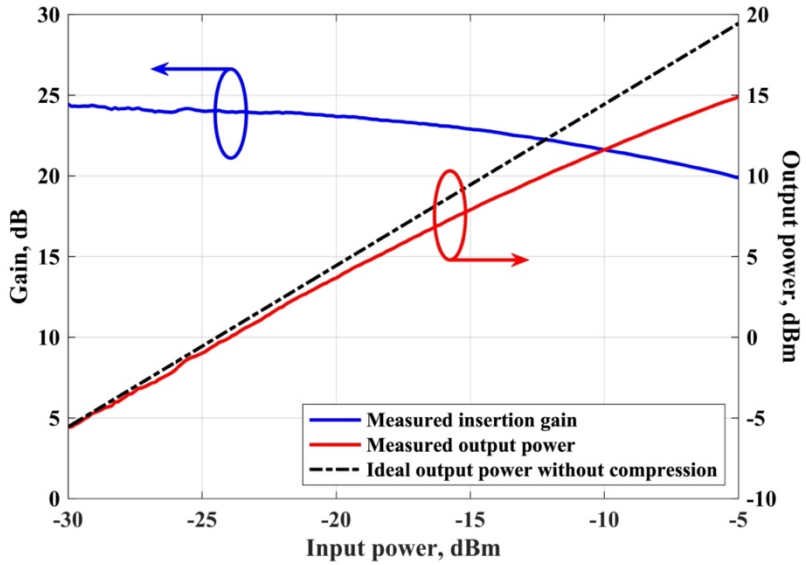

Figure 4-25 Measured in-band insertion gain and output power of the tunable peak with respect to the input power.

Figure 4-26 depicts the input IP3 of the tunable peak amplifier with respect to the frequency offset Δf from the peak gain frequency. Since the peak gain frequency was 1.11 GHz with the 3.22 GHz pump, the measured insertion gain was from 1.01 GHz to 1.21 GHz. As shown in Figure 4-26, the in-band IIP3 was -11.5 dBm, and the out-of-band IIP3 > 30 dBm at -90 MHz offset. This implies that the tunable peak amplifier can be inserted before the diplexer of a wireless front-end to boost the in-band received signal power without suffering from the degradation due to the adjacent channel blocker interference.

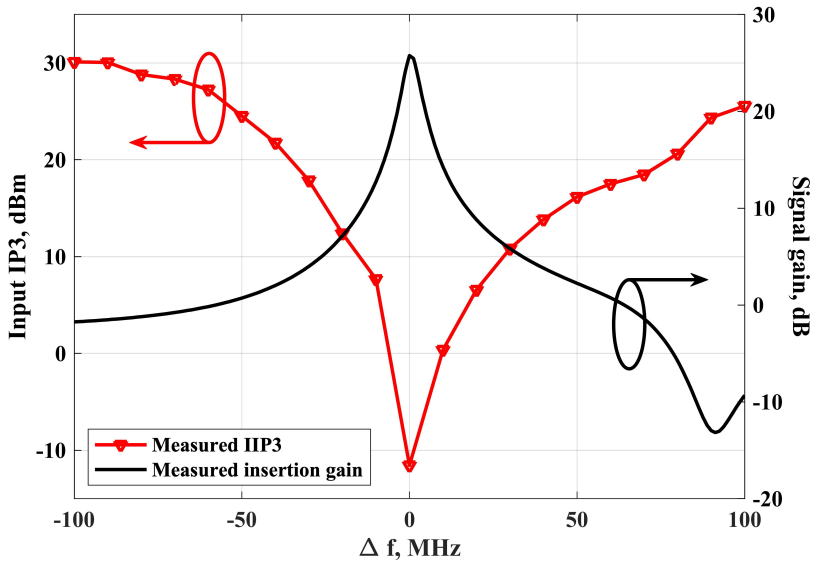

Figure 4-26 Measured input IP3 and its associated insertion gain with respect to the frequency offset from the peak gain frequency.

The performance of the tunable peak amplifier prototype was also compared with the state-of-the-art tunable peak amplifier and filter designs. The results are summarized in Table 4-1, the proposed tunable peak amplifier achieved the best frequency selectivity and noise figure. The out-of-band IIP3 was comparable to active N-path filters in literature. The power consumption for this design was high because the TVTL design has not been optimized for a high power-efficiency yet, and the MMIC processes used were low-cost GaAs HBT process that is not ideal for low-power applications. Ideally, parametric circuits enabled by nonlinear reactance can achieve 100% efficiency [47] if all harmonics and intermodulation tones are treated properly. This implies that there is great potential in improving the power efficiency and reducing the power consumption of a TVTL. Furthermore, it must be noted that the proposed tunable peak amplifier approach, unlike the N-path filter approach, does not have the noise folding issue and additional passbands at

harmonic frequencies. More importantly, the design could easily be scaled to a higher frequency and may ultimately lead to promising applications such as dynamic filtering and sensing.

Table 4-1 Comparison table – tunable peak amplifier/filter

	[63]	[64]	[65]	[66]	This work
Technology	CMOS 65nm	CMOS 65nm	CMOS 65nm	CMOS 65nm	GaAs HBT
Method	All-passive N-path filter	Active N-path filter	Active N-path filter	LNA with interference-rejecting loop	Parametric mixer with a positive feedback
Channel BW (MHz)	9~15	20	8	20	5
Frequency tunning range (GHz)	0.60 to 0.85	0.4-1.2	0.1-1.2	0.2-1.6	1.05 to 1.17
NF (dB)	8.6	10.0	2.6 to 3.1	3.6	1.8
Gain (dB)	-4.7 to -6.2	-2 to 3.2	25	14 to 24	>22
IB IP1dB (dBm)	0.0	NR	-23.0	NR	-18.5
IB IIP3 (dBm)	7.0	9.0	-12.0	NR	-11.5
OOB IIP3 (dBm@Δf)	17.5	29.0 (@50MHz)	26.0 (@50MHz)	14.5 (with linearity enhancement)	25.0 (@50MHz). 30.0 (@100MHz)
OOB rejection (dB)	30-50	55	59	NR	27
Power consumption (mW)	75.0	21.4	18.0 to 57.4	15.8 to 20.2	1260.0

NR – Not reported

Chapter 5

Conclusion

In this research, in-depth theoretical discussions of the time-varying transmission lines (TVTL) were first presented. The theoretical work discussed in Chapter 2 complemented well with some classical works in traveling-wave parametric amplifiers done in the 1950s and 1960s [8]-[11] as well as a recent work [37] by presenting a complete derivation of the conversion gain and noise figure of the TVTL operating in the single-sideband condition. The discussion on the noise performance of the TVTL in this work demonstrated a different understanding of the lower limit of the TVTL's noise figure than that in classical literature [9][44] in which a 3 dB noise figure lower limit was often quoted. The new understanding showed that the theoretical noise figure limit of the TVTL could be as low as the quantum noise limit. Moreover, with reactive input termination at ω_{p-s}, an additional benefit offered by the TVTL to the system noise performance was that the noise generated by the output load incident into the TVTL could be reflected with a properly designed phase and cancel what was originally generated by the load. It thus could bring the noise advantage even to the stage following the TVTL.

Moreover, three TVTL configurations, namely the traveling-wave TVTL, the reflective TVTL, and the directly-pumped TVTL were proposed and designed with commercial monolithic microwave integrated circuit (MMIC) processes. For the traveling-wave TVTL, the inductor-pumped structure was implemented to improve boost the conversion gain. Measured results showed that the MMIC traveling-wave TVTL could achieve a maximum of 2.1 dB conversion gain and a 2.7 dB mean noise figure within the measured frequency band. For the reflective TVTL, since multiple reflections and resonance were involved, thorough analyses on the conversion gain

and noise figure were included along with discussions on the trade-offs between gain, bandwidth, and noise figure when feedback was introduced. Measured results indicated that the MMIC reflective TVTL demonstrated a 0.4 dB conversion gain while requiring 7.6 dB less pump power than the traveling-wave TVTL. The noise figure of the reflective TVTL, however, was compromised due to the multiple reflections created in the reflective TVTL. For the directly-pumped MMIC TVTL, novel 3D solenoid inductors were employed to improve the quality factor of the MMIC inductors and reduce the insertion loss of the TVTL. Measured results demonstrated that $>$ 1.4 dB insertion gain and >1.7 dB conversion gain were observed for the entire measured signal frequency band from 600 MHz to 1.1 GHz, and a peak conversion gain of 4.2 dB was achieved at 600 MHz. The averaged insertion noise figure and conversion noise figure were 3.0 dB for the entire measurement frequency.

Lastly, the RF correlator with both the frequency translational approach and the tunable peak amplifier approach were demonstrated in Chapter 4. The RF correlator utilizes the TVTL as a low-loss and low-noise parametric mixer to perform multiplication in the correlation operation. When the signal code and the reference code are correlated, the desired signal can be received while the unwanted interference is spread out. Experimental results showed that 0 dB conversion loss was realized with the MMIC directly-pumped TVTL frequency translational correlator prototype, and the averaged noise figure was 3.8 dB. A 30 dB correlation suppression could be achieved by the designed RF correlator with the frequency translational approach comparing the orthogonal case with the correlated case. For the tunable peak amplifier, measurement results indicated that both the center frequency and the gain level of the tunable peak amplifier could be controlled via the pump. Even though the feedback and resonance were involved, the in-band noise figure of the tunable peak amplifier was <1.8 dB in both the simulations and measurements. Moreover, the

prototype also demonstrated good linearity, which was -11.5 dBm in-band IIP3 and 30 dBm out-of-band IIP3. This indicates that the tunable peak amplifier is capable of amplifying the desired signal while handling large out-of-band interference.

References

[1] Y. E. Wang, "Non-reciprocity with time-varying transmission lines (TVTLs)," in *IEEE Int. Wireless Inform. Technol. Syst. Conf*, Maui, Hi, USA, Nov. 2012.

[2] Y. E. Wang, "Time-varying transmission lines (TVTL) - A new pathway to non-reciprocal and intelligent RF front-ends," in *IEEE Radio Wireless Symp.*, Newport Beach, CA, Jan. 2014.

[3] M. Samizadeh Nikoo, S. M. Hashemi and F. Farzaneh, "Theory of Terminated Nonlinear Transmission Lines," *IEEE Trans. Microw. Theory Techn.*, vol. 66, no. 1, pp. 91-99, Jan. 2018.

[4] N. Seddon, C. R. Spikings, and J. E. Dolan. "RF pulse formation in nonlinear transmission lines." in *IEEE Int. Pulsed Power Conf*, Albuquerque, NM, vol. 1, pp. 678-681, 2007.

[5] I.V., Romanchenko, V. V. Rostov, V. P. Gubanov, A. S., Stepchenko, A. V. Gunin, and I. K., Kurkan, "Repetitive sub-gigawatt RF source based on gyromagnetic nonlinear transmission line." *Rev. Sci. Inst*., vol. 83, no. 7, p.074705, 2012.

[6] Y. Wang, L. J. Lang, C. H. Lee, B. Zhang, and Y. D. Chong. "Topologically enhanced harmonic generation in a nonlinear transmission line metamaterial," *Nature Commun.*, vol. 10, no. 1, pp. 1-7, Mar. 2019.

[7] R. Landauer, "Parametric amplification along nonlinear transmission line," *J. Appl. Phys.*, vol. 31, no. 3, pp. 479–484, Mar. 1960.

[8] P. K. Tien and H. Suhl, "A Traveling-Wave Ferromagnetic Amplifier," *Proc. IRE*, vol. 46, no. 4, pp. 700-706, April 1958.

[9] Tien, P. K. "Parametric amplification and frequency mixing in propagating circuits," *J. Appl. Phys.*, vol. 29, no. 9, pp. 1347-1357, Sep. 1958.

[10] A. Cullen, "A Travelling-Wave Parametric Amplifier", *Nature*, vol. 181, no. 4605, pp. 332-332, 1958.

[11] R. Mavaddat and F. J. Hyde, "Investigation of an experimental travelling-wave parametric amplifier," *Proc. of the IEE-Part B: Electron. Commun. Eng.*, vol. 109, no. 47, pp. 405-413, Sep. 1962.

[12] H. Heffner and G. Wade, "Gain, Band Width, and Noise Characteristics of the Variable-Parameter Amplifier," *J. Appl. Phys.*, vol. 29, no. 9, pp. 1321-1331, 1958.

[13] J. Edrich, "Low-noise parametric amplifiers tunable over one full octave," *IEEE J. Solid-State Circuits*, vol. 7, no. 1, pp. 32-37, Feb. 1972.

[14] A. Smith, R. Sandell, J. Burch, and A. Silver, "Low noise microwave parametric amplifier," *IEEE Trans. Magn.*, vol. 21, no. 2, pp. 1022-1028, March 1985.

[15] R. Stolen, "Phase-matched-stimulated four-photon mixing in silica-fiber waveguides," *IEEE J. Quantum Electron.*, vol. 11, no. 3, pp. 100-103, March 1975.

[16] R. Stolen and J. Bjorkholm, "Parametric amplification and frequency conversion in optical fibers," *IEEE J. Quantum Electron.*, vol. 18, no. 7, pp. 1062-1072, July 1982.

[17] M. Foster, A. Turner, J. Sharping, B. Schmidt, M. Lipson, and A. Gaeta, "Broad-band optical parametric gain on a silicon photonic chip", *Nature*, vol. 441, no. 7096, pp. 960-963, 2006.

[18] M. Marhic, P. Andrekson, P. Petropoulos, S. Radic, C. Peucheret, and M. Jazayerifar, "Fiber optical parametric amplifiers in optical communication systems", *Laser Photonics Rev.*, vol. 9, no. 1, pp. 50-74, 2014.

[19] B. Kuo, M. Hirano, and S. Radic, "Continuous-wave, short-wavelength infrared mixer using dispersion-stabilized highly-nonlinear fiber", *Opt. Express*, vol. 20, no. 16, pp. 18422-18431, 2012. Available: 10.1364/oe.20.018422.

[20] S. Radic, "Parametric Signal Processing," *IEEE J. Sel. Topics Quantum Electron.*, vol. 18, no. 2, pp. 670-680, March-April 2012.

[21] J. Sharping, M. Fiorentino, P. Kumar, and R. Windeler, "Optical parametric oscillator based on four-wave mixing in microstructure fiber", *Opt. Lett.*, vol. 27, no. 19, p. 1675, 2002.

[22] B. Yurke, L. Corruccini, P. Kaminsky, L. Rupp, A. Smith, A. Silver, R. Simon, E. Whittaker, "Observation of parametric amplification and deamplification in a Josephson parametric amplifier", *Phys. Rev. A*, vol. 39, no. 5, pp. 2519-2533, 1989.

[23] M. Castellanos-Beltran and K. Lehnert, "Widely tunable parametric amplifier based on a superconducting quantum interference device array resonator", *Appl. Phys. Lett.*, vol. 91, no. 8, p. 083509, 2007.

[24] C. Macklin, K. O'Brien, D. Hover, M. Schwartz, V. Bolkhovsky, X. Zhang, W. Oliver, I. Siddiqi, "A near-quantum-limited Josephson traveling-wave parametric amplifier", *Science*, vol. 350, no. 6258, pp. 307-310, 2015.

[25] S. Magierowski, J. Bousquet, Z. Zhao, and T. Zourntos, "RF CMOS Parametric Downconverters," *IEEE Trans. Microw. Theory Techn.*, vol. 58, no. 3, pp. 518-528, March 2010.

[26] Z. Zhao, S. Magierowski and L. Belostotski, "Parametric CMOS upconverters and downconverters", *Int. J. Circuits. Theor. App.*, vol. 42, no. 12, pp. 1209-1227, 2013.

[27] M. Hedayati, L. K. Yeung, M. Panahi, X. Zou, and Y. E. Wang, "Parametric Downconverter for Mixer-First Receiver Front Ends," *IEEE Trans. Microw. Theory Techn.*, pp. 1–1, 2021.

[28] W. Lee and E. Afshari, "Low-Noise Parametric Resonant Amplifier," *IEEE Trans. Circuits Syst. I: Reg. Papers*, vol. 58, no. 3, pp. 479-492, March 2011.

[29] B. Gray, "Design of RF and Microwave Parametric Amplifiers and Power Upconverters", *Ph.D. dissertation*, School of Elect. and Comp. Eng., Georgia Inst. of Tech., USA, 2012 [Online]. Available: https://smartech.gatech.edu/handle/1853/43613

[30] L. K. Yeung, X. Zou, and Y. E. Wang, "Parametric quality factor enhancement for highly-selective miniaturized BPFs," in *IEEE Radio Wireless Symp.*, San Antonio, TX, Jan. 2020, pp. 148–151.

[31] L. K. Yeung, X. Zou, and Y. E. Wang, "BPFs with parametrically compensated passband insertion loss and selectivity," in *IEEE MTT-S Int. Microw. Symp.*, Los Angeles, CA, pp. 803–806, Aug. 2020.

[32] L. K. Yeung, X. Zou, and Y. Wang, "Parametrically enhanced bandpass filters," *IET Microw., Antennas & Propag.*, vol. 15, no. 2, pp. 229–240, 2021.

[33] J. D. Schneider, T. Lu, S. Tiwari, X. Zou, A. Mal, R. N. Candler, Y. E. Wang, and G. P. Carmen., "Frequency conversion through nonlinear mixing in acoustic waves," *J. Appl. Phys.*, vol. 128, no. 6, p. 064105, 2020.

[34] T. Lu, J. D. Schneider, X. Zou, S. Tiwari, Z. Yao, G. P. Carmen, R. N. Candler, Y. E. Wang, "Lamb Wave Resonator Loaded Non-reciprocal RF Devices," in *IEEE MTT-S Int. Microw. Symp.*, Los Angeles, CA, pp. 516–519, Aug. 2020.

[35] X. Zou and Y. E. Wang, "Parametric Flat Lenses for Near-Field Imaging and Electronic Beam Scanning," in *IEEE Int. Antennas Propag. Symp. & North American Radio Sci. Mtg.*, Jul. 2020, pp. 511–512.

[36] S. Qin, and Y. E. Wang, "Parametric conversion with distributedly modulated capacitors (DMC) for low-noise and non-reciprocal RF front-ends," in *IEEE MTT-S Int. Microw. Symp.*, Seattle, WA, pp. 1-3, Jun. 2013.

[37] S. Qin, Q. Xu, and Y. E. Wang, "Nonreciprocal Components with Distributedly Modulated Capacitors," *IEEE Trans. Microw. Theory Techn.*, vol. 62, no. 10, pp. 2260-2272, Oct. 2014.

[38] S. Qin and Y. E. Wang, "Broadband Parametric Circulator with Balanced Monolithic Integrated Distributedly Modulated Capacitors (DMC)," in *IEEE Int. Microw. Symp.*, San Fracisco, CA, pp. 1-4, 2016.

[39] Q. Wu, X. Zou, S. Qin, and Y. E. Wang, "Frequency translational RF receiver with time-varying transmission lines (TVTL)," in *IEEE MTT-S Int. Microw. Symp.*, Honolulu, HI, pp. 1767-1769, 2017.

[40] X. Zou, Q. Wu, and Y. E. Wang, "Parametrically Enhanced Delay Line with Monolithically Integrated Time-varying Transmission Lines (TVTL)," in *IEEE Radio Wireless Symp.*, Orlando, FL, pp. 1–3, Jan. 2019.

[41] C. Andrews and A. C. Molnar, "Implications of Passive Mixer Transparency for Impedance Matching and Noise Figure in Passive Mixer-First Receivers," *IEEE Trans. Circuits Syst. I: Reg. Papers*, vol. 57, no. 12, pp. 3092-3103, Dec. 2010.

[42] A. Molnar and C. Andrews, "Impedance, Filtering and Noise in N-phase Passive CMOS Mixers," in *Proc. IEEE Cust. Integr. Circuits.*, San Jose, CA, 2012, pp. 1-8.

[43] E. A. M. Klumperink, H. J. Westerveld, and B. Nauta, "N-path filters and mixer-first receivers: A review," in *IEEE Cust. Integr. Circuits*, Austin, TX, 2017, pp. 1-8.

[44] W.H. Louisell, "Parametric coupling principle for lumped circuits," in *Coupled Mode and Parametric Electronics*. Hoboken, NJ, USA: John Wiley & Sons, Inc., 1960, ch. 4, sec. 6, pp. 115-118.

[45] X. Zou, Q. Wu, and Y. E. Wang, "Monolithically Integrated Parametric Mixers With Time-Varying Transmission Lines (TVTLs)," *IEEE Trans. Microw. Theory Techn.*, vol. 68, no. 10, pp. 4479–4490, Oct. 2020.

[46] B. H. Eom, P. K. Day, H. G. LeDuc and J. Zmuidzinas, "A wideband, low-noise superconducting amplifier with high dynamic range," *Nature Physics*, vol. 8, pp. 623–627 (2012).

[47] J. M. Manley and H. E. Rowe, "Some General Properties of Nonlinear Elements-Part I. General Energy Relations," *Proc. IRE*, vol. 44, no. 7, pp. 904-913, July 1956.

[48] D. M. Pozar, "Noise and Nonlinear Distortion," in *Microwave Engineering*. ed. 4, Hoboken, NJ, USA: John Wiley & Sons, Inc., 2012, ch. 10, sec. 1-2.

[49] Q. Wu, X. Zou, and Y. E. Wang, "RF Correlator Receiver Based on Monolithically Integrated Directly-Pumped Time-Varying Transmission Lines," *preparation for publication*.

[50] Q. Wu, X. Zou, R. Zhu, and Y. E. Wang, “Chip-Scale RF Correlator with Monolithically Integrated Time-Varying Transmission Line (TVTL),” in *IEEE Int. Microw. Symp.*, Philadelphia, PA, pp. 431–434, Jun. 2018.

[51] Q. Wu, " Monolithically Integrated Time-varying Transmission Line (TVTL) for Signal Processing", *Ph.D. dissertation*, Dept. Elect. Comp. Eng., UCLA, USA, 2012 [Online]. Available: https://escholarship.org/content/qt1fw7r5dp/qt1fw7r5dp.pdf

[52] M. Gilden and G. L. Matthaei, "Practical Design and Performance of Nearly Optimum Wide-Band Degenerate Parametric Amplifiers” *IRE Trans. Microw. Theory Techn*., vol. 9, no. 6, pp. 484-490, November 1961.

[53] W. J. Getsinger and G. L. Matthaei, "Some Aspects of the Design of Wide-Band Up-Converters and Nondegenerate Parametric Amplifiers," *IEEE Trans. Microw. Theory Techn*., vol. 12, no. 1, pp. 77-87, January 1964.

[54] G. R. Branner and Shu-Park Chan, "A New Technique for Synthesis of Broad-Band Parametric Amplifiers," *IEEE Trans. Microw. Theory Techn.*, vol. 21, no. 7, pp. 437-444, Jul. 1973.

[55] S. Egami, "In-Line Signal Circuit for Broad-Band Parametric Amplifiers," *IEEE Trans. Microw. Theory Techn.*, vol. 23, no. 3, pp. 282-287, Mar. 1975.

[56] J. Kim, R. Shenoy, K. Lai, and J. Kim, "High-Q 3D RF solenoid inductors in glass," *IEEE Radio Freq. Integr. Circuits. Symp.*, Tampa, FL, pp. 199-200, 2014,

[57] N. Kim, V. Aparin, and L. E. Larson, “A Resistively Degenerated Wideband Passive Mixer With Low Noise Figure and High IIP_2,” *IEEE Trans. Microw. Theory Techn.*, vol. 58, no. 4, pp. 820–830, 2010.

[58] D. Na and T. W. Kim, "A 1.2 V, 0.87–3.7 GHz Wideband Low-Noise Mixer Using a Current Mirror for Multiband Application," *IEEE Microw. Wireless Compon. Lett.*, vol. 22, no. 2, pp. 91-93, Feb. 2012.

[59] S. S. K. Ho and C. E. Saavedra, "A CMOS Broadband Low-Noise Mixer With Noise Cancellation," *IEEE Trans. Microw. Theory Techn.*, vol. 58, no. 5, pp. 1126-1132, May 2010.

[60] X. Zou, Q. Wu, and Y. E. Wang, “Tunable peak amplifier with monolithically integrated time-varying transmission lines (TVTL),” *preparation for publication.*

[61] S. Qin and Y. E. Wang, "A nonreciprocal, frequency-tunable notch amplifier based on Distributedly Modulated Capacitors (DMC)," in *IEEE Int. Microw. Symp.*, San Francisco, 2016, pp. 1-3, doi: 10.1109/MWSYM.2016.7540316.

[62] B. Razavi, “Basic Concepts in RF Design,” in *RF microelectronics*. vol. 2. New York: Prentice Hall, 2012, ch. 2, sec.5.

[63] N. Reiskarimian and H. Krishnaswamy, "Design of all-passive higher-order CMOS N-path filters," in *IEEE Radio Freq. Integr. Circuits Symp.* Phoenix, AZ, pp. 83-86, May 2015.

[64] M. Darvishi, R. van der Zee, E. A. M. Klumperink and B. Nauta, "Widely Tunable 4th Order Switched G_m-C Band-Pass Filter Based on N-Path Filters," *IEEE J. Solid-State Circuits*, vol. 47, no. 12, pp. 3105-3119, Dec. 2012.

[65] M. Darvishi, R. van der Zee and B. Nauta, "Design of Active N-Path Filters," in *IEEE J. Solid-State Circuits*, vol. 48, no. 12, pp. 2962-2976, Dec. 2013.

[66] J. Zhu, H. Krishnaswamy, and P. R. Kinget, "Field-Programmable LNAs With Interferer-Reflecting Loop for Input Linearity Enhancement," *IEEE J. Solid-State Circuits*, vol. 50, no. 2, pp. 556-572, Feb. 2015.